# FRICTION STIR WELDING OF POLYMERS AND POLYMER COMPOSITES

By

Lucas Thomas Wilkins

Dissertation
Submitted to the Faculty of the
Graduate School of Vanderbilt University
in partial fulfillment of the requirements
for the degree of

DOCTOR OF PHILOSOPHY
in

Mechanical Engineering

December 16, 2023

Nashville, Tennessee

Committee:

Alvin M. Strauss, Ph.D.
Kevin C. Galloway, Ph.D.
James R. McBride, Ph.D.
D. Greg Walker, Ph.D.
Thomas J. Withrow, Ph.D.

# ACKNOWLEDGMENTS

Completion of the work in this dissertation was made possible by a countless number of individuals. I would first like to thank Dr. Alvin Strauss for providing me the opportunity to work in the Vanderbilt University Welding Automation Lab. You gave me the freedom to explore problems that interest me, and I have learned and gained more skills while at Vanderbilt than I could have possibly imagined. I would also like to thank my committee members Dr. Kevin Galloway, Dr. James McBride, Dr. Greg Walker, and Dr. Thomas Withrow. All of you gave me valuable guidance and provided me with resources that helped my research practices grow and mature. Additionally, I would like to thank the Tennessee Space Grant Consortium for funding me and my projects.

My lab mates and colleagues at Vanderbilt taught me skills, helped me consider alternative ideas, and provided a helping hand when I needed it. I would like to thank former and current graduate students Todd Evans, Adam Jarrel, Kelsay Neely, Connor Strawn, Benjamin Snyder, Brayden Terry, Victoria Vest, Henry Gunner, Austen Shelton, Benjamin Firestone, and Hayden Jenkins for a positive workplace and reliable source of entertainment. I also gained valuable experience working with Eric Zhang, who as an undergraduate researcher helped me complete two novel projects and exhibited substantial growth working with me over four semesters. Furthermore, a huge thanks to Phil Davis, Mark Thelen, Dr. Lesa Brown, Dr. Rossanne Delapp, Dr. Janet Macdonald, and Garret Thorne for teaching me new skills and providing critical support for my projects.

I am mostly appreciative of my family who shaped me into the person I am today. I am lucky to have two wonderful older sisters, Olivia and Rachel, with unique skills and characteristics who served as role models in all aspects of my life. My parents, Tom and Terry, taught me to push myself, encourage me to learn a wide range of new skills, and preached to not be afraid to fail. They fostered my love of mechanical machines from a young age, supported me with all of my next “great” ideas, and continue to do so today. Finally, I would like to thank my girlfriend Amy who helps me balance work and life, supports my endeavors, and has helped me grow considerably over the last few years.

# TABLE OF CONTENTS

Page

# LIST OF TABLES

# LIST OF FIGURES

# LIST OF ABBREVIATIONS

## Abbreviations

| | |
|---|---|
| ABS | Acrylonitrile butadine styrene |
| AS | Advancing side |
| CF | Carbon fiber |
| CFRTP | Carbon fiber reinforced thermoplastic |
| DOE | Design of experiments |
| DSC | Differential scanning calorimetry |
| FCC | Face-centered central composite |
| FSP | Friction stir processing |
| FSW | Friction stir welding |
| HDPE | High density polyethylene |
| IPM | Inches per minute |
| LMPAEK | Low-melt polyaryletherketone |
| PC | Polycarbonate |
| PEEK | Polyetheretherketone |
| PVC | Polyvinyl chloride |
| RS | Retreating side |
| RSM | Response surface methodology |
| SEM | Scanning electron microscopy |
| TGA | Thermogravimetric analysis |
| TMAZ | Thermo-mechanically affected zone |
| TPI | Threads per inch |
| TS | Tensile strength |
| UTS | Ultimate tensile strength |

## Symbols

| | |
|---|---|
| $\omega$ | Rotational velocity |
| $\omega_c$ | Weight fraction carbon fiber |
| $\sigma$ | Standard deviation |
| $\tau$ | Torque |
| $d$ | Thread depth |
| $k$ | Thermal conductivity |
| $P$ | Power |

| | |
|---|---|
| $q$ | Heat generation |
| $R^2$ | Coefficient of determination |
| $R_s$ | Electrical resistance |
| $T_g$ | Glass transition temperature |
| $T_m$ | Melting temperature |
| $T_{95}$ | Temperature at 5% weight loss |
| $x_c$ | Crystallization fraction |

# CHAPTER 1

## Introduction

A world where mankind pushes the boundaries of engineering complex structures and machines requires quality joining methods to attach various parts and components. Friction stir welding (FSW) is currently used to join alloy components in industries including aerospace, automotive, rail, maritime, and tech. Its continued use for many applications in these industries proves its value for joining metallic materials. However, continuous growth of the use of polymeric materials in these and other industries requires advancements in their joining techniques as well. Researchers applied FSW methods to polymeric materials over the last couple of decades, though industry has yet to adopt it as a viable polymer joining process. Fierce competition with other already established polymer joining methods hinder FSW's adoption in the realm of thermoplastics. With a greater focus on joining metals, polymer industries are starved of relevant FSW research that focuses on polymer joining. This dissertation focuses on advancing FSW as a polymer joint manufacturing process. Key areas to fulfill this mission include enhancing the understanding of polymer science with FSW and expanding potential applications where FSW may be beneficial over other current polymer joining technologies.

This dissertation's outlined structure begins with a literature review in Chapter 2, which discusses the relevant characteristics of polymers and welding that must be considered to friction stir weld thermoplastics and composites. Chapter 3 provides a tool study to better understand the influence of tool geometry during FSW of neat polymers. Chapter 4 demonstrates the joining of PVC pipe couplings as a new application for FSW. Chapter 5 shifts the focus to polymer composites with a derivative process of FSW, friction stir processing (FSP), to establish a more efficient method of forming metal-polymer composites. Chapter 6 presents novelty in the field of FSW with joints of woven carbon fiber reinforced thermoplastic (CFRTP) laminates. Chapter 7 expands on the research in Chapter 6 by implementing post-weld heat treating to further improve mechanical joint properties. The dissertation concludes with Chapter 8.

### Overview of Work

Chapter 3 explores the influence of tool thread pitch during FSW of neat high density polyethylene. The tool geometry is among many parameters that affect joint quality during FSW. A general consensus among many published works suggests that threaded tools offer superior improved joint strength over non-threaded tools. However, there is a lack of understanding of the influence of the thread pitch during polymer FSW. This study considers tools fabricated with variable thread pitches under several experimental conditions.

Using response surface methodology (RSM), statistical approaches were used to evaluate the influence of thread pitch compared to other experimental variables. These results contribute to the understanding of tool/workpiece interaction so that FSW can be better optimized for a variety of joint configurations with a variety of other polymeric materials.

Chapter 4 demonstrates FSW in a novel polymer joint configuration by welding off-the-shelf PVC pipe and pipe couplings. Further analysis evaluates its feasibility in a portable application since water supply and drainage pipelines require on-site assembly. The metrics to determine portable welding feasibility include an analysis of machine requirements as well as post-weld chemical properties of the PVC that indicate low risk of health hazards for machine operators. Weld performance under hydraulic pressure and overall joining times were compared to current commercially used joining methods for small diameter PVC pipe. This research fulfills goals to identify new applications and industries that can benefit from FSW technologies.

Chapter 5 focuses on friction stir processing (FSP), a derivative process used to form polymer composites. In this study, a new variant of FSP called *top plate FSP* improves the efficiency of metal-polymer composite formation over large areas compared to previously studied FSP techniques. Top plate FSP uses successive welding passes of a thin metal plate over a polymer to form a composite. The top plate serves multiple functions including temperature control and material confinement that allows for use of conventional FSW tools. Though other researchers demonstrate FSP induced modifications to the base material's mechanical properties and conductivity, this study addresses the ability to do so over large areas rather than a long narrow region.

Chapter 6 introduces FSW to applications of joining woven CFRTP used in aerospace applications. Further novelty in this work includes welding of low-melt polyaryletherketone (LMPAEK), which is gaining popularity in aerospace sectors due to its improved processibility compared to mature thermoplastics of similar properties. This work has relevance as the next generation of aerospace vehicles will utilize more CFRTP in primary and secondary structures than ever before due to their weld-ability among other characteristics.

Chapter 7 uses results from Chapter 6 as a foundation for continued research, where strength optimized welds undergo post-weld heat treating to further improve their properties. Rapid processing times during welding of thermoplastics can limit mechanical performance. By implementing post-weld annealing, the mechanical properties of large batches of welded parts can be improved simultaneously. Post-weld processing of large batches can improve overall manufacturing efficiency by eliminating the need to increase individual part processing times during welding. The principles of post-weld processing not only apply to friction stir welded joints, but composite joints formed by other thermoplastic welding methods as well. Thus, this work contributes to many thermoplastic manufacturing and joining methods across many sectors.

# CHAPTER 2

# Literature Review

## 2.1 Polymeric Materials

Polymeric materials exist in all aspects of modern day life. From thread in clothing to aircraft fuselages, polymers come in many forms and serve a wide range of purposes. Often used interchangeably, the term plastic refers to specific polymeric compounds that have irreversible strain under large stresses [6]. Rubbers on the other hand, are polymers that can return their shape following large strains.

Polymers have a growing presence in vehicle structures for their high versatility and lightweight properties. Estimates of 10% weight reduction in automobiles results in a 5%-7% reduction in fuel consumption [19]. Polymers can also be formed into complex shapes. For these reasons current automobiles consist of over 150 kg of plastics in their construction [19]. Reinforced polymers have a growing presence, especially in aerospace. In 1972, the Airbus A300 began use of polymer composites structures in fin leading edges and fairing panels. Today, commercial aircraft such as the Boeing 787 utilize polymer composites in primary and secondary structures such as the main fuselage construction and access panels. The 787 has approximately 50% composite structures by weight [2], shown in figure 2.1.

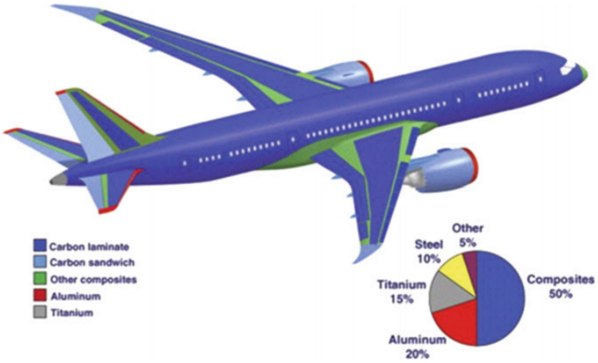

Figure 2.1: Use of carbon fiber-reinforced composites in the Boeing 787. Adopted from [2].

Polymers' superior corrosion resistance compared to many metallic materials also prompts their further adoption and integration. Water pipeline systems face rapid deterioration from corroding iron pipes. Corrosion induced leaks cause billions of dollars of losses every year [20]. Polymeric pipes have significantly longer usable life than metallic pipes and require less maintenance due to inertness to acidic environments [21]. Their ductility aids in robustness under changing landscapes, but also serves to simplify installation since they can be pulled through curved tunnels and trenches [22]. These qualities among others results in continued growth in implementation of polymeric pipe systems. Figure 2.2 exemplifies polymeric pipe popularity with growing use in potable water applications.

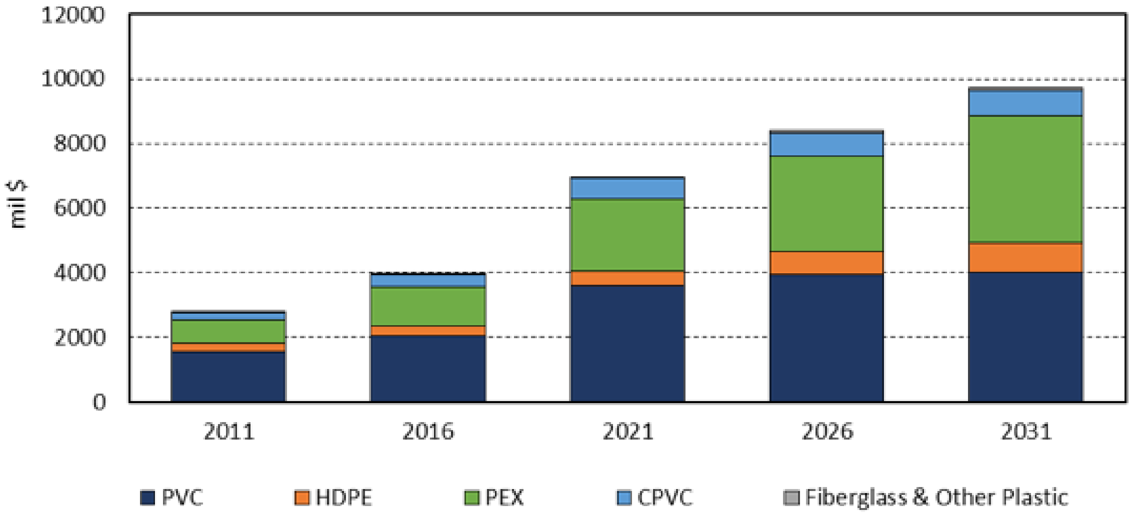

Figure 2.2: Potable water plastic pipe market. Adopted from [3].

Further adoption of polymers into engineering structures will continue due to many of their desirable properties. These properties and variety across many different polymer types is a product of their fundamental structure.

### 2.1.1 Polymer Structure

The word polymer derives from Greek roots, where the prefix *poly-* means "many" and *meros* means "parts" [23]. Polymers are large molecules formed by smaller covalently bonded monomer units in a pattern. Grouped atoms of two or more bonding sites compose these monomer units [6]. Three subcategories encompass polymers: elastomers, thermosets, and thermoplastics. The molecular arrangement and interaction in each subcategory dictates its behaviors at various temperatures. Thermosetting polymers solidify using a chemical reaction to cure them [23]. For example, super glue reacts with water molecules in the air to cure and permanently harden. Cross-linking between polymer chains limits their mobility in thermosets, resulting in permanent form when they cure. Elastomers consist of partially cross-linked units that have a permanent structure but offer increased flexibility, such as rubber tires [1].

Thermoplastics do not have cross-linked polymer chains, which allows them to slide passed each other given the right temperature conditions. Below the glass transition temperature ($T_g$), the polymer chains are rigid and act like stiff springs. Temperatures above $T_g$ permit the polymer chains to relax and mobilize. This transition is completely reversible, allowing thermoplastics to be thermoformed. Thus with thermoplastics,

---

[1] The process of cross-linking rubber is called Vulcanization, invented by Charles Goodyear in 1839.

pellets can be melted and injection molded, sheets can be compression molded, parts can be welded, and parts can be recycled at their end of life. The ability to reprocess thermoplastics post-solidification makes them attractive for manufacturing processes. Thus, all polymer related work in this dissertation implements the use of thermoplastics.

Two subcategories classify thermoplastic structures: amorphous and semi-crystalline. Figure 2.3 shows a comparison between their structures, where amorphous polymers have a random structure and semi-crystalline polymers have regions of higher order between molecular chains.

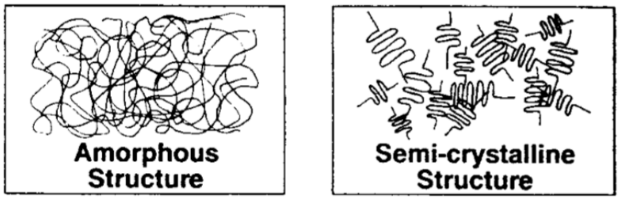

Figure 2.3: Structural arrangement of amorphous and semi-crystalline polymers. Adopted from [4].

The morphology plays a role in thermoplastic processing, as it dictates polymer behavior with respect to temperature. For example, amorphous polymers have five relative states with respect to temperature. These states consist of the glassy state ($T < T_g$), followed by the leathery state, rubbery state, rubbery flow, and viscous state [6]. Amorphous polymers do not have a sharp melting point. Rather, their molecular mobility progressively increases with temperature to a highly viscous liquid.

Semi-crystalline polymers have regions of tightly folded molecular chains. Polymolecularity of the macromolecules prohibits a 100% crystalline structure, so amorphous regions reside in between and connect crystals [23]. Like amorphous polymers, semi-crystalline polymers have a glassy state, and therefore a glass transition temperature $T_g$. Semi-crystalline polymers also have two more distinct transition temperatures including the crystallization temperature $T_c$ and the melting temperature $T_m$. Crystal structures are only maintained below $T_c$. When melted, molecular chains fully relax and can flow as a viscous liquid just like an amorphous polymer. Upon cooling, the polymer chains begin to stack and form crystal regions at $T_c$. The total percentage of crystalline structure relies on the rate of cooling, as crystallization rates are also temperature dependent [24]. The degree of crystallinity upon cooling can be described by the following equation [23]:

$$x(t) = x_\infty(1 - e^{-Zt^n}) \tag{2.1}$$

$x_\infty$ is the maximum percent crystallinty, typically determined by experiment for specific polymers. $Z$ is a molecular weight and temperature dependent crystallization rate, $t$ is time, and $n$ is the Avrami exponent. $n$ ranges between 1 to 4 depending on the specific nucleation structure. 1 corresponds to instantaneous rod-like growth, 2 is continuous rod-like growth, 3 is disclike growth, and 4 is spherulitic growth. Measureable crystallization growth occurs between $T_m - 10K$ to $T_g + 30K$ since chain entanglements at lower temperatures hinder chain diffusion and thermal motions at higher temperatures disrupt crystal nucleation [6]. Thus with the aforementioned temperature range, quickly cooling a semi-crystalline polymer from the melt, or quenching, can result in an amorphous polymer. Likewise, heating an amorphous polymer capable of forming crystals and slowly cooling it can increase its % crystallinity through a process called annealing. The degree of crystallization affects the polymer's mechanical properties, chemical resistance, and permeability [23, 25, 26]. Thus, the cooling rates during processing of semi-crystalline thermoplastics must be considered to produce desirable properties.

Molecular arrangement dictates mechanical properties, thermal properties, rheological properties, and chemical resistance. Even slight modifications to a polymer's molecular structure can drastically change any of these properties. For example, consider the molecular arrangement of polyetheretherketone (PEEK), shown in figure 2.4a. Each monomer unit consists of two ether groups and one ketone group, each separated by an aryl group. PEEK possesses high performing mechanical properties and chemical resistance. Like most variations in the family of polyaryletherketones (PAEK), PEEK follows an "unwritten rule" with a ratio between the melting and glass transition temperature of 1.5. Upon insertion of one extra aryl group in 25% of the monomers, nearly all mechanical and thermal properties are retained with the exception of a lower melting temperature [5]. The modified polymer, called low-melt polyaryletherketone (LMPAEK), is easier to process but remains rigid at nearly the same temperatures as PEEK.

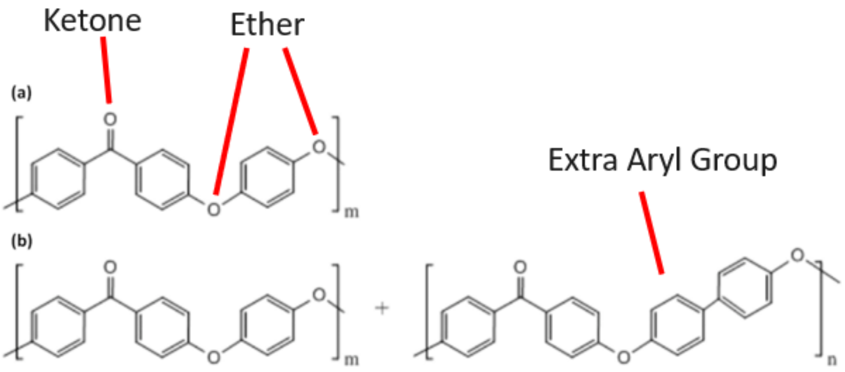

Figure 2.4: Molucular structure of a)PEEK and b)LMPAEK. Adopted from [5].

### 2.1.2 Composites

The term *composite* represents a material composed of two or more materials at a macroscopic scale [27]. The "macroscopic" component is key to distinguish a composite, as many materials are a mixture of smaller components. For example, aluminum alloy AA-6061 consists of Al, Mg, Si, Fe, Cu, Cr, Zn, Ti, and Mn. Though the alloy has mixtures on the microscopic scale, it is macroscopically homogenous and the individual components are indistinguishable. Composite materials serve the purpose of using the favorable properties from each constituent. Enhanced material properties when forming a composite can include but are not limited to improving strength, stiffness, fatigue life, resistance to corrosion, wear resistance, temperature-dependent behavior, electrical insulation/conductivity, and thermal insulation/conductivity.

Fiber reinforced plastics (FRP) take advantage of long reinforcing length scales to effectively distribute loads across a body. A material's strength tends to rely on its dimensions due to defects that concentrate stress and produce inherent weakness. For this reason, a cluster of small diameter fibers has improved strength over a single larger diameter fiber since a defect in one fiber will not spread to another fiber under load [28]. Fiber reinforcement types include short/chopped and continuous. Short fibers allow for injection molding and near isotropic mechanical properties if the suspended fibers have a random orientation. Short fibers allow for forming composite materials with highly complex geometry. They do not bear the strength of continuous fiber reinforcement though, as a greater number of fiber ends in the matrix leads to more stress concentrations and are more prone to void formation [28]. Continuous fiber reinforcement offers superior strength in composites along the fiber direction. However, anisotropic reinforcement requires stacking of layers with strategic fiber orientations to ensure directional strength and stiffness [27].

Common fiber reinforcement materials include aramid, glass, and carbon. Many materials have a similar modulus/weight ratio, and only aramid and carbon fibers have substantial substantial advantages over other materials [29]. Aramid fibers are made from aromatic polyamide and often go by the trade name Kevlar. The most common precursors for carbon fibers are polyacrylonitrile (PAN), pitch (petroleum), and rayon (cellulose) [2, 28] [2]. Precursor type and processing procedure dictates mechanical properties and matrix adhesion characteristics. For example, pitch fibers tend to have greater modulus than PAN fibers [2], shown in figure 2.5. However, pitch fibers also tend to have lower compressible strength [28].

The introduction of fibers into a polymer can have huge improvements to the polymer's mechanical properties. For example, virgin polycarbonate (PC) has a specific tensile strength of $52\frac{kNm}{kg}$ [23]. T300 carbon fiber has a tensile strength of approximately 3.5 GPa. When reinforced with 43% woven T300 by weight, the PC/T300 composite can have a specific tensile strength of 537 $\frac{kNm}{kg}$. High specific strengths of fiber reinforced composites makes them competitive material choices in many applications including primary and secondary structures in aircraft, spacecraft, automobiles, marine hulls, wind turbine blades, and sports equipment [2].

Polymer nanocomposites consist of small particle fillers suspended in a polymer matrix. Metal and metal

---

[2] Thomas Edison invented carbon fiber in 1879 for light bulb filaments. His carbon fiber precursors were cotton and bamboo [2]

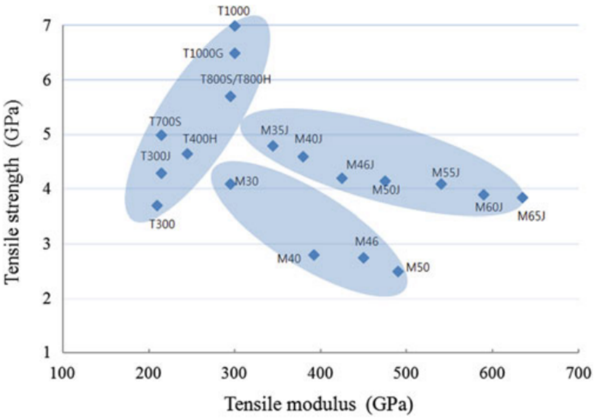

Figure 2.5: Classification of high-performance carbon fibers. “T” are PAN based. “M” are pitch based. Adopted from [2].

oxide fillers serve to improve thermal and electrical conductivity, chemical resistance, wear resistance, oxidation resistance, and mechanical properties [30, 31]. Clay based fillers can also offer enhanced mechanical properties over the neat polymer due to exfoliated layers that increase surface interaction with the polymer [32]. A huge advantage of these composites is their low cost due to inexpensive filler materials and ease of processing compared to fiber reinforced polymers [33].

## 2.2 Welding

### 2.2.1 Overview

A common assumption of the term “welding” is that it implies joining metals together by melting them at their interface. In fact, the Cambridge Dictionary defines the verb *weld* as “to join two pieces of metal together permanently by melting the parts that touch” [34]. This definition identifies specific material and joining criteria that do not always apply. The Welding Institute (TWI) provides a more general definition, stating “Welding is a fabrication process whereby two or more parts are fused together by means of heat, pressure, or both forming as the parts cool” [35]. The general approach now includes joining of non-metallic materials including thermoplastics.

Metallic welding methods include both liquid state and solid state processes. Liquid state, or fusion welding, requires a heat source to melt the joining materials so that they flow together. Metal fusion welding typically requires high energy often through an electrical arc to melt the metal. Fusion welding methods may utilize molten casting, gas, electrical resistance, electrical arc, electron beams, or lasers as a heat source to melt the joining metals. Solid state welding methods utilize heat and pressure to coalesce the joining materials together and form metallurgical bonds at temperatures below the melting point of the joining materials [36]. Solid state welding methods include diffusion and friction welding.

### 2.2.2 Polymer Welding

Polymeric welding requires the diffusion of polymer chains across the joining interface. Unlike metals, molecular chains in polymers have physical barriers from kinks and knots that serve as obstacles for the chains to slide passed each other. When temperatures pass $T_g$ for amorphous polymers and $T_m$ for crystalline polymers, these chains relax and allow them to move across physical joint boundaries in a process called reptation, shown in figure 2.6 [6]. Piere Gill de Gennes first proposed reptation theory in 1972 where molecular chain movement occurs from relaxation of defects. In other words, kinks in a polymer chain move towards the molecule's ends, making it wriggle similar to a worm or snake [37]. Reptate comes from the Latin root *reptare*, which means "to creep" and is the root of the word "reptile." Doi and Edwards further postulated that reptation occurs within the confines of a virtual tube formed by other surrounding molecules. Thus, chain relaxation is independent of the other polymer chains, making long range polymer chain diffusion in solutions and melts possible to approximate relative to chain length and molecular weight [38].

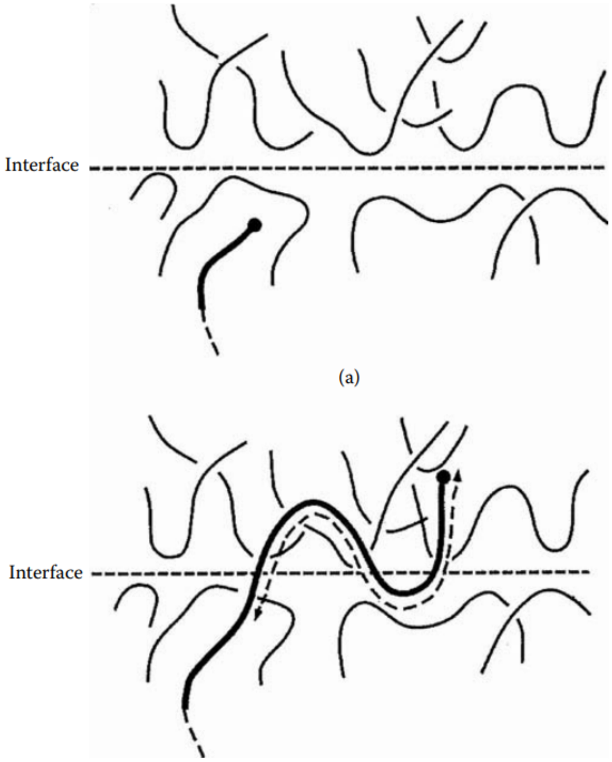

(a)

(b)

Figure 2.6: Schematic of chain movement across an interface: a) first contact and b) after having been in contact for some time, with a chain from one surface having reptated across into the interface of the adjoining polymer block. Adopted from [6].

Diffusion requires complete contact between the joining pieces. Unless substantial pressure conforms the joining pieces to each other, the polymer must flow at the joint to ensure contact. Polymer melts flow like a highly viscous liquid. Their viscosity is temperature dependent with the following relationship [39]:

$$\eta = Ae^{E^*/RT} \tag{2.2}$$

$A$ is a constant, $E^*$ is the activation enthalpy of viscous flow, $R$ is the gas constant, and $T$ is the temperature. Higher temperatures reduce the melt viscosity and promote improved polymer flow. The temperature dependency of polymer diffusion and flow tend to require liquid state welding processes due to short processing times. Polymers also have non-newtonian behavior with shear thinning characteristics. The complex flow behavior of polymer melts stems from viscoelastic properties. At high shear rates, the molecules stretch out which allows them to slide passed each other with less resistance [23]. When the flow stops, Brownian motion returns the molecular chains to an equilibrium state at a given temperature. The molecular elasticity creates a relaxation period of thickening viscosity [40]. In some cases, high stresses can also rupture macromolecular structures, creating a shear-thinning effect [23].

The complex material flow and diffusion restraints requires balancing welding parameters to facilitate adequate temperatures, polymer flow, and diffusion. These requirements necessitate special attention to polymer welding parameters, especially for mechanical welding methods.

Current welding technologies employed in joining polymers and polymer composites include laser welding, [41], press welding [41], ultrasonic welding [42], induction welding [43], and resistance welding [42]. Though these polymeric welding techniques differ in their process, they share the same fundamental principles of using heat to soften and melt the polymers at the joint. These welding methods typically require lapped configurations between the joining materials to allow for bonding of their surfaces.

## 2.3 Friction Stir Welding

### 2.3.1 Overview

Wayne M. Thomas, Edward D. Nicholas, James C. Needham, Michael G. Murch, Peter T. SMith, and Christopher J. Dawes of The Welding Institute (TWI) first applied for a Friction Stir Welding (FSW) patent on December 6, 1991 [44][3]. The process was originally intended as a solid-state technique to join metal alloys using a rotating tool, in which when applied under pressure to the joining surfaces, generates frictional heat to soften the metals and transfer material across the joint. Key attributes of FSW include those outlined in table 2.1:

---

[3] The original patent application is GB9125978.8 and is actually still "pending."

Table 2.1: A selection of FSW's key attributes. Summarized from [1].

| **Characteristic** | **Effect** |
|---|---|
| No filler material | Lightweight joints |
| Small heat affected zone (HAZ) | High joint efficiency |
| Material forging | Ability to join dissimilar materials |
| Low temperatures | Energy efficient |

With these key attributes, FSW found adoption for joining metallic materials in rail industries [45], maritime [46], automotive [47], aircraft [48], and spacecraft [49]. FSW's importance as useful manufacturing process also gained recognition in the fictional book *The Rocket Company* with its own chapter titled "Balloon Tanks, Fracture Mechanics, and Friction Stir Welding" [50].

The traditional form of FSW for metal joining utilizes a non-consumable tool with a shoulder and center pin, shown in figure 2.7. The rotating tool generates heat through friction and plastic deformation, which softens the material. As the tool rotates, material flows around the tool and mixes and consolidates. The tool shoulder overwhelmingly has the greatest heat contribution in metal FSW due to the large tangential velocities relative to the center pin [51].

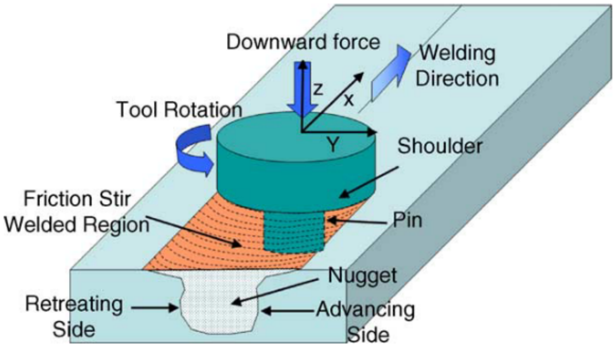

Figure 2.7: Schematic drawing of friction stir welding. Adopted from [1].

Shoulder and pin tools produce four main regions during metal FSW [52]. The base material (BM), or parent material, is the material unaltered by the welding process. The stir zone (SZ), or nugget, has refined grains due do direct interaction with the tool pin. The thermo-mechanically affected zone (TMAZ) extends beyond the SZ, where severe plastic deformation still occurs, but grain size varies based on its proximity to the tool pin. The heat-affected zone (HAZ) is characteristic of all welding forms where the base material experiences microstructural changes due to thermal cycling outside of the region of material flow. Coarsening of precipitates in the HAZ typically cause it to have the lowest strength.

### 2.3.2 Polymer FSW

Since its conception, FSW expanded to several commercial industries serving valuable purpose in many applications. Currently, FSW is not commercially used to join polymeric materials. Several attributes are responsible for polymer's lag behind metals in FSW applications. Since FSW was originally developed as a solid-state joining process for metals, researchers naturally did not apply FSW to polymeric materials until years later. In a review article, Seth Strand claims the first demonstration of polymer FSW occurred in 1997 [53]. However, this fact is subject to debate. Mattel Inc. offered a plastic welding toy kit in 1974 called the Spinwelder. The Spinwelder, in a time when many toys were still made in USA, was a portable battery powered device capable of bonding plastic parts and rivets using friction from the rotary tool. These toy kits were certainly ahead of their time and foreshadowed a remarkable manufacturing process. Perhaps the Spinwelder inspired early FSW researchers. The Spinwelder did not inspire the invention of metal friction stir welding though, as Wayne Thomas himself replied to a LinkedIn inquiry that he was unaware of the Spinwelder until several years after the first FSW patent. The actual inspiration for the FSW patent, he remarks, was his work with conventional friction welding and friction surfacing [54].

Though several early publications advance polymer FSW, the majority of research commenced within the last decade. Most research revolves around parameter optimization for joint strength, and the material subjects include similar joints between neat polymers, dissimilar polymer joints, dissimilar joints between polymers and metals, and the aforementioned with reinforced polymers.

#### 2.3.2.1 Polymer Specific Considerations

Unlike other polymer welding methods, FSW requires the joining materials to conduct heat throughout their thickness rather than confining heat conduction to their interfacial surfaces. Thermal conductivity is at least a couple orders of magnitude lower for polymers than metals. Take for example, high density polyethylene (HDPE) which is the most studied polymer in FSW research. HDPE's thermal conductivity $\kappa$ ranges between 0.38 $W/mK$ to 0.51 $W/mK$ depending on temperature, pressure, and crystalline content and is among the best thermal conductors of thermoplastics [23]. In contrast, pure aluminum has a thermal conductivity of 237 $W/mK$, and its alloys can have as low as approximately 80 $W/mK$ [55].

Polymers can have a self-lubricating effect during FSW [40, 53]. Additionally, polymers' low melt viscosity reduces frictional heat from the tool. Low melt-viscosity can also lead to expulsion of material from the weld zone, resulting in defects [14]. These behaviors exclusive to polymer FSW requires adaptation of the process from traditional metal FSW methods.

Excessive heat can also subject polymers to thermal degradation. Thermal degradation results in chemical alterations to the molecules in the form in chain breaking, molecular cleavage, and oxidation [23]. Thermal degradation can also promote chain cross linking that restricts crystal formation [56]. These effects ultimately hinder mechanical performance. Low thermal conductivity in thermoplastics results in high concentrated areas of heat in the weld zone with a high risk of thermal degradation. Polymer discoloration in the weld zone indicates degradation during FSW caused by prolonged heat concentration [57]. The Arrhenius Principle states that the time a polymer can withstand a particular temperature before undergoing thermal degradation is proportional to the following equation [23]:

$$t_{permitted} \propto exp(\frac{\Delta}{RT}) \tag{2.3}$$

where $\Delta$ is the activation energy of the polymer, $R$ is the gas constant, and $T$ is the absolute temperature. Thus, welding processes utilizing excessively high processing temperatures must have low processing times to limit thermal degradation.

#### 2.3.2.2 Material Flow

The low thermal conductivity of polymers and liquid state FSW changes the material flow characteristics compared to metals. Little computational modeling of material flow specific to polymer FSW currently exists. However, researchers apply principles from models intended for metal FSW to understand flow fields in polymers [9]. In many cases, metal FSW flow models apply to polymer applications since many of those models considers the metal in the TMAZ a highly viscous non-Newtonian fluid even though it remains solid throughout the entire metal FSW process [58, 59, 60, 61, 62]. FSW couples mechanical and thermal interactions between the tool and workpiece.

Figure 2.9a distinguishes in-process welding zones during FSW. A pre-heating zone preceeds the rotating tool where material begins to soften. Contact with the tool's leading edge provides the initial deformation of material. The material sweeps around the tool along the retreating side (RS) where it extrudes behind the tool, shown in figure 2.8. In many cases the material becomes forged back into the advancing side (AS) [10]. The AS experiences the greatest shear and temperatures since the tool rotation and material flow counters the welding direction.

The Arbegast Model distinguishes four material flow zones in metal FSW that recede behind the tool (figure 2.9b). Zones I and II pertain to material transfer along the AS and RS. Zone III is specific to shouldered tools that transfer material across the top surface into the weld zone. Zone IV lies along the bottom of the SZ/TMAZ where material from zone II can use as a path to transfer to zone I. Confinement of material flow in

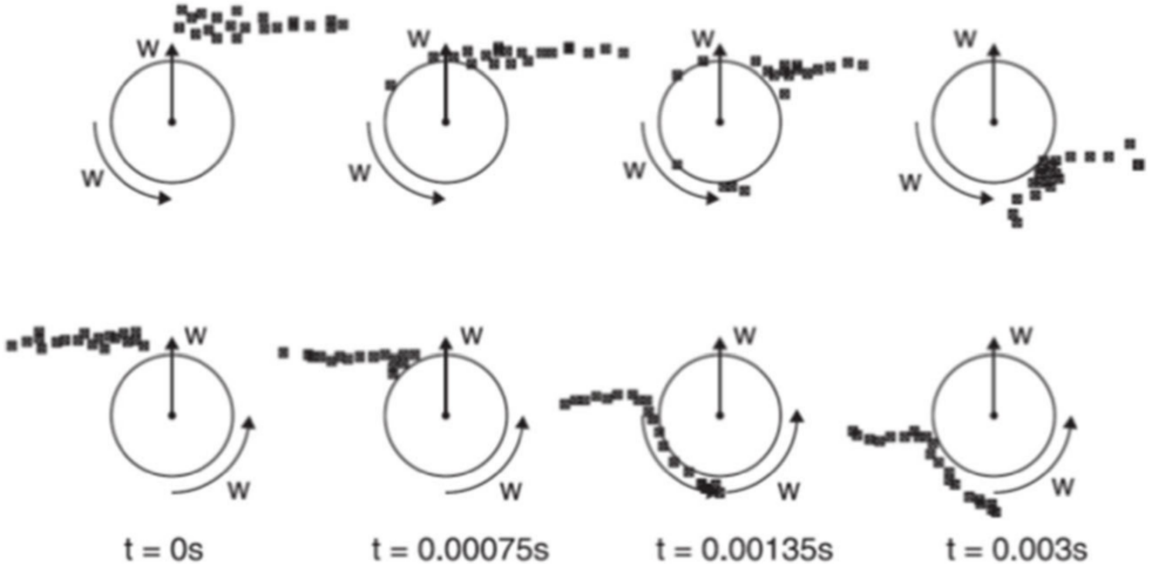

Figure 2.8: The material flow at advancing side (*above*) and retreating side (*below*) of the weld. Adopted from [7]. Figure originally from [8].

the SZ eliminates zones III and IV in polymeric FSW. Material flow confinement has been demonstrated with illustration of sharp and clear boundaries along the pin influence. [9]. The elimination of flow across zone III means that conventional FSW tools may only serve as containment of polymer in the weld zone rather than serving to transfer material.

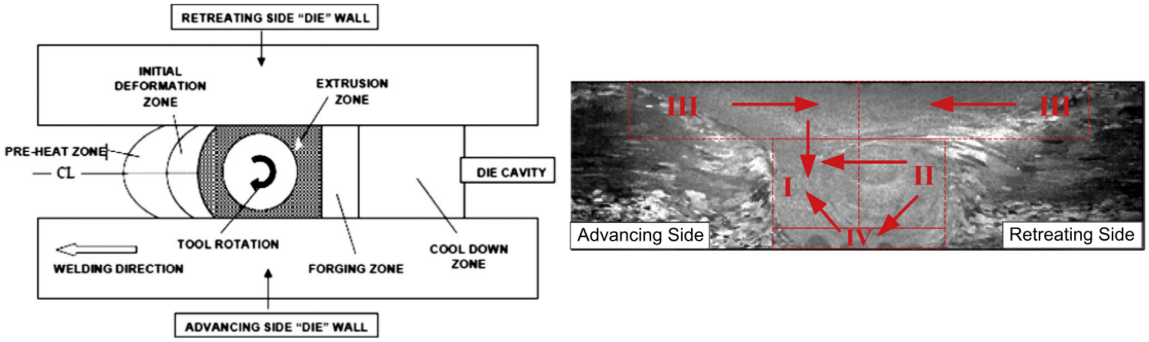

Figure 2.9: a) Representation of welding zones during FSW. Adopted from [9]. b) Post-weld material flow zones. Adopted from [10].

Joint failure locations characteristic to metal FSW and polymer FSW differ due to material interactions with respect to temperature. The AS experiences higher temperatures than the RS [63] which produce coarser grains in the HAZ adjacent to it in metals [1]. Reduced friction behind the tool can reduce the forging and consolidation of material along the AS during metal FSW [64]. Thus, large defects are more likely to form along the AS in metals [65]. For these reasons, the AS tends to be more prone to failure in metal FSW.

Contrary, the molten polymer pools during polymer FSW allows for forging along the AS behind the tool. The higher temperatures along the AS compared to the RS also promote greater diffusion across the joint. Lower pressures are also prevalent towards the RS behind the tool which can act as a vacuum to pull material away from the RS interface [66]. Thus, lower pressures along the RS and absence of zone IV in polymer FSW results in the higher likelihood of defects in these locations [7, 9, 67, 68].

#### 2.3.2.3 Tooling

FSW commences on rotary equipment such as specialized mill type machines. Contrary to machining tools, FSW tools are designed to heat and transfer material rather than remove it [69]. Fabricating tools from tool steel is sufficient for polymers and soft metals, while robust tools made from tungsten or polycrystalline cubic boron nitride (PCBN), are necessary for longer tool life when welding harder and abrasive materials [69]. The tool geometry affects the material flow and heat generation. Tooling fits in two subcategories: conventional FSW and stationary shoulder friction stir welding (SSFSW)[7], both of which were implemented in this dissertation. Conventional FSW refers to use of tools with a rotating center pin and shoulder. Shoulders can vary in diameter, curvature, and can contain variable features. Due to the large difference in relative tangential velocity between the shoulder and center pin, compromise for fast tool rotation speeds can result in material expulsion and overheating at the outer shoulder radius that degrades the polymer [57]. This problem does not arise in metal FSW since metals do not face chemically altering degradation and greater thermal conductivity alleviates large heat concentrations.

The center pin geometry has pronounced effects on the material flow in the SZ. The tool pin must generate frictional heat, disrupt the contacting surfaces, and transfer material from the leading edge behind the tool [69]. Figure 2.10 shows common tool pin geometries reported in FSW research. Pin geometry affects interfacial surface area between the tool and polymer, volumetric interaction, and flow velocity. Threaded tool profiles have been shown to facilitate both horizontal and vertical material flow in the weld zone with sound results [61, 70, 71]. For these reasons, threaded pins have been common place in the Vanderbilt University Welding Automation Lab research.

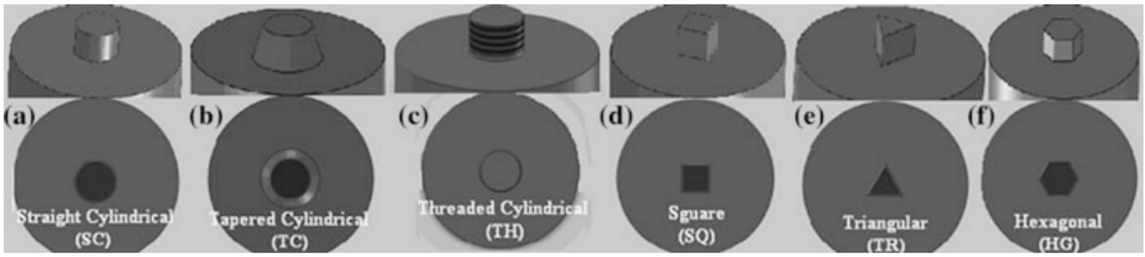

Figure 2.10: Different pin profiles of tool for FSW. Adopted from [11].

External heating methods help to supplement low frictional heat generated when friction stir welding polymers. Supplementary heat sources include hot plates under the weld pieces [67, 68], induction heated tools [72], and heated stationary shoulders [57, 73].

The heated stationary shoulder, or "hot shoe" was developed at Brigham Young University with a patent filed in 2001, shown in figure 2.11. A center pin protrudes through a floating shoulder and rotates independently while the shoulder remains stationary. The heated stationary shoulder applies heat to the workpiece while the rotating pin facilitates the mechanical stirring. The shoulder constrains the molten polymer in the weld zone to prohibit material expulsion and volumetric loss [74]. Conductive heat preheats the material in front of the tool while reducing the cooling rate of welded material behind the tool. A reduced cooling rate allows for uniform material shrinkage across the joint and limits defects upon cooling [12]. The reduced cooling rate also allows for improved crystalline growth in semi-crystalline polymers. SSFSW has proven to be an effective method for forming polymeric joints with joint efficiencies greater than 90% in a variety of thermoplastics including HDPE [57], Nylon 6 [75], wood/HDPE composite [76], polypropylene (PP) [12], PP/HDPE [77], and poylethylene terephthalate glycole (PETG) [78].

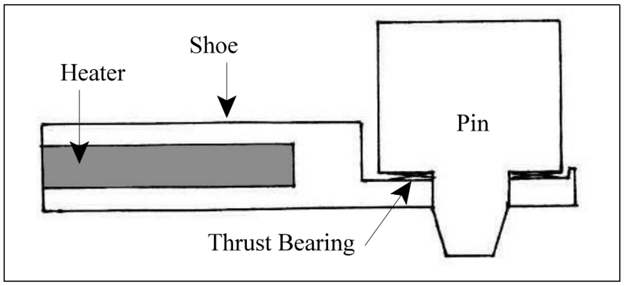

Figure 2.11: 2001 diagram of heated stationary shoulder ("Hot Shoe") from BYU. Adopted from [12]

#### 2.3.2.4 Parameter Optimization

FSW requires a harmony of finely tuned parameters to produce quality joints. Mechanical performance typically distinguishes a joint's quality, though visual surface appearance and cross-sectional analysis can expose defects that ultimately lead to poor joint performance. Common tune-able welding parameters include the tool rotation speed, welding/traverse speed, tool tilt angle, plunge depth, and tool dimensions. For heat assisted FSW methods, the temperature of the heat source is also a variable parameter.

Study of each parameter's influence on joint performance can require heavy experimentation to account for the wide range of possible parameter choices. Thus, researchers have employed experimental methods using a variety of design of experiments (DOE) to perform statistical analysis on parameter influence, identify parameter interactions, and create models to predict joint performance given a set of parameters.

Three common DOE classifications for testing multiple variables include full-factorial, response surface methodology (RSM), and Taguchi methods. Full factorial experiments test every combination between parameters. For example, testing two different parameters at three levels each requires $3^2$ or nine total combinations. Performing experiments with more parameters requires significantly more runs with full-factorial experiments, making their execution costly. RSM and Taguchi methods allow for strategic selection of parameter combinations to estimate influence of each parameter while significantly reducing the number of experimental runs. RSM's use methods of least squares to statistically fit parameter inputs to functional relationships with their outputs. RSM's are particularly useful to model parameter curvature, or nonlinear influence and identify dependent interactions with other parameters. Taguchi methods are more streamlined for parameter optimization often used in quality control and typically require fewer parameter combinations. Taguchi methods use the signal-to-noise ratio of parameter response from the mean response to optimize parameter choice. Though they can be a cost-effective solution for determining optimal parameters, Taguchi methods do not consider parameter interactions and thus provide less information when studying a specific parameter's influence on a response [79].

The degree of each individual parameter's contribution to joint performance can depend on other considered factors such as the welded material type and selected parameter range. Figure 2.12 compares the contribution of tool rotation speed, traverse speed, and tilt angle from two different studies that utilize a Taguchi method. Figure 2.12 shows results from FSW of a carbon fiber/polypropylene composite [13] and figure 2.12b shows results from FSW of neat HDPE [14]. Though both studies indicate very little influence from the tool tilt angle on mechanical strength, they disagree on the contribution from rotation and traverse speeds. Besides the welded material type, the range of rotation speeds also varies significantly between the two studies, which may indicate an interaction between the rotation and traverse speeds over a wider parameter range.

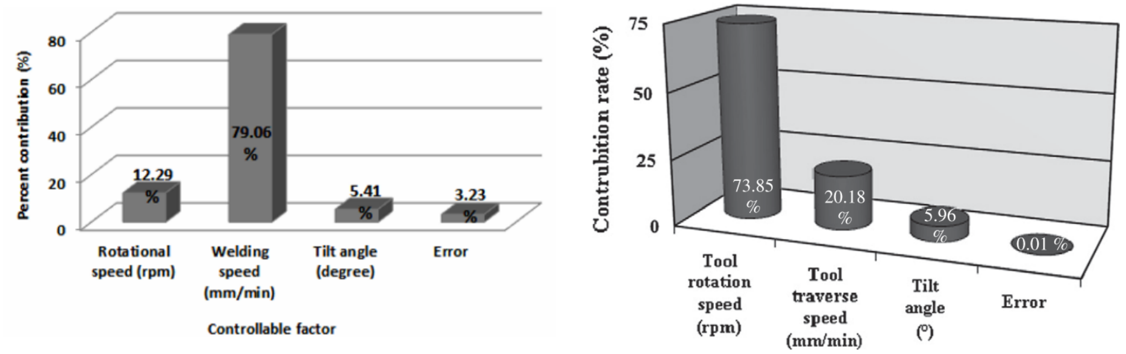

a)

b)

Figure 2.12: Polymer FSW parameter contributions from a)[13] and b) [14].

Statistical models of parameter inputs only approximate relationships between considered variables and careful consideration must be taken of the experimental conditions when evaluating those models. Take for example, conclusions from Rezgui et al., who performed an RSM considering the tool plunged surface, rotation speed, and traverse speed during FSW of HDPE [80]. Unlike the conclusions of figure 2.12, they conclude that the rotation speed has no statistical significance on joint strength in their experiments. However, Rezgui et al. uses a shoulderless tool (diameter of zero) unlike the tools used in the experiments by Ahmadi and Bozkurt [13, 14]. Thus, the absence of variable shoulder geometry in these studies confounds the interaction between rotation speed and shoulder diameter.

A general consensus, though, is that for conventional tools varying the tool rotation and traverse speeds have the greatest influence on joint strength in polymer FSW due to their influence on heat generation and heat flux to the material [81]. Thus, the tool rotation and traverse speeds should be of high consideration when researching FSW joints with new materials or configurations.

### 2.3.3 FSW Variant Processes

Several derivative processes use the same fundamental principles as FSW but utilize different tooling and tool paths for specific applications. Friction stir spot welding (FSSW) has the greatest similarity to traditional FSW as its major difference comes from the stationary tool contact location, shown in figure 2.13. FSSP typically occurs using conventional tools with convex shoulders to contain the molten polymer in the weld zone [82, 83].

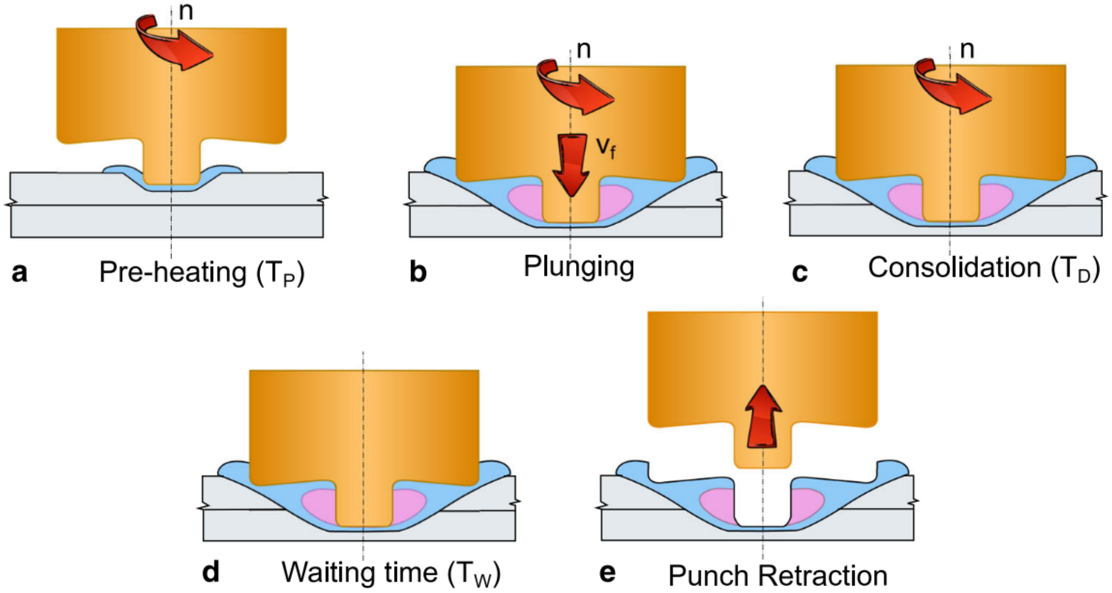

Figure 2.13: Typical phases of friction stir spot welding process: Preheating, joining, consolidation, and tool retraction. Adopted from [15].

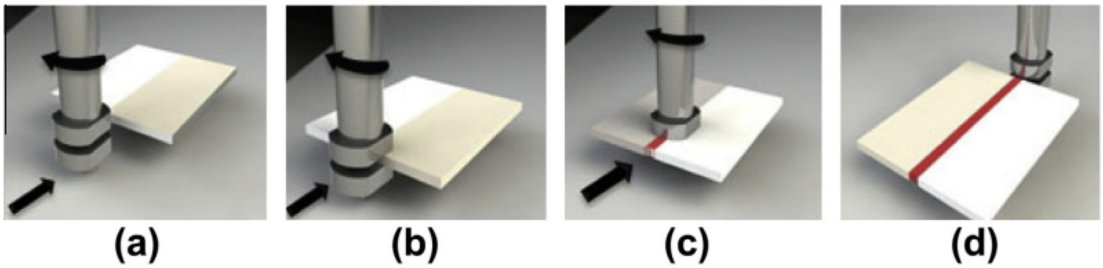

Figure 2.14: Diagram of SRFSW with double stationary shoulder tool. Adopted form [16].

Conventional FSW requires backing support underneath the work piece due to the tool's large axial force. Self reacting FSW (SRFSW) uses tool contact on both sides of the work piece, eliminating the need for support below the weld. SRFSW can come in the form of a bobbin tool with a pin between two rotary shoulders [84], or pin with double stationary shoulder design [16]. SRFSW allows for joining of enclosed geometries where a backing mandrel may be impractical, such as in the case of joining pipe sections [85].

Friction stir processing (FSP) is not a joining process. Rather, FSP applies modifications to the existing surface of a material. For polymers, FSP can introduce filler materials to form composites. The introduction of metals or clay particles to polymeric materials using FSP has been shown to change mechanical properties [17]. Most methods to form composites requires modification of the base material to accept the filler in the form of grooves or pre-drilled holes, shown in figure 2.15.

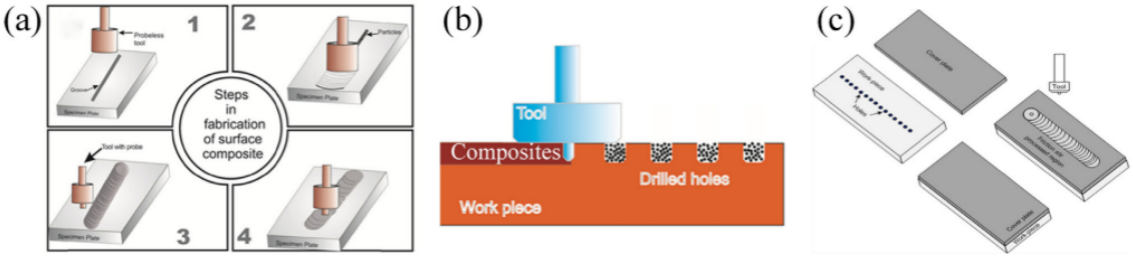

Figure 2.15: Common FSP material preparation methods a)milled grooves b) pre-drilled holes c) holes with cover plate. Adopted from [17]. Figure content originally from [18].

# CHAPTER 3

## Influence of Tool Thread Pitch During Friction Stir Welding of High-Density Polyethylene Plate

The following work was previously published in the *Journal of Manufacturing Science and Engineering* as:

L. T. Wilkins, A.M. Strauss, Influence of Tool Thread Pitch During Friction Stir Welding of High-Density Polyethylene, Plate. ASME. J. Manuf. Sci. Eng. December 2022; 144(12): 121010.

### Abstract

This study utilizes a face-centered central composite response surface design of experiments to determine the effects of thread pitch when friction stir welding high density polyethylene. The tool pin thread pitch, along with rotation and traversing speed, were varied so that models of the maximum tensile strength, tool temperature, and tool forces could be analyzed. Coarser thread pitches facilitated higher tensile strength than finer threads due to greater material velocity and overlap between the stir zone and base material. In the tested range, the thread pitch provided a 6% linear contribution to ultimate tensile strength, where welds with coarse threads had on average a 2.83 MPa increase in tensile strength over the fine thread tool. The greater circumferential pin surface area of fine threads caused a greater increase in tool temperature, though this did not correlate to stronger welds. Ultimately, the most interdiffusion across the polymer joint occurred with the coarser thread pitch and slow traverse speed due to prolonged joint exposure to the molten polymer weld pool.

### 3.1 Introduction

The push for more economical and efficient materials drives increased usage of lightweight plastics. Reducing a vehicle's weight by 10% can increase fuel economy by an estimated 5%-7% in an automobile [19]. Plastic applications includes but is far from limited to body panels, lamp lenses and screens, fuel and other liquid tanks, equipment housings, and wear items such as gears and bushings [19]. Integrating polymers into engineered structures requires the ability to join them to each other and dissimilar materials. Joining methods using mechanical fasteners, adhesives, and welding have different benefits, limitations, and applications.

Welding of polymers put simply, utilizes melting of thermoplastics to promote bonds that solidify after cooling. The bonds form through adhesion, which includes variants such as van der Waals forces, covalent bonds, capillary bonds, electrostatic bonds, magnetic bonds, mechanical interlocking, and interdiffusion [86]. Typically, no welding joint relies solely on only one of these adhesion mechanisms. Miscible polymers can achieve interdiffusion, where the molecules become intertwined across a joint, due to their homogeneous properties (i.e. similar glass transition temperature). Polymer interdiffusion can be described by the reptation model, where two similar amorphous polymers held together above their glass transition temperature will diffuse together [6]. The reptation model describes a polymer chain restricted inside of a hypothetical tube. The reptation time, $\tau$, is the time for the polymer chain to move completely, like a snake, through the hypothetical tube. $\tau$ is inversely proportional to the polymer's temperature, so higher temperatures will have faster interdiffusion, or movement of polymer chains across each other [6].

Of the many methods to join polymeric materials, friction stir welding (FSW) is an attractive process utilizing a rotating non-consumable tool to melt and blend polymers at their joining surface. FSW necessitates melting of the material only during joining of plastics. Seemingly unknown to many, FSW, patented by Thomas et al. in 1991 at The Welding Institute (Cambridge, UK) was originally intended for solid state joining of aluminum alloys and dissimilar metals [44]. It is considered an environmentally friendly manufacturing process since the low processing temperatures are energy efficient, no filler material is needed, and no gasses or fumes are produced. FSW polymers is not a solid state process since polymers consist of entangled chained molecules with different lengths that must melt for them to fuse across a joint [53]. Melting is necessary for welding plastics since a polymer chain cannot cross the path of another chain. Carbon, oxygen, and nitrogen typically construct these chains, and their bonds are arranged at various angles in solid form. When polymers melt, these molecular bonds can rotate freely allowing for entangled polymer chains to slip past each other [40]. Polymer structure is analogous to ramen noodles in a square pack. The dry noodles are entangled in a brick and no single noodle can be removed without breaking. After cooking and softening the noodles, it is possible to remove a now compliant noodle without rupturing it. An advantage with FSW is that it generates heat in both joining parts, allowing for welding of dissimilar polymers such as acrylonitrile butadine styrene (ABS) and polycarbonate (PC) [87]. Ultrasonic welding is an example where welding dissimilar polymers with drastically different melting temperatures is challenging since the vibrations during welding may melt one polymer and not the other [4].

Extensive studies have shown that parameter selection and tool geometry greatly affect the quality of friction stir welded joints in both metals and polymers [14, 88]. Polymers present additional challenges over metals to FSW due to their low thermal conductivity and limited range between melting temperature, $T_m$, and thermal degradation temperature, $T_d$. To weld polymers, the temperature in the weld zone must be high enough to allow slippage of polymer chains but cannot exceed temperatures that lead to degradation. Polymer degradation is a change in chemical or physical structure induced by factors such as excess heat or light that leads to reduction of strength or changes in other properties such as color and shape [89].

Tool geometries have an effect on heat generation, material flow and stress, welding forces, and ultimately

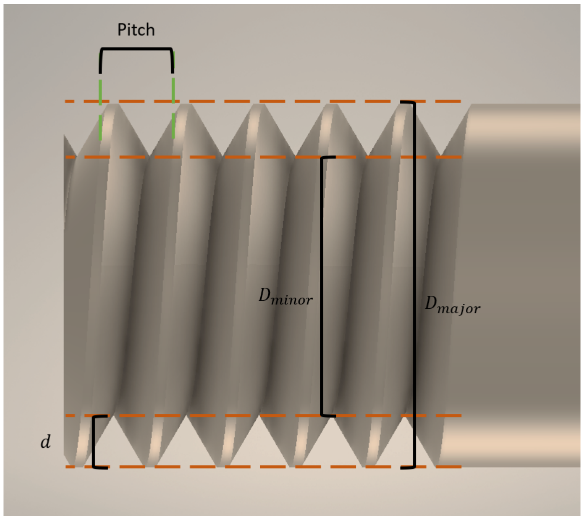

Figure 3.1: Components of thread specifications.

weld quality. For example, it has been shown that the number of edges on a tool pin for various geometries influences the material flow, temperature, hardness, strain, and welding forces. Generally, increasing the number of edges on a tool increases the temperature and traverse forces [84]. Tool pin geometries explored for FSW polymers include square [66, 77, 90, 91], triangular [11, 66, 77], cylindrical [13, 77, 90, 91], tapered [11, 13, 66, 90, 91], threaded cylindrical [11, 13, 71, 77, 90], and threaded tapered [11, 13], each of which exhibit different behavior. Triangular and square pins tend to have a pulsating effect which can provide good material mixing [91] but can also induce blow holes through the bottom of welded sheet [70]. Smooth cylindrical pins tend to poorly mix polymers resulting in very weak joints [91, 92]. Smooth tapered pins though tend to produce better quality joints than straight cylindrical geometries [92]. Several studies test threaded tool pins against non-threaded profiles. These studies, however, do not account for the thread pitch as a variable parameter. The thread pitch is the distance, typically in millimeters, between thread crests as illustrated in figure 3.1. Another metric is the thread count per unit length of the shaft, and is often described using threads per inch (TPI). For the threaded tools used, these studies conclude that threaded tool pins can form joints with high joint efficiency for different polymers [83] with lower linear force due to greater heat generation [70]. The increased heat generation from threaded pins is a result of increased surface heat flux from a larger interfacial surface area [61]. The orientation of thread flutes with respect to tool rotation direction also affects material flow and joint quality. Thread flute movement from the bottom of the tool to the material surface tends to pull the welded material out of the joint, whereas better joint quality is achieved by downward moving flutes that force material into the joint [71].

Researchers performed extensive studies pertaining to the effects of threads on FSW tools in polymers, but very little has been done to include thread pitch as an experimental parameter in FSW polymer optimization. However, varying thread pitch has been studied for various aluminum alloys. A study utilizing bead-on-plate welds for various aluminum alloys found that intermediate thread pitches were optimal for weld quality and reduction of defects [93]. The thread pitches ranged from 1.02 *mm* (25 TPI) to 3.18 *mm* (8 TPI) on large 15.9 *mm* diameter cylindrical pin tools. Welding forces and their relationship to thread pitch varied between aluminum alloys. Another study joining butted AA1080 plates found that larger thread pitches for a particular set of welding parameters has a drilling effect, where metal chips move up the tool and are expelled from the weld zone [94].

A thread pitch study was also conducted during friction stir spot welding (FSSW) of polypropylene (PP) plates where thread pitch ranged from 0.8 *mm* to 2.0 *mm* [90]. This study produced similar conclusions to that of Boz et al. [94], where a smaller thread pitch produced stronger welds and too large of a thread pitch expelled material from the weld zone.

The FSW community lacks studies pertaining to the effects of thread pitch during traversing polymer welds. Due to fundamental differences in material flow during FSW of alloys and polymers, thread pitch effects found in Rabby et al. and Boz et al. cannot be assumed to directly correlate to polymers. It has been shown that material flow during FSW polymers differs from that of metals, where polymers exhibit fewer material flow zones and a much smaller thermo-mechanically affected zone (TMAZ) [9]. Lateral weld fractures also tend to form along the retreating side due to lack of consolidation, whereas in metals defects tend to occur along the advancing side.

Former studies indicate that sound polymer joints with FSW requires finely tuned interacting welding parameters. The tool pin geometry plays a significant role in heat generation, material flow, and weld consolidation. Threaded pins can improve these functions over other pin types, but the field lacks studies pertaining to the influence of thread pitch during polymer welds. This study considers the influence of thread pitch on welded high density polyethylene (HDPE) tensile strength, tool temperature, and tool forces. Because welding parameters can have interaction with each other, tool rotation and traverse speeds are also considered. The effects of these parameters are tested using design of experiments.

HDPE consists of long hydrocarbon chains with very little branching [95]. Branching refers to architectures where short polymer chains protrude off of a long main chain [23]. These chains are formed by free radical addition polymerization of $C_2H_4$ repeated units. Polyethylene, a polyolefin resin, is by far the most commercially used polymer and can be processed into different forms [19]. HDPE is the most rigid of the polyethylene forms due to less than 7 branches per 1000 carbon atoms that allows for tight packing of polymer chains, making it a highly crystalline material [6]. It is also studied most often in the field of FSW compared to other thermoplastics with a presence in approximately 36% of publications as of 2018 [91].

Thus, its popularity in FSW and industry make it a good candidate to study the influence of thread pitch.

## 3.2 Materials and Tooling

FSW experiments occurred in the Vanderbilt University Welding Automation Lab (VUWAL) on a modified Kearney and Trecker Milwaukee Model K milling machine. External motors mounted to the machine controlled using Simulink provided precise automated operation. Three thread pitches were tested using varied tool rotation and traverse speeds in HDPE. The physical properties of HDPE used in this study are available from the data sheet by Polymer Industries [96].

Figure 3.2: Three tool thread pitches used in this study. a) 1.27 *mm* (20TPI) b) 0.79 *mm* (32 TPI) c) 0.58 *mm* (44 TPI).

Table 3.1: Pin specifications for each thread pitch type

| TPI | Pitch (mm) | $D_{major}$ | $D_{minor}$ | $d$ | $SA$ | $V_T$ |
|---|---|---|---|---|---|---|
| 20 | 1.27 | 6.35 *mm* | 5.26 *mm* | 1.09 *mm* | 231 $mm^2$ | 127 $mm^3$ |
| | | (0.250”) | (0.207”) | (0.043”) | (0.358 $in^2$) | (0.008 $in^3$) |
| 32 | 0.79 | 6.35 *mm* | 5.67 *mm* | 0.68 *mm* | 239.63 $mm^2$ | 82.36 $mm^3$ ) |
| | | (0.250”) | (0.223”) | (0.027”) | (0.371 $in^2$) | (0.005 $in^3$) |
| 44 | 0.58 | 6.35 *mm* | 5.87 *mm* | 0.48 *mm* | 243.37 $mm^2$ | 60.84 $mm^3$ |
| | | (0.250”) | (0.231”) | (0.019”) | (0.377 $in^2$) | (0.004 $in^3$) |

A modular FSW tool capable of holding removable pins was machined in house to allow for rapid tool changes between thread pitches. The tool pins were cut from H13 tool steel since tools steels can withstand large loads, high temperatures, and lots of friction [97]. H13 is often used for aluminum FSW making it suitable for polymer FSW since the loads required to weld aluminum are much higher. Three pins of 1.27 *mm* (20 TPI), 0.79 *mm* (32 TPI), and 0.58 *mm* (44 TPI) thread pitches, shown in figure 3.2, were threaded on a lathe using the “Sharp V” thread form described in Walker [98]. The threads were cut in a left hand orientation so that a clockwise rotation facilitated downward flow along the pin [71, 99]. Table 3.1 outlines each pin’s specifications pertaining to the thread pitch, where TPI is the thread count per inch, Pitch is the distance between a specific point between two consecutive threads, $D_{major}$ is the largest diameter of the thread, $D_{minor}$ is the smallest diameter of the thread, and $d$ is the thread depth [98], shown in figure 3.1. Note that $d = D_{major} - D_{minor}$. For a Sharp V thread, the thread depth can be calculated by:

$$d = \frac{0.866}{N} \tag{3.1}$$

where $N = TPI$. $SA$ refers to the total thread surface area on both sides of the thread crest. $V_T$ is the total volume of space within the threads. These values pertain to a threaded pin 6.35 *mm* in length. Thread pitches were chosen to encompass the optimum parameters reported in Bilici et al. [90]. Extremely coarse threads were avoided to prevent milling of the polymer in the weld zone.

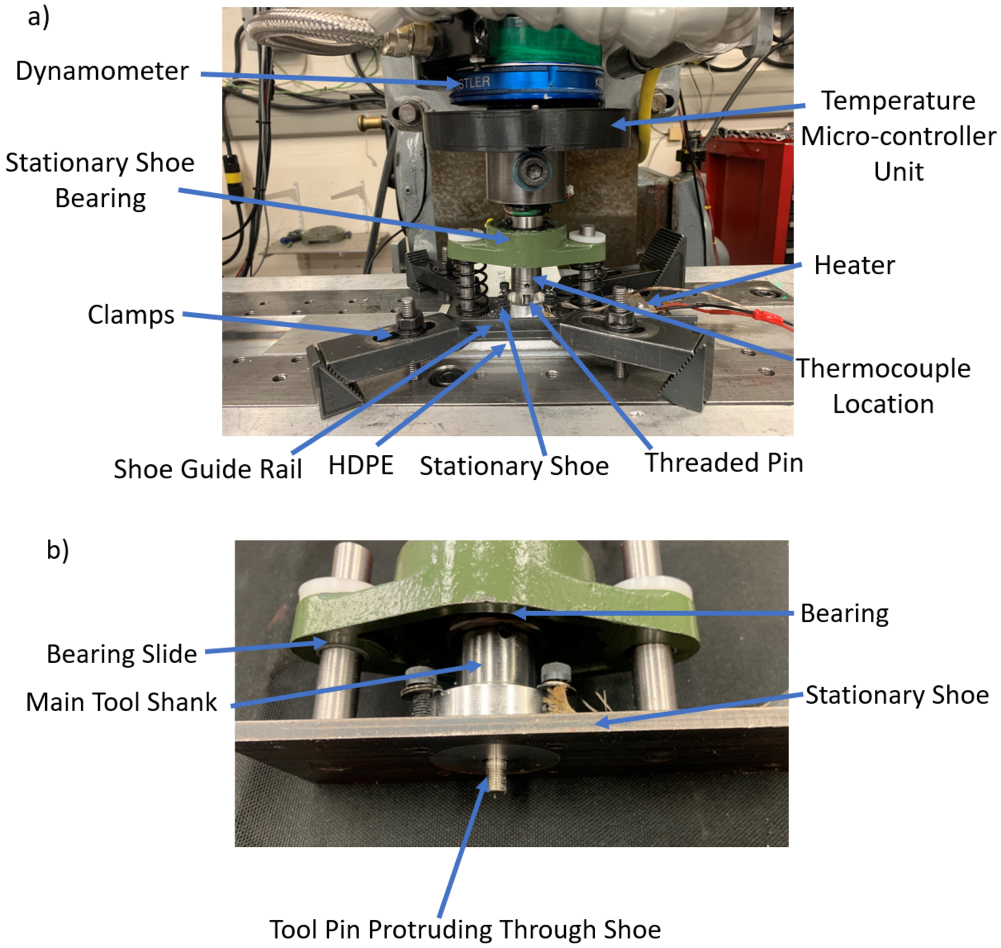

Figure 3.3: a) Diagram of tooling setup. The dynamometer measures welding forces. The temperature micro-controller unit collects data from a thermocouple located inside the tool shank. A bearing mounted to the tool shank centers the pin with a hole in the shoe. b) Underside of stationary shoe. The tool pin protrudes through a hole in the shoe when plunged.

The tested rotation speeds were 1000 RPM, 1250 RPM, and 1500 RPM, and the traverse speeds were 25.4 $mm/min$, 63.5 $mm/min$, and 101.6 $mm/min$. The shoulderless tool rotated within a stationary shoe heated to $65°C$ at the shoe's tool opening with zero tilt. Stationary shoes prevent ejection of molten polymer during the welding process [9]. Heating the stationary shoe aids in controlling the welded polymer's cooling rate, reducing voids induced from fast shrinkage and ultimately improving the weld quality [17, 31]. A pillow block bearing was fixed to the tool shank. Floating spring loaded slides guided the stationary shoe to follow the tool and apply pressure to the work piece as it traversed. Guide rails clamped to the work piece prevented the shoe from rotating with the tool.

A thermocouple inside the main tool shank measured the tool temperature during the entire welding process, allowing for the authors to infer heat generated from the tool temperature change since the tool ultimately conducts a portion of the heat generated [100]. Measuring the temperature inside the tool isolated the measured temperature changes from the shoe's heat input so that only the tool parameter effects were observed. The thermocouple is located at the top of the tool pin 34 *mm* from the weld centerline and connects to a Teensy LC microcontroller mounted on the tool spindle that stores the temperature data on a micro SD card. Temperature data collection is activated by an accelerometer that senses tool rotation. Tool temperature change was calculated using the difference between the minimum and peak value measured during each weld. The tool was cooled to room temperature before the start of each weld and it reached peak temperature before tool retraction. Therefore, the minimum and peak tool temperatures correspond to the temperature prior to tool plunge and at tool retraction. The values were normalized against the time duration since the traverse speed affects the welding time.

A Kistler type 9123C dynamometer measured forces experienced on the tool in the axial and planar directions. Welding forces were analyzed by first applying filters to the raw data from the dynamometer. The largest contributor to signal noise indicated by the frequency spectra of the data sets is the tool rotation frequency. Thus, low band pass filters with cut off frequencies of 10 Hz, 15 Hz, and 20 Hz were applied to 750 RPM, 1125 RPM, and 1500 RPM data sets, respectively.

Mechanical tests followed the ASTM D638-14 guidelines to characterize tensile strength. Specimens used in tensile testing were precisely cut using a Shapeoko XXL CNC router. Figure 3.3 provides a schematic and shows the real setup of the FSW tooling used in this experiment, outlining the dynamometer, temperature measurement system, and stationary shoe.

### 3.2.1 Design of Experiments Method

A series of bead-on-plate welds followed a face-centered central composite (FCC) design of experiments. The bead-on-plate configuration was chosen to reduce variation in experimental setup from variables such as surface roughness between butted plates and possible tool offset from machine backlash. Joint configurations also play a role in the strength and joint characteristics [101], so the bead-on-plate configuration was used to provide a simple foundation. An FCC design is a type of response surface methodology (RSM), which are useful for analyzing problems where multiple variables influence the response. In essence, a fitted model with two parameters produces a three-dimensional surface, hence the name RSM [79]. FCC designs are beneficial for three factor experiments because they only require three levels for each parameter, requiring fewer runs, and consequently resources, than uniform-precision designs. Because tool parameters tend to have quadratic effects on material strength [80], a second order model is necessary to describe the parameter response and requires a minimum of three parameter levels to do so [79]. A cube can signify a three level design, with each cube axis representing a range of values for a respective parameter. Each corner of the cube lies at a minimum or maximum. The FCC design uses data points from each corner, face center, and the cube center. A disadvantage of the FCC design is that it is non-rotatable, meaning some biases can occur since the corner and face points are not equidistant from the center [79]. However, FCC designs utilize center points that allow for a good estimate of experimental error.

Table 3.2: A 3 level, 3 factor response surface design of experiments using these values.

| **Symbol** | **Level** | -1 | 0 | +1 |
|---|---|---|---|---|
| A | **Thread Pitch** (mm) | 1.27 (20 TPI) | 0.79 (32 TPI) | 0.58 (44 TPI) |
| B | **Rotation Speed** (RPM) | 750 | 1125 | 1500 |
| C | **Traverse Speed** ($mm/min$) | 25.4 | 63.5 | 101.6 |

The design utilized three parameters each with three levels, requiring a total of 20 runs with six repeated center point runs. Replicates for selected non-repeated runs were added to the experiment to refine the models from experimental error and investigate unusual observations. Minitab statistical software generated a random order to complete the runs. Table 3.2 outlines the values for each parameter level. The parameter levels were determined using observations and data from preliminary experiments and scientific literature review. A summary of optimum FSW joining parameters for various polymers is shown in a literature review by Zafar et al [83]. The thread pitch levels are determined by equally spaced thread counts, where the center point is the average thread count of the high and low levels. Thus, the low level has smallest thread count, but the largest thread pitch. The high level has the greatest thread count, but the smallest thread pitch. Thread pitch, rotation speed, and traverse speed will be referred to as A, B, and C respectively moving forward. Responses included the tool axial and planar forces, tool temperature change from tool plunge to tool retraction, and average tensile data between five specimens from each run. Table 3.3 shows the experimental design with the response values. “Run” is the group number of each combination of parameter levels. “Run Order” refers to Minitab’s randomized order in which each run was completed. The responses were analyzed using Minitab’s response surface analysis tools.

## 3.3 Results

## 3.4 Maximum Tensile Strength

Figure 3.4 shows the surface of completed welds for each parameter combination. The highest experimental maximum tensile strength was 23.18 MPa using A = 1.27 mm (20TPI) , B = 1500 RPM, and C = 25.4 $mm/min$. This results in an 89% joint efficiency from the 26.0 MPa measured in virgin material.

Table 3.3: FCC DOE with responses.

| Run | Run Order | Thread Pitch | RPM | IPM | Max T.S. (Mpa) | dT/min | Plunge Force (N) | Planar Force (N) |
|---|---|---|---|---|---|---|---|---|
| 1 | 13 | -1 | -1 | -1 | 16.37 | 1.42 | 951.11 | 124.8 |
| 2 | 3 | 1 | -1 | -1 | 9.54 | 2.36 | 1344.4 | 166.9 |
| 3 | 2 | -1 | 1 | -1 | 23.18 | 2.9 | 748.9 | 106.1 |
| 4 | 18 | 1 | 1 | -1 | 18.54 | 3.41 | 606.96 | 72.3 |
| 5 | 9 | -1 | -1 | 1 | 8.29 | 1.33 | 976.18 | 398.1 |
| 6 | 7 | 1 | -1 | 1 | 6.98 | 2.77 | 1416 | 497.1 |
| 7 | 8 | -1 | 1 | 1 | 5.58 | 3.23 | 509.3 | 225.2 |
| 8 | 15 | 1 | 1 | 1 | 6.23 | 3.91 | 880.99 | 234.9 |
| 9 | 17 | -1 | 0 | 0 | 6.81 | 2.39 | 601.26 | 256.2 |
| 10 | 12 | 1 | 0 | 0 | 4.8 | 3.15 | 806.82 | 389.8 |
| 11 | 10 | 0 | -1 | 0 | 6.42 | 1.84 | 1013.1 | * |
| 12 | 4 | 0 | 1 | 0 | 18.38 | 3.63 | 643.17 | 128.9 |
| 13 | 5 | 0 | 0 | -1 | 20.49 | 2.11 | 733.52 | 88 |
| 14 | 14 | 0 | 0 | 1 | 7.09 | 2.82 | 863.22 | 355.3 |
| 15 | 11 | 0 | 0 | 0 | 5.9 | 2.28 | 928.21 | 202.1 |
| 16 | 1 | 0 | 0 | 0 | 5.18 | 2.64 | 858.6 | 204.8 |
| 17 | 19 | 0 | 0 | 0 | 6.75 | 2.5 | 847.34 | 207.2 |
| 18 | 16 | 0 | 0 | 0 | 6.63 | 2.36 | 750.43 | 201.8 |
| 19 | 20 | 0 | 0 | 0 | 6.04 | 2.6 | 864.6 | 192.2 |
| 20 | 6 | 0 | 0 | 0 | 6.19 | 2.32 | 852.39 | 195.6 |

* indicates failed data measurement.

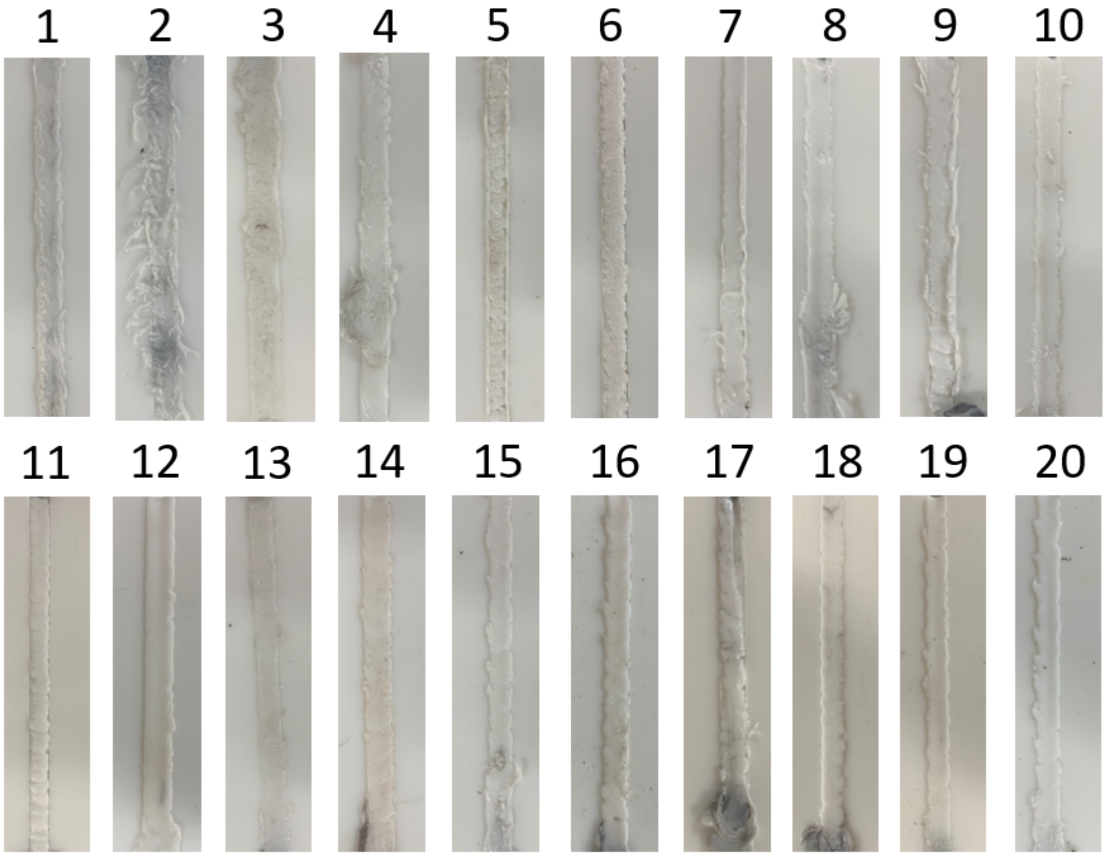

Figure 3.4: Weld sections for each completed weld run. Each weld label refers to “Run” parameters outlined in table 3.3.

Minitab by default produces a response surface model consisting of all parameters, square of these parameters, and 2-way interactions. Each term in the model has a combination of parameter values multiplied by a coefficient. For example, an interaction term between thread pitch and rotation speed will look like $\beta_{ij}A*B$, where $\beta_{ij}$ is the coefficient corresponding to their contribution to the model, and A and B are the respective parameter values. Five terms are statistically significant at a 95% ($\alpha = 0.05$) confidence interval with their F and P values displayed in table 3.4. The critical F and T values ($F_{crit}$ and $T_{crit}$) were calculated in Minitab, where $F_{crit} = 3.885$ and $T_{crit} = 2.093$. A statistically significant parameter term has $P < \alpha$ and $F > F_{crit}$ when using an F test and $|T| > |T_{crit}|$ when using a T test. Removing all of the terms incorporating thread pitch improves the coefficient of determination ($R^2$) for the model. However, the lack of fit (LOF) parameter has a P-value of $p = 0.000$. When $p \leq 0.050$, the lack of fit has significantly more error than the pure error, and the regression model does not adequately describe the data, even if the data has a good fit to it [79]. Upon further investigation, it was found that the model residuals were skewed to the left, shown in figure 3.5. The default models assume that the residuals are normally distributed which can skew model predictions due to non-constant variance of the observations. Non-normal residual distributions can lead to inaccurate parameter significance levels [79]. Applying a variance-stabilizing transformation can normalize an error distribution.

Table 3.4: Significant values for non-transformed maximum tensile strength model response. $F_{crit} = 3.885$.

| **Effect** | **F-value** | **P-value** |
|---|---|---|
| C | 43.49 | 0.000 |
| CC | 9.87 | 0.010 |
| B | 9.63 | 0.011 |
| B*C | 6.63 | 0.028 |
| $B^2$ | 5.01 | 0.049 |
| LOF | 41.54 | 0.000 |

A Box and Cox transformation was applied to the tensile data. The estimated transformation coefficient is $\lambda = -0.84$, where $y* = y^{\lambda}$ is the transformed data points and $\lambda = 1$ applies no transformation to the data. The 95% confidence interval for $\lambda$ is (-1.91,0.18). Since $\lambda = 1$ does not reside within the bounds of the confidence interval, continuing with the transformation is appropriate. Minitab determined $\lambda$ using the *Optimal* $\lambda$ Box Cox transformation function, and rounded the transformation coefficient to $\lambda = -1$, which corresponds to an inverse transformation. Figure 3.5 shows that the model residuals of the transformed data follow a closer resemblance of a normal distribution with the residuals centered around zero. A new model

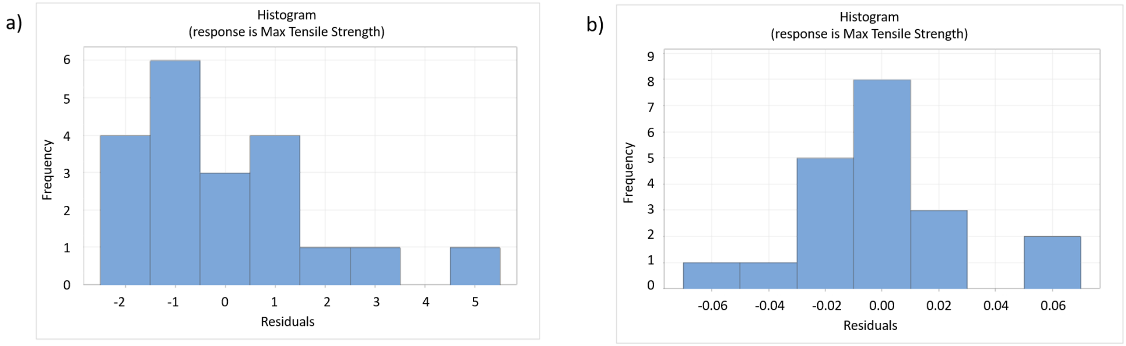

Figure 3.5: a) Residual distribution for non-transformed tensile strength data. The residuals are skewed to the left and do not have a normal distribution. b) Residual distribution of transformed maximum tensile strength data.

for the maximum tensile strength including the terms in table 3.5 followed the transformation. The coded coefficients in table 3.5 form equation 3.2, and their order reflects their contribution to the maximum tensile strength, TS:

$$
\begin{aligned}
TS = & \\
& -0.15632 - 0.04148C + 0.0487C^2 - 0.0386B^2 \\
& -0.0339A^2 - 0.01737A - 0.01604BC + 0.01107B
\end{aligned}
\tag{3.2}
$$

Table 3.5: Effects used in reduced transformed model response for maximum tensile strength. The coded coefficients are based on the scale of values between -1 and 1 for the parameters in table 3.2. $T_{crit} = 2.093$.

| Effect | Coded Coefficient | T-value | P-value |
|---|---|---|---|
| Constant | -0.15632 | -18.17 | 0.000 |
| C | -0.04148 | -5.24 | 0.000 |
| $C^2$ | 0.0487 | 3.23 | 0.007 |
| $B^2$ | -0.0386 | 2.56‘ | 0.025 |
| $A^2$ | -0.0339 | -2.24 | 0.044 |
| A | -0.01737 | -2.19 | 0.049 |
| B*C | -0.01604 | -1.81 | 0.095 |
| B | 0.01107 | 1.4 | 0.187 |
| LOF | | 0.098 | 3.40 |

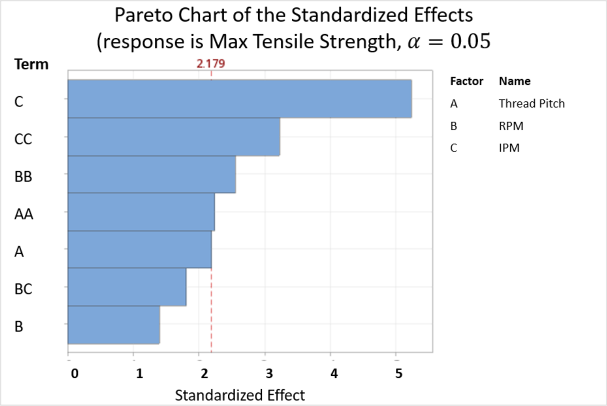

Figure 3.6: Pareto chart of standardized effects in reduced transformed model. The dotted red line signifies the threshold for statistical significance at a 95% confidence interval, where all terms extending to the right of the dotted line are statistically significant.

The reduced transformed model has linear, square, 2-way interaction, and error contributions of 43.22%, 37.48%, 4.15%, and 15.15%, respectively. The high contribution of square terms confirms curvature in the model response and that three levels were indeed necessary for this study. C, $C^2$, $B^2$, $A^2$, and A are statistically significant terms in the reduced model with 34.67%, 13.16%, 20.86%, 3.46%, and 6.08% contribution. Parameter contribution is calculated by the percentage of the respective term's sequential sum of squares to the data's total sequential sum of squares. Sequential sum of squares measure variation in the response from each parameter. Figure 3.6 shows a Pareto chart of the terms included in the reduced transformed model for maximum tensile strength. The magnitude of each parameter's standardized effect is related to their contribution to the model response. B is left in the model to satisfy hierarchical effects, and B*C interaction improves the overall fit. The coefficient of determination for the reduced transformed model is $R^2 = 84.85\%$, $R^2(adj) = 76.01\%$, and $R^2(pred) = 48.10\%$. The lack of fit is well beyond the threshold of statistical significance with $p = 0.098$. Though the regression has room for improvement, the lack of fit suggests that the model is a good representation of the parameter effects. The low $R^2$ values are similar to the outcome reported in Rezgui et al.'s HDPE FSW parameter study [80]. Their study used a slightly wider range of rotation speeds and a lower range of traverse speeds with a smaller center point.

Figure 3.7 shows the individual parameter contribution to tensile strength. The significance of the squared model terms is visually apparent due to the parabolic response when sweeping each parameter across its range. The minimum/maximum parameter responses in figure 3.7 indicate that the chosen parameter ranges were sufficient to capture the general behavior of parameter values. Figure 3.8 also visualizes this behavior through 3D surface plots. Increasing traverse speeds sharply decreases the ultimate tensile strength when sweeping through the center point, while sweeping between the center point and high value has a smaller contribution to tensile strength. Rotation speed has a predicted minimum effect on tensile strength just below its center point, though overall the higher rotation speeds tend to promote greater tensile strengths as found in other studies [14]. The linear effects of rotation speed does not have statistical significance, nor does it in Rezgui et al. [80]. Studies finding significant contribution from the rotation speed implemented higher rotation speeds than this study [14], but exceedingly large rotation speeds hinder weld strength from material expulsion and degradation [102]. The local minima near the center point for both rotation speed and traverse speed may suggest some interaction between the two parameters. Though no parameter interaction provided statistically significant contribution to the ultimate tensile strength, the B*C interaction does improve the model fit. In the case of this study, every run incorporating the center point parameter values for both B and C resulted in tensile strength values below 7 MPa regardless of thread pitch. In some cases where only B or C had a center point parameter value, tensile strength greatly improved.

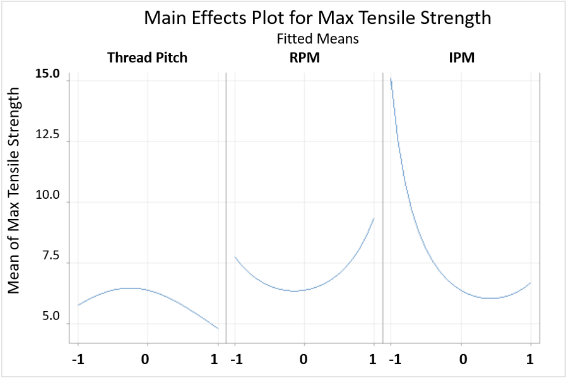

Figure 3.7: Effects for main parameters on maximum tensile strength.

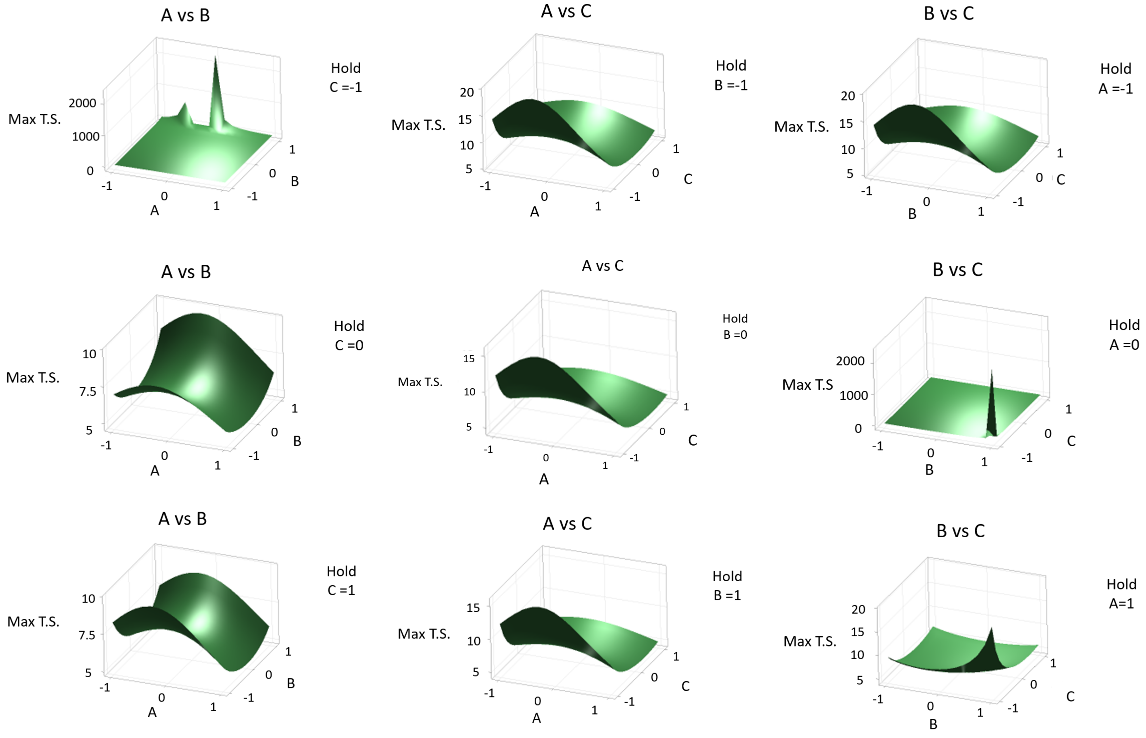

Figure 3.8: 3D surface plots for parameter relationship with maximum tensile strength as the response.

Thread pitch shows significant quadratic effects in the model with a local maxima between the low and center point parameter values. The linear thread pitch term suggests that generally the coarser threads in this study produce welds with higher tensile strength. On average, the 1.27 *mm* pitch threads provide 2.83 MPa over the 0.58 *mm* pitch threads. The model predicts a drop off in tensile strength at the coarse thread pitch in this study, though the response of the -1 thread pitch is still significantly higher than the +1 thread pitch. This may be an slight indication of the milling effect described in Boz et al. [94], though significant milling was not observed. As threads become finer and finer, the pin geometry approaches that of a smooth cylindrical pin, which as noted before perform poorly compared to other pin geometries. Thus, the downward curvature nature of the thread pitch response on tensile strength is expected.

Run 12 is labeled as an unusual observation with a disproportionally large residual, potentially making it an outlier in the data. The weld logs were checked for run 12 with no obvious issues. Further replicate trials of run 12 produced similar results, so the original data was left in the model. Removing run 12 from the model all together did not improve the regression or fit either. The poor regression model may be a product of non-rotatability in the FCC design. In the cube model described before, runs 1-8 are all radially equidistant from the center points due to their extremums along all three axes. Runs 9-14 are all radially closer to the center points since their parameters put them at an extremum along only one axis. Thus, the variance of the predicted response is not equal in all directions from the cube center [79]. Further evidence of the effects of non-rotatability are the extreme model predictions shown in plots “A vs B” and “B vs C” in figure 3.8. Both plots predict unrealistic maximum tensile strengths when A, B, and C are all at their optimum values.

### 3.5 Tensile Fracture Surface

The fractured tensile specimens displayed clear patterns on break morphology when categorized by thread pitch. All specimens ruptured on the retreating side of the weld zone. Polymers tend to rupture at the retreating side distinctly along the tool pin’s path since the thermo mechanically affected zone (TMAZ) is limited to the stir zone during FSW of polymers [9]. The smaller TMAZ size in polymers compared to metals is a result of polymers’ low thermal conductivity. Higher stresses on the tool advancing side tend to fully consolidate the stirred polymer with the base material. The higher stresses arise from molten polymer being pulled around from the back side of the pin, which is then extruded into the advancing side. The retreating side experiences a smaller forging pressure, which results in less consolidation at the stir zone wall [9].

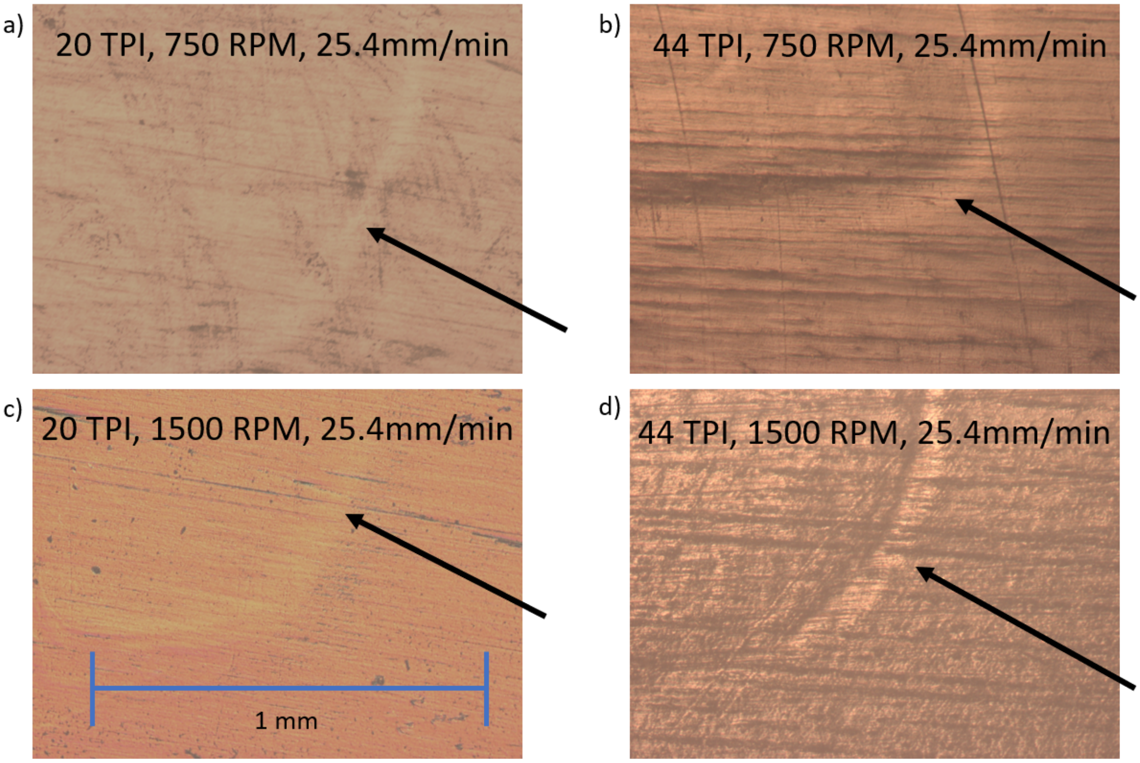

Figure 3.9: Micrographs of weld cross sections located at the bottom of the weld retreating side. The arrows point to defects at the weld zone interface. a) Run 1. b) Run 2. c) Run 3. d) Run 4.

The first eight runs with the +1 and - 1 thread pitch levels follow a $2^3$ full factorial design, consisting of two levels for each parameter. Runs 9 and 10 use +1 and -1 level thread pitch with center points for rotation speed and traverse speed. Thus, the fracture surface for each thread pitch can be compared between rotation/traverse speed pairs. Figure 3.9 shows micrographs of weld cross sections at the weld retreating side for coarse and fine thread welds at high and low rotation speeds. For both rotation speeds, the coarse threads show enhanced polymer interdiffusion between the weld zone and base material over the fine thread tools as indicated by a fainter defect line visible at the stir zone interface. Figure 3.9 also lacks a heat affected zone (HAZ) far beyond the stir zone, which is common for polymer FSW [83]. Figure 3.10a indicates fracture between the stir zone and base material along the retreating side of the weld, which was observed for all runs. Figure 3.10b shows fracture surfaces of coarse and fine thread tensile specimens. Lightly applied brushed gold paint adhered to the high spots on the fracture surface to provide distinction between the fracture surfaces. In general, the fine thread pitch specimens tend to have a consistent vertical break at the stir zone/retreating side interface, with a surface reflective of the tool threads. The tool thread shape at the interface reveals a kissing bond, where the polymer flows to fill the cavity left by the tool but adheres mostly between the joint surfaces. The coarse thread pitch specimens have less distinct fracture patterns that indicate fewer kissing bonds than seen in the finer thread pitch specimens. The less distinct fracture pattern in the coarse thread specimens may be a result of greater interdiffusion across the joints induced by greater mixing. The coarse thread tool provides a greater overlap between the stir zone and base material with a thread depth of over double that of the fine thread tool, shown in table 3.1. Furthermore, the coarser threads have a higher velocity of material in the thread grooves, which facilitates greater volumetric heat generation in the shear layer around the tool [61] and aids in polymer interdiffusion.

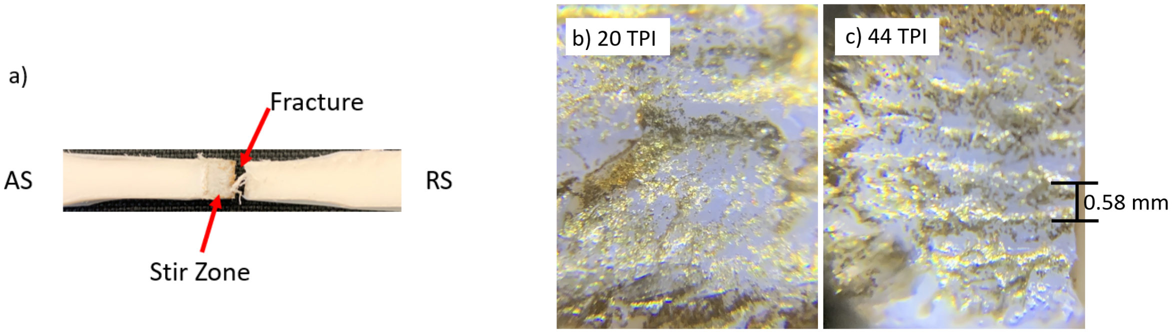

Figure 3.10: a) Fractured tensile specimen. b) Coarse thread fracture surface. c) Fine thread fracture surface. Surfaces are coated with gold paint to show texture. Scale shows fracture surface has spacing of the thread pitch.

### 3.6 Tool Temperature

Residuals for the increase in tool temperature had a relatively normal distribution with Minitab's standard model, so no transformations were necessary. The reduced model includes all three main effects and one interaction effect, where the interaction effect is the only non-statistically significant term. Rotation speed has the greatest contribution to tool temperature (63.84%), followed by thread pitch (22.14%) and traverse speed (4.10%). Each parameters' contribution to temperature response is illustrated by the Pareto chart of standardized effects, shown in figure 3.11. The reduced tool temperature model fits well to the data with $R^2 = 92.16\%$, $R^2(adj) = 90.07\%$, $R^2(pred) = 85.52\%$. All three parameters have a linear relationship with tool temperature, shown in figure 3.11, and have very little interaction with each other. Figure 3.12 shows surface plots between each parameter and highlights the lack of curvature with the nearly flat surfaces. Increasing the thread count (reducing thread pitch), rotation speed, and traverse speed all result in higher tool temperature. The surface heat generation at the tool and substrate contact interface can be described by equation 3.3 [61]:

$$q(r) = \kappa[\delta \cdot \tau_y + (1-\delta) \cdot \tau_f] \cdot \omega r \tag{3.3}$$

$\kappa$ is a constant related to contact area dependent on thread shape. $\delta$, known as the slip rate, is the relation of flowing work piece velocity $v_m$ to the tool velocity $v_t$ at the contact interface. $\tau_y$ is the shear yield stress, $\tau_f$ is the friction stress, $\omega$ is the tool rotational velocity, and $r$ is the tool radius. The reader is encouraged to refer to Sun et al. [61] for more information regarding equation 3.3. The linear parameter effects on tool temperature in this study agree with the relationships found in Sun et al.'s model. Since $\kappa$ relates to increases in contact area, an increase in the thread surface area from a lower thread pitch will increase the heat generation. Sun et al. demonstrates in their model that the thread pitch affects surface heat generation and volumetric heat generation inversely to each other. Heat is generated in the FSW process by both friction at contact surfaces and through plastic deformation in the material shear layer. Smaller thread pitches have greater surface area, which increases heat generated at the interfaces along the threads. Conversely, less heat is generated in the shear layer between the threads with a small thread pitch, partially because the increased contact temperatures reduces the material flow stress. Therefore, the tool surface area dominates the heat generation for the thread pitch contribution. Temperature profiles that show increased total heat generation from finer threads can be seen in Sun et al. [61].

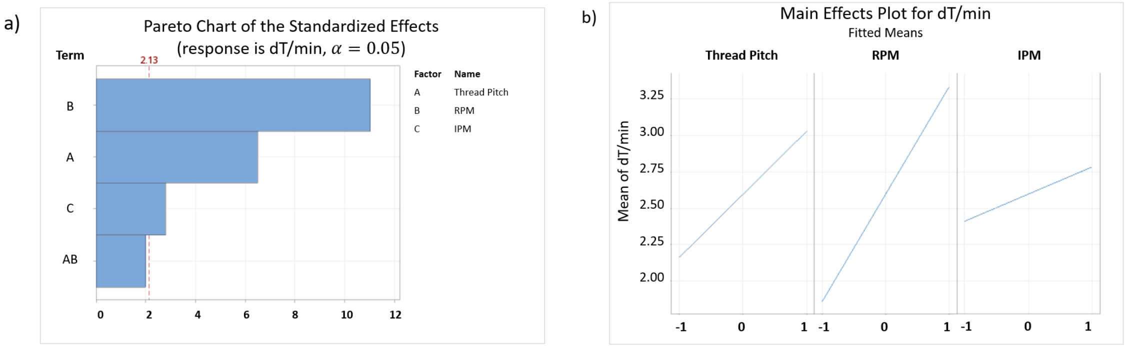

Figure 3.11: a) Pareto chart of reduced model for tool temperature change. Rotation speed, thread pitch, and traverse speed are statistically significant effects. b) Main effects for increases in tool temperature. Each parameter has a linear relationship with temperature increase.

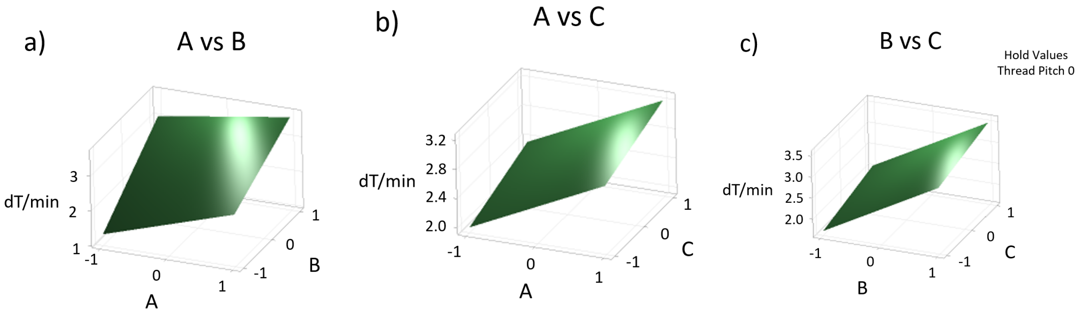

Figure 3.12: 3D surface plots for parameter relationship with change in tool temperature as the response. a) Thread Pitch vs Rotation Speed b) Thread Pitch vs Traverse Speed c) Rotation Speed vs Traverse Speed

## 3.7 Welding Forces

### 3.8 *Axial Forces*

The thread pitch does not provide a statistically significant contribution to the tool axial forces during traversing welding periods. Rather, tool rotation speed has the greatest contribution (50.06%), followed by traverse speed (21.80%), and their squared terms which combined provide a 15.61% contribution in the reduced model. The thread pitch, however, has a large contribution to the plunge force. The rotation speed once again has the greatest contribution at 56.93%, followed by thread pitch at 17.14%, and square of rotation speed at 5.16% in the reduced model. There is no significant interaction between the thread pitch and rotation speed. Traverse speed provides no contribution during the plunging period since no lateral movement occurs.

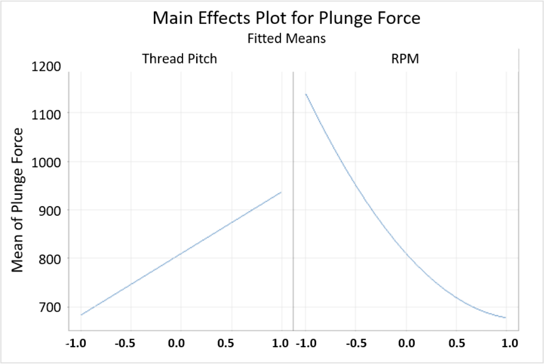

Figure 3.13: Main effects for maximum tool axial force during plunging.

Stated in section 3.6, the rotation speed and thread pitch provide the greatest contribution to tool temperature and therefore heat generation. Heat generation is inversely proportional to axial force under a constant plunge rate since heat softens the material [15]. Since rotation speed has the greatest contribution to heat generation, it is no surprise that the highest rotation speeds results in the lowest plunge forces. The thread pitch has an inverse effect on the maximum plunge force than the heat generated, where a lower thread pitch actually results in a higher maximum plunge force, shown in figure 3.13. The maximum plunge force occurs during initial contact between the tool and the material. The tool axial force slowly reduces throughout the plunge as the material softens [15]. Thus, vertical side tool geometry provides no contribution to the plunge force at initial contact, which means that the thread pitch's contribution to the plunge force is a result of its effect on the tool's bottom surface. Most notably, the surface area decreases for finer threads, and the center of the flat region becomes more offset from the tool's center axis, shown in figure 3.14. A 10% reduction in surface area occurs between the highest and lowest thread pitch tools used in this study. The bottom tool surface areas for coarse to fine thread pins are 24.5 $mm^2$, 25.16 $mm^2$, and 27.19 $mm^2$ respectively. The bottom surface offset carves and expels material through pulsation, and the small surface area inherently requires a smaller force to plunge. For runs 1-10, the coarse threads on average have a 25% reduction in plunge force over the fine threads. Because the greatest forces during FSW occur during the plunge, smaller machine requirements are necessary for coarser thread tools.

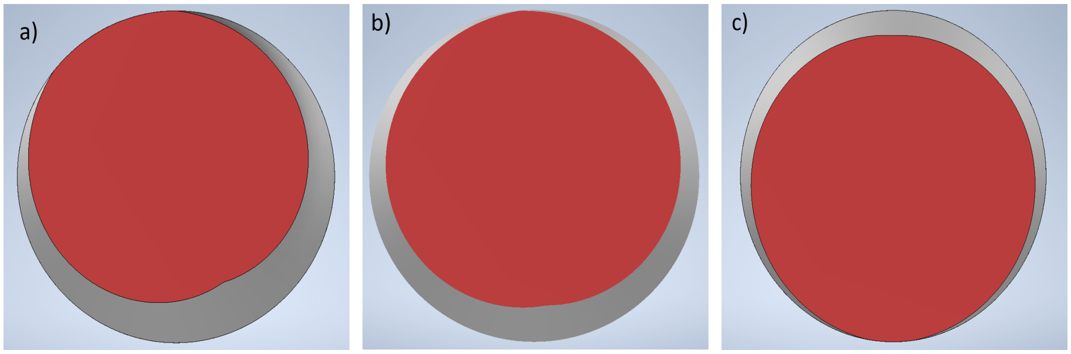

Figure 3.14: Bottom view of tool pins. The shaded region is the bottom surface area at initial plunge contact. a) 20 TPI (24.51 $mm^2$) b) 32 TPI (25.15 $mm^2$) c) 44 TPI (27.10 $mm^2$)

### 3.9 *Planar Forces*

The measured planar forces did not produce any meaningful models for parameter influence solely in the traverse or lateral directions. However, the lateral axis consistently experienced considerably higher tool forces towards the advancing side relative to the traverse axis. Planar force measurement failed during Run 11, as indicated by '*' in table 3.3. Since no correlation was present in the planar forces without Run 11, no further replicates were performed to include it in the data. The traverse forces $F_t$ ranged from approximately 3 $N$- 120 $N$, where the lateral forces $F_l$ ranged from 17 $N$- 170 $N$. The planar forces, where $F_p = \sqrt{(F_T^2 + F_L^2)}$, show a general relationship with the greatest contribution from traverse and rotation speed. Slow traverse speeds and high rotation speeds tend to reduce overall planar forces. Though these trends are apparent, the lack of fit for all produced models is well beyond the threshold of statistical significance. Lack of fit for planar forces is likely due to the implementation of the stationary shoe, whose sliding friction and interaction with the polymer melt has overwhelming effects over the tool parameters. In studies by Mendes et al. [103] and Eslami et al. [104], a contrary relationship was found where the traverse forces were significantly higher than the lateral forces. The axial forces were also significantly higher than those reported in this study. The difference in forces between the two studies lies in stationary shoe's degrees of freedom. In the current study, the shoe is allowed to slide along the vertical tool axis independent of the tool, where the shoe in Mendes et al. is fixed to the axis. Thus, the shoe has a greater axial force in Mendes et al., contributing to higher frictional forces in the traverse direction. Since the shoe's smaller axial pressure in this study allows it more freedom to float across the polymer, a higher net lateral force can be observed.

## 3.10 Discussion

Thread pitch clearly has noticeable effects on the ultimate tensile strength, heat generated, and contact plunge force during FSW of HDPE. Understanding the effects on machine forces is necessary for reliable tooling setup during manufacturing. The thread pitch has noticeable effects on the axial forces, but the required forces are related to the tool's bottom contact area and the degree to which it carves away the base material. The coarse threads have a larger "cutting area" at the tool's bottom leading edge, allowing it to perform with lower plunge forces. With a stationary shoe setup necessary to FSW many polymers, strong correlations are not observed with the parameters studied, and it is likely that the thread pitch has negligible effects. The tool temperature data produced a much better fitting model than the tensile data. This model shows that the heat generated is clearly more predictable than joint strength due to several reasons. The linear relationship between all main effects inherently makes for a simpler model to fit. Heat generation is a lower level effect than joint strength since joint strength is dependent on heat generation in FSW. The joint strength, therefore, has more variables to consider, such as the stationary shoe temperature and contact pressure. It is also clear that an improved model to predict weld strength will require a wider range in rotation speed. Generally, a hotter melt allows a polymer to flow more easily so that molecules can diffuse across a joint and bond to other molecules [95]. Interestingly, the higher tool temperatures in this study do not necessarily correlate to higher weld strength. Figure 3.15 shows a comparison between the maximum tensile strength and tool temperature for all 20 runs, and does not show a relationship between the two.

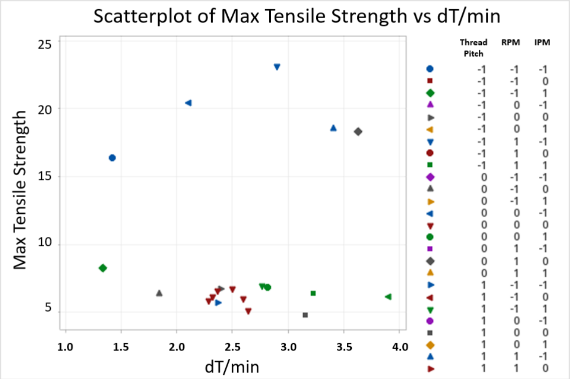

Figure 3.15: Maximum tensile strength compared to tool temperature for all 20 runs.

The tool temperature does not adequately predict tensile strength for FSW polymers due to the low polymer thermal conductivity. Mentioned in section 3.6, the surface interaction between the tool and polymer dominates the heat generation over material layer shear, so most heat is generated at the tool's surface. The tool, made of tool steel, has a significantly higher thermal conductivity than the HDPE, permitting more heat flow to the tool than into the polymer. This contradicts results found by Chao et. al, but they welded AA

2195-T8 which has an estimated 3× the thermal conductivity over their tools [100], whereas the tools used in this study have an estimated thermal conductivity of 50× that of the HPDE. Therefore, changing the parameters will not drastically alter the heat flux through the polymer, keeping the melt local to the tool. Another property difference between aluminum and polymers is the change in thermal conductivity with temperature. Aluminum, like many metals, has a maximum thermal conductivity on a downward curve [105], and this maximum occurs within temperatures experienced during FSW. Polymers have an anisotropic thermal conductivity because the heat transport favors the chain alignment direction. Semi-crystalline polymers such as HDPE tend to have higher thermal conductivity than amorphous polymers because there are more orderly packed chains to quickly transfer molecule vibrations [106]. As the polymer heats up, the spacing between the adjacent polymer chains increase, and order reduces through rotation in the chains, overall decreasing the thermal conductivity with increase in temperature and further slowing the spread of heat.

Though the finer threads have greater total heat generation due to more friction from a higher surface area, the coarse threads have greater volumetric heat generation from more severe plastic deformation [61]. Thus, it appears that the total heat generation alone is not the main contributing factor to friction stir welded polymer weld strength.

Chain entanglement at a polymer interface is the most important factor for polymer-polymer adhesion. The polymer adhesion is proportional to the fourth root of the annealing time under contact [86]. The slow tool traverse speeds during FSW caters to this critical annealing time for full inter-diffusion. The pressure experienced by polymers around the tool is also non-uniform. According to AghajaniDerazkola et. al, polymers experience a low pressure zone immediately following the traversing tool pin for a smooth tapered tool [66]. This low pressure zone prevents full polymer adhesion if applied to the adjoining surfaces too early. The asymmetry in pressure around the tool is a result of higher strain rates at the leading edge and advancing side of the tool, where higher strain rates induce higher pressures [66]. Thus, coarser threads and slower traverse speeds may increase pressure at the tool's trailing edge and limit tension pulling on solidifying polymer at the stir zone walls. The slow traverse speeds also maintain a molten weld pool behind the tool, similar to a metal fusion welding process. Strong polymer joints rely on this weld pool to heat the polymer beyond the stir zone interface. The longer the molten weld pool has contact with the stir zone interface, the more interdiffusion occurs. The enhanced polymer interdiffusion is analogous to metal FSW where slow traverse speeds facilitate greater inter-material mixing [107]. The reptation model described by Cowie states that polymers in contact will diffuse when they are above $T_g$, but this only applies for polymers in an amorphous state [6]. HDPE has a glass transition temperature, $T_g$, of $-125°C$ [40], but it returns to a semi-crystalline state as it cools, so interdiffusion will not continue after the melt solidifies. Therefore, a strong semi-crystalline polymer weld requires prolonged contact between the molten pool and base material, which is most effectively achieved by a low traverse speed.

### 3.11 Conclusion

A tool parameter study following a face centered central composite response surface design was used to determine the effects of thread pitch during friction stir welding of polymeric materials. The three tool pins had thread pitches of 1.27 *mm* (20TPI), 0.79 *mm* (32 TPI), and 0.58 *mm* (44 TPI). The studied effects of thread pitch were the ultimate tensile strength, fracture surface, tool temperature, and axial and planar forces. The study's results indicate the following:

- Thread pitch has statistically significant effects on the ultimate tensile strength, heat generation, and axial plunge force. Thread pitch does not have significant contribution to traversing axial or planar forces.
- The model for maximum tensile strength indicates both linear and quadratic contribution of thread pitch, but the strongest welds were skewed to coarser threads.
- The fine threads generate the greatest tool temperatures, but the tool temperature does not correlate to the maximum tensile strength.
- The coarser threads provide greater volumetric interaction with the polymer, improving polymer entanglement between the stir zone and base material.
- Tool threads have little effect on the welding forces. Significant thread pitch contribution to welding forces occurs only during the plunge. Coarse threads require smaller plunge forces due to less surface area on the pin bottom and increased drilling.
- The strongest weld joints are a result of prolonged contact between a molten weld pool behind the tool and base material outside the stir zone that allow for sufficient interdiffusion across the joint. Tool traverse speed provides the greatest contribution to polymer interdiffusion, as slow traverse speeds maintain a weld pool and decrease the cooling rate.

It is clear from other studies that parameter values outside the range of those performed in this study exhibit other pronounced behaviors. For example, the tool rotation speed has a greater contribution to joint strength when values range into 2000-3000 RPM. Exceedingly coarse threads may have a more pronounced milling effect on the polymer that will have a negative effect on joint strength. Further, polymer types also play a role in parameter influence based on their degree of crystallinity and molecular weight. To fully capture the influence of tool thread pitch across these wider scenarios, it will be useful to employ a uniform-precision response surface design, which will utilize more levels for each parameter that can better capture the welding behaviors across a wider range at the expense of performing more runs. The uniform-precision design will also not apply biases to the predicted responses in specific parameter regions.

# CHAPTER 4

## Joining PVC Pipe Couplings: A Portable Application for Friction Stir Welding

*Lucas T. Wilkins, Eric. L. Zhang, Alvin M. Strauss*

This work is submitted to the ASCE *Journal of Pipeline Systems Engineering and Practice*.

### Abstract

Solvent welding of PVC pipe joints can take hours to fully cure and require adequate ventilation which can postpone the use of high priority pipe systems in need of repair. An alternative PVC pipe joining method uses friction stir welding (FSW) to join PVC pipes and couplings. This study brings a novel application to FSW and determines its feasibility for jobsite PVC pipe joining through examination of processing forces, chemical changes in the welded joints, joint performance under tensile load, joint performance under hydraulic pressure, and overall processing times. Analysis of welding forces indicate relatively low machine requirements that justify the capability of small, portable FSW machines that are not possible for most current FSW applications. Thermal analysis shows that FSW poses little health risk when joining PVC pipes due to a lack of thermal degradation that would release toxic gases. Pipe joints subject to hydraulic pressure surpass ASTM burst pressure standards for all tested welding speeds. Thus, this study demonstrates welded PVC pipe coupling joints with exemplary pressure capability formed on the order of several minutes, reducing overall processing times from up to several hours that may be necessary to fully cure a solvent weld.

### 4.1 Introduction

Perhaps one of the most essential forms of infrastructure is water transport systems. In North America, over 60,000 water and waste water systems serve more than 450 million people [20]. Much of this infrastructure, manufactured from metal pipes, is crumbling due corrosion after many years of service. According to a 2002 congressional study, approximately 17% of all drinking water in the United States is lost to leaks in pipe systems, equivalent to 2.6 trillion gallons at a cost of $50.7 billion annually [20]. More than twenty years later, the problem receives little alleviation. A 2017 infrastructure report states that more recently nearly six billion gallons of treated drinking water leak from pipes per day in the United States, equating to approximately 2.1 trillion gallons per year [108]. Polymeric pipes have been increasingly implemented in water systems over the last several decades as a result of lower installation costs, reduced maintenance, and longer service life compared to metal pipes. Polymeric pipes prove useful in other applications including natural gas transport and electrical insulation. Forming reliable joints is a key challenge in pipework, especially since pipe systems must be assembled on site.

Polyvinyl chloride (PVC) is a common and favorable polymeric pipe material manufactured in a wide range of sizes from home use to large diameters used in sewer systems. Eugene Baumann discovered PVC in 1872 when vinyl chloride gas contained in a glass container turned to a white solid due to a reaction with sunlight [109]. It was not until the early 20th century that PVC saw promotion in useful applications. German scientists began developing PVC compounds in 1931, where some was designated to build pipe. World War II created a surge in PVC pipe production to restore destroyed water supply and waste water pipelines [20]. Today, PVC is the most reliable piping material. In North America, there are approximately 14 ruptures for every 160 km (100 miles) of water mains per year. For PVC, there are only 2.3 ruptures for every 160 km per year and has the lowest overall failure rate of all pipe materials [21].

Mechanical joints utilizing elastomeric seals are common in sewer and gas distribution systems. Mechanical joints offer fast assembly times, though different mechanical and chemical properties of seals from PVC can invite leaks under certain environmental conditions [110]. Though literature suggests mechanical joints are only likely to fail under extreme conditions, real world results show that mechanical joint failure exceeds that in theory. A main contributor to joint failure likely stems from installation practices [110]. Solvent welding is a common method to join PVC pipes, typically requiring a two-step application of a primer and cement applied on a PVC pipe and fitting. Solvent welding is robust method as tight tolerances between pipes and fittings provide small possibility for leaks when solvent welded. A main drawback, however, are cure times up to several hours depending on the type of cement and environmental conditions. Long processing times can be disadvantageous, especially for highly utilized pipelines. Additionally, solvent welding produces fumes that requires adequate ventilation and can cause irritation to skin, eyes, and respiratory systems [111]. If not handled properly, these qualities can induce long-term health effects.

Non-chemical welding offers an approach to join PVC pipe with improved processing times and reduced health hazards typical of solvent welding. Fusion butt welding is a common welding method for high density polyethylene (HDPE) pipe that is scalable to large diameter pipes [112]. The process utilizes a hot plate to heat the ends of butted pipes. The pipes join upon solidification when pressed together [22]. Though processing times are on the order of several minutes, quality joints require precise surface preparation to ensure adequate heat transfer and bonding. Friction welding has been studied in several forms for polymer pipe joining, which uses mechanical interactions between joining materials to heat and soften the materials. Rotary friction welding (RFW) generates frictional heat by rotating one of the joining pipe surfaces against a stationary pipe. Hamade et al. found that RFW consumed only 10% of the energy to produce a comparable joint by fusion butt welding with shorter processing times [113]. A disadvantage to this process is the requirement of workpiece angular mobility, which may not be possible for certain configurations such as angles and tee joints.

Friction stir welding (FSW) is a joining technology with rapid advancement in polymeric applications. Wayne Thomas et al. of The Welding Institute (TWI) in Cambridge, UK patented FSW as a process to join butted metal alloys on December 6, 1991 [44]. A plethora of advancements in similar and dissimilar joining commenced since then, and researchers began applying FSW to polymeric materials as early as the late 1990's [12]. The majority of polymeric FSW research focuses on joints between flat sheets of similar and dissimilar polymers and polymer composites. Poor thermal conductivity in polymers makes joining thermoplastics via FSW challenging due to poor material flow and diffusion that produces mechanically detrimental defects including porosity, kissing bonds, and root defects [9, 17]. Often, the most significant welding parameters are the tool rotation and traverse speed. Rotation speeds control heat generation, while traverse speeds dictate the amount of heat conducted through the joint thickness [68]. To combat poor heat conduction in polymers, external heat sources such as heated backing plates [67, 68], heated tools [72], and heated stationary shoulders [57, 73] implement pre-heating and slow cooling rates to improve joint performance.

Though limited, a select number of researchers applied FSW to polymeric pipe configurations. Mosavvar et al. joined butted HDPE pipes with inner supports to prevent pipe collapse and material expulsion [114]. The study reports tensile strengths of up to 5.13 MPa without external heating and a traverse speed of 110 mm/min. For reference, 25.4 mm/min traverse speeds and a heated stationary shoulder produced tensile strengths of over 23 MPa in flat HDPE sheets [115]. Recently, Jayran et al. used a bobbin tool to FSW butted PVC pipe without inner support. The bobbin tool requires pre-drilling a hole to allow tool insertion. Though they do not specify mechanical performance of the joints, Jayran et al. reports that only half of the pipe was successfully welded and the joints were brittle [85].

To the authors' knowledge, the only other study to join PVC with FSW was reported by Inaniwa et al. [116], who achieved a 45% joint efficiency in flat PVC sheets. The purpose of the following study is to expand the applications of FSW to polymeric pipe and increase the understanding of PVC FSW. Several key challenges are anticipated in this project. PVC requires processing temperatures of approximately 200°C for smooth and continuous fusion [117]. Many polymers require relatively high temperatures for effective processing. PVC is unique among most polymers in that it begins to thermally degrade at temperatures much lower than other polymers. Thermal degradation occurs in two stages for PVC. In the first stage, dehydrochlorination (de-HCl) occurs between 250°C-350°C producing volatiles such as hydrochloric acid, benzene, toluene, and other hydrocarbons. The second degradation stage decomposes the de-HCl into char between 350°C-525°C [118, 119]. Rapid thermal degradation provides a small window of processing temperatures to weld PVC without severely altering its chemical composition and releasing toxic chemicals. Thus, this study evaluates if PVC FSW risks a health hazard.

FSW typically requires large and heavy equipment due to large processing forces. FSW machine specifications limit FSW to stationary workstations in manufacturing facilities that are not suited for most pipeline joining applications. The liquid state nature of polymeric FSW requires significantly reduced processing forces, and therefore machine requirements, that are common to metal FSW. The difference in processing forces for polymer FSW [70, 104] and metal FSW [120] can reach orders of magnitude. Demonstrating low machine requirements may justify development of a portable device that can join PVC pipe on job sites. To demonstrate FSW's feasibility as a competitive joining method to current solvent welding techniques, FSW must form strong and reliable joints, produce little health hazard, utilize low processing forces, and to have the best opportunity for adoption in industry, meet these criteria while joining current off-the-shelf materials with fast processing times.

## 4.2 Materials and Methods

### 4.2.1 Joint Fabrication

All experimentation used 1.5" (38.1 mm diameter) schedule 40 PVC pipe manufactured by Charlotte Pipe and Foundry Company. Popularity and availability at common home improvement stores justified material choice. Pipe sections were cut to 63.5 mm (2.5") in length. Pipe couplings slid onto the pipes at maximum depth.

FSW was performed on a modified computer controlled milling machine. A rotary axis mounted to the machine's table made FSW on curved surfaces possible, shown in figure 4.1. FSW tooling consisted of a threaded probe and heated stationary shoulder. The probe had a diameter of 6.25 mm and left-hand threads of 1.27 mm pitch that facilitate downward material flow under a clockwise rotation. The stationary shoulder was fabricated in multiple pieces from 6061 aluminum with a curved contact surface to match the outer diameter of the pipe coupling. A step with the smaller pipe diameter kept the shoulder aligned. The tool pin protruded through the large diameter of the stationary shoulder to produce a lap weld between the coupling and pipe. Temperature controlled resistive heaters maintained the stationary shoulder at 100 °C. Figure 4.2 shows a diagram of the tool and shoulder.

A 2-parameter 3-level full-factorial design of experiments was used to optimize welding parameters for joint strength under tensile load. Tool rotation and circumferential (traverse) welding speeds were the variable welding parameters, as these are the most influential to joint strength in polymer FSW. Table 4.1 outlines the variable welding parameters. The welding direction oriented such that the tool's advancing side faced the load bearing direction in the pipe coupling. All welds utilized a 5.59 mm plunge depth. Minitab Statistical Software aided in determining the significance of welding parameters on select responses. Statistical significance was determined using analysis of variance (ANOVA) at a 95% confidence interval ($p \leq 0.05$).

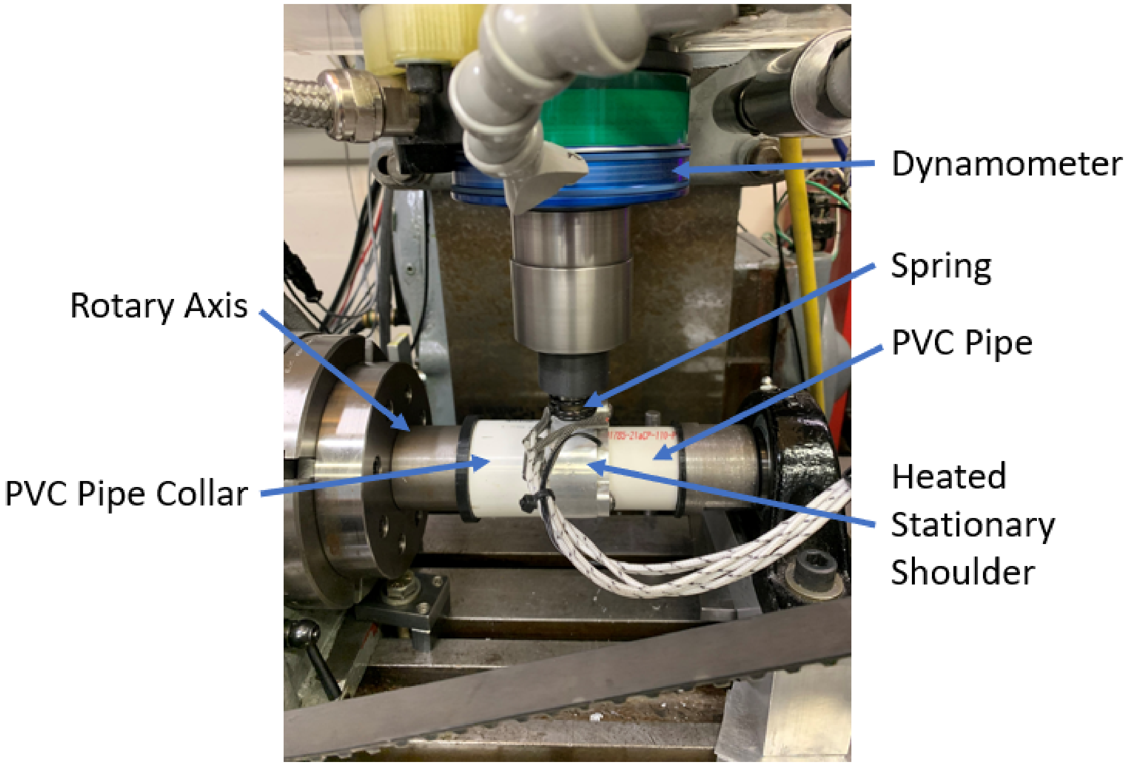

Figure 4.1: Setup for PVC pipe FSW with a rotary axis.

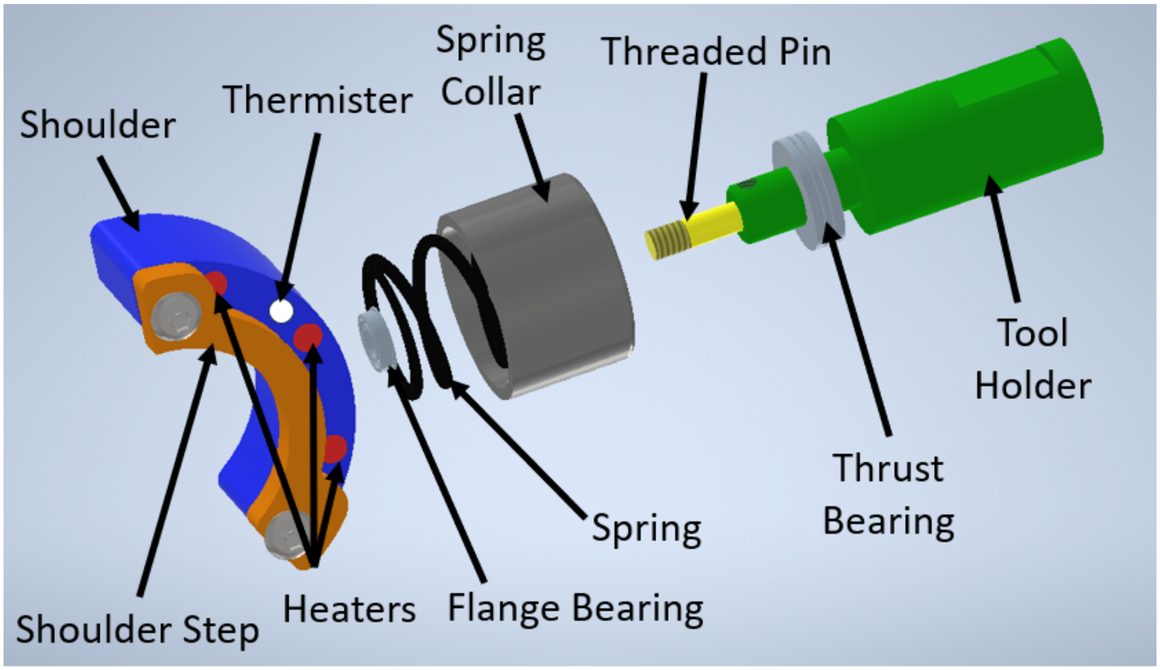

Figure 4.2: Schematic of FSW tool and curved stationary shoulder.

Table 4.1: Full Factorial Design of Experiments Parameter Setup

| Parameter | Symbol | Level 1 | Level 2 | Level 3 |
|---|---|---|---|---|
| Rotation Speed | A | 1200 RPM | 1500 RPM | 1800 RPM |
| Circumferential Speed | B | 25.4 mm/min | 44.5 mm/min | 63.5 mm/min |

### 4.2.2 Welding Forces

A Kistler type 9123C dynamometer mounted to the welder spindle provided measurement of axial forces (z-direction), circumferential forces (x-direction), lateral forces (y-direction), and spindle torque. Filters applied to the raw data removed signal noise corresponding to the tool rotation frequency. Low bandpass filters include 20 Hz, 25 Hz, and 30 Hz for 1200 RPM, 1500 RPM, and 1800 RPM rotation speeds, respectively.

### 4.2.3 Thermal Analysis

Thermogravimetric analysis (TGA) commenced in a TA Instruments SDT-Q600. Specimens from weld zones were cut to approximately 7 mg in mass. Flat specimen surfaces formed with abrasive paper ensured adequate sample contact with the instrument's sample cup.

### 4.2.4 Mechanical Tests

#### 4.2.4.1 Tensile Tests

Tensile specimens were cut from three locations in each weld parameter condition. Location 1 refers radially to 13° after the weld keyhole, location 2 refers to 180° from the weld keyhole, and location 3 refers to 13° prior to the weld keyhole. The keyhole is an open cavity of displaced material left in the weld piece when the tool retracts. Figure 5.3.7 illustrates the location of tensile specimens.

A universal load frame pulled specimens at a rate of 5 mm/min. Pads between the specimens and instrument's grippers compensated for the lapped pipe section offset. Tensile specimens of cemented joints were also pulled.

#### 4.2.4.2 Pressure Tests

An additional set of welded pipe sections were prepared for hydraulic pressure testing with the pipe section cut to 76.2 mm (3 in.) in length. Pipe caps cemented to the welded pipe sections formed a pressure chamber. The caps were fastened using an Oatey Handy Pack, consisting of Purple Primer and Medium Clear PVC Cement. The cement cured for 24 hours prior to testing. Male pipe caps cemented to the welded collar were drilled and tapped on their ends to accommodate a 3/8" NPT fitting for a hydraulic line quick disconnect. A 2000 psi gauge was threaded into the opposing female cap side wall that was cemented to the welded pipe section. The pressure vessels were filled with canola oil. An Enerpac P-84 10,000 psi hydraulic pump

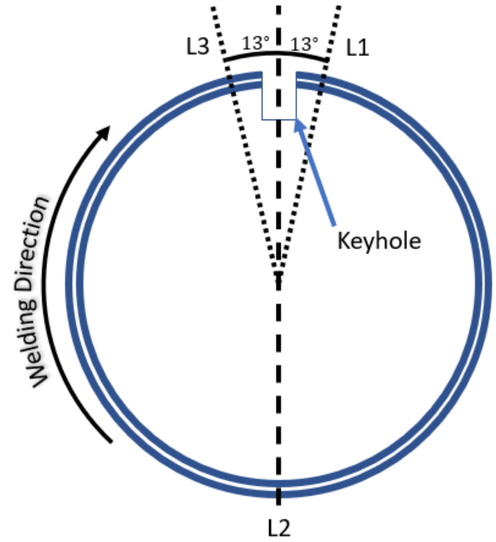

Figure 4.3: Locations of tensile shear specimens with respect to the weld keyhole.

supplied hydraulic pressure. Pressure vessels were submerged in water at temperatures between 25°C to 29°C during testing. High speed cameras recorded the pressure gauges during testing. The pressure was increased gradually until failure at approximately 7 MPa/min such that bursts occured after 60 seconds according to ASTM D1599-18 [121].

## 4.3 Results

### 4.3.1 Welding Forces

Welding parameters have a significant effect on processing forces under certain circumstances. Table 4.2 briefly summarizes the parameters that affect each force component and lists the average value of each force component throughout the entire study. **A** refers to rotation speed, **B** refers to circumferential welding speed (WS), and **AB** refers to the interaction between the two. All forces were calculated using the average during the duration of weld traverse, with the exception of the axial plunge force. The axial plunge force reports the maximum during initial plunge. Sections 4.3.1.1,4.3.1.2,4.3.1.3, and 4.3.1.4 provide an in-depth analysis on parameter influence on each force component. The welding force directions can be referenced in figure 4.4.

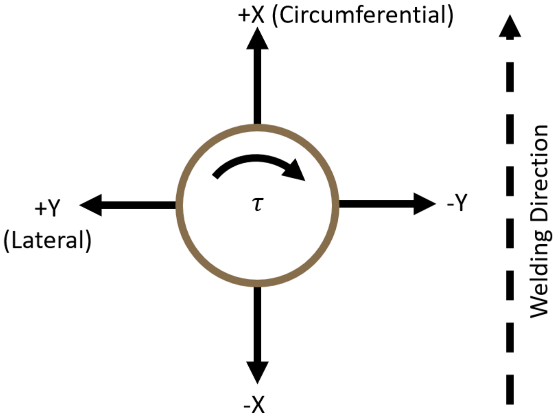

Figure 4.4: Diagram of force directions with respect to the tool.

Table 4.2: Summary of Welding Forces

| **Force Direction** | **Significant Parameter Contribution** | **Significant Parameters** | **All Average Force** |
|---|---|---|---|
| **Circumferential** | ✓ | **B AB** | 1.5 N |
| **Lateral** | ✓ | **B** | 65.3 N |
| **Axial (Average)** | × | n/a | 232.3 N |
| **Axial (Plunge)** | × | n/a | 178.8 N |
| **Torque** | × | n/a | 0.2 Nm |

#### 4.3.1.1 Circumferential Forces

The circumferential force, or traverse force, dictates machine requirements to push the tool around the pipe joint. Figure 4.5a shows a linear trend for both parameters **A** and **B**. The average force changes direction at larger tool rotation speeds and circumferential speeds. At low rotation speeds, the force applied at the tool's leading edge and friction from the stationary shoulder dominate and pull the tool away from the welding direction. During FSW, the rotating tool sweeps the polymer around the retreating side (RS) to the back of the tool and forces material back into the advancing side (AS). Thus, the higher material velocity as the material transports behind the tool pushes the tool towards the welding direction at higher RPM's. Figure 4.5b shows an interaction effect between parameters **A** and **B**, indicated by the crossing weld speed lines. In essence, the welding speed contributes to the tool rotation speed's effect on circumferential welding forces because it controls the rate of material that the tool can pull around itself.

ANOVA results shows that **AB** and **B** are statistically significant results in a regression model, shown in

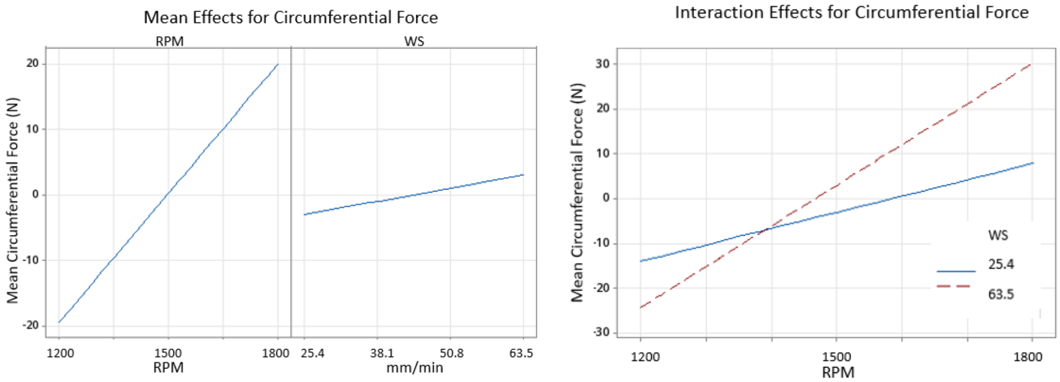

Figure 4.5: a) Mean parameter effects on circumferential force. b) Circumferential force parameter interaction.

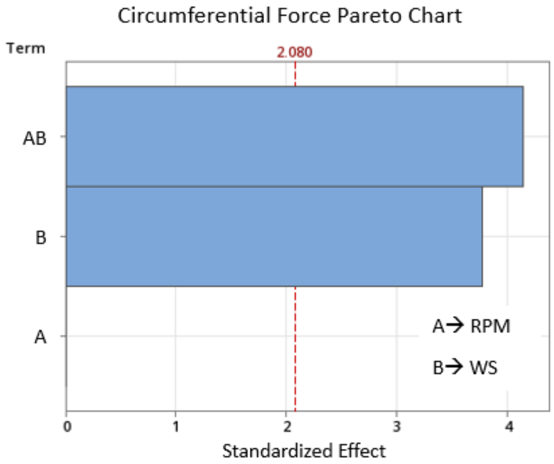

Figure 4.6: Pareto chart for parameter effects on circumferential forces. The red dotted line is the threshold for statistical significance.

figure 4.6. A model with parameters **A** (p = 0.999), **B** (p = 0.001), and **AB** (p = 0.000) provides the best overall fit with a coefficient of variance $R^2 = 88.43\%$, $R^2_{adj.} = 86.77\%$, and $R^2_{pred.} = 82.55\%$. Though **A** on its own does not have statistically significant effects on circumferential forces, it does have the greatest % contribution due to the wide range in mean effects. Hence, this contribution and its hierarchy make it essential to include in the model, though its contribution only has statistical significance when considering its interaction with **B**.

#### 4.3.1.2 Lateral Forces

The lateral force describes cross-weld forces on the tool that dictates workpiece fixture requirements to keep the tool aligned on the welding path. The average magnitude of lateral forces exceed those of the circumferential forces by considerable margin. However, sweeping the welding parameter values does not change

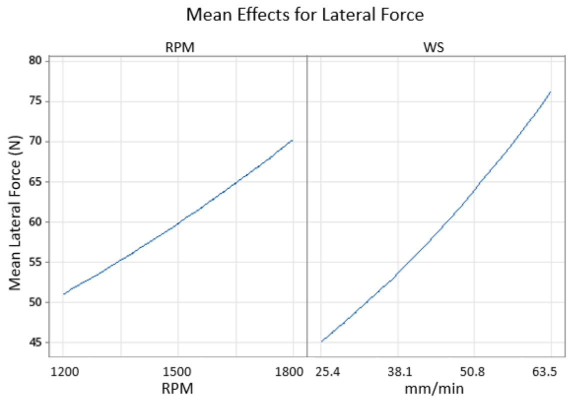

Figure 4.7: Mean parameter effects for lateral force.

the lateral force direction. Figure 4.7 shows a general linear contribution between parameters **A** and **B** and lateral forces. Positive lateral forces indicate that the tool pulls towards the advancing side (AS). Though the heated stationary shoulder preheats the polymer in front of the tool, friction with the rotating tool contributes to the bulk of material softening and melting. The softened polymer then transfers to the back side of the tool. Thus, material in front of the tool has greater viscosity than material behind the tool, pulling the tool towards the AS. Passing the polymer between the tool and retreating side (RS) also contributes to the tool forces towards the AS. In the case of this experiment, the tool's clockwise rotation pulls the tool left of the weld line.

A model with parameters **A** and **B** provides the best fit, though **B** is the only statistically significant term (figure 4.8). No significant parameter interaction between **A** and **B** occurs for lateral force. A model for parameter contribution to lateral force including **A** (p = 0.077) and **B** (p = 0.009) results in a coefficient of variance $R^2 = 34.80\%$, $R^2_{adj.} = 28.88\%$, and $R^2_{pred.} = 12.11\%$. The lateral force model has poor regression compared to the circumferential force. A key difference between the two directions is that the step design of the stationary shoulder counteracts forces towards the AS. Any lateral tool deflection can only occur from compliance between the tool, stationary shoulder, and work piece. The stepped shoulder limits this compliance towards the AS.

#### 4.3.1.3 Axial Forces

The axial forces dictate the downward pressure the tool spindle must apply to the workpiece. During the weld traverse period, increasing parameter **A** tends to increase the average axial force while increasing parameter **B** tends to decrease the average axial force. However, neither parameter provides statistically significant contribution. FSW typically experiences the greatest axial forces during the plunge at the beginning of the weld since the tool must soften and displace material using the bottom tool face. The tool rotation speed

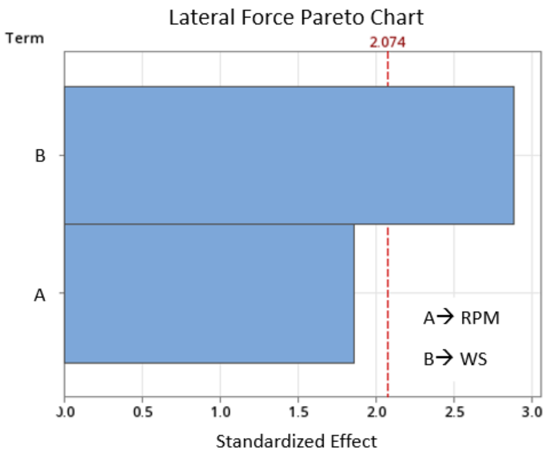

Figure 4.8: Pareto chart for parameter effects on lateral force. The red dotted line is the threshold for statistical significance.

usually affects the axial plunge force due to its effect on heat generation. However, parameter **A** does not influence the plunge force, and the axial force during the traverse period tends to surpass the plunge force. This phenomena may be caused by preheating from the stationary shoulder during weld setup that softens the polymer at the weld start.

#### 4.3.1.4 Torque

Spindle torque is opposition to the welding material's resistance to tool rotation and dictates the required power. PVC provides very little resistance to tool rotation with an average torque of 0.21 Nm during the weld traverse period. The welding parameters do not have statistically significant effects on spindle torque, though the small torque measurements are within the sensitivity of the dynamometer. Nonetheless, the liquid state nature of polymer FSW reduces torques compared to solid state welding of metals. The lack of a rotating shoulder also significantly reduces the overall torque. Adding a rotating shoulder can increase the spindle torque by an order of magnitude, which would likely show more contribution from welding parameters [64].

### 4.3.2 Thermal Properties

Thermogravimetric analysis (TGA) can indicate thermal degradation through changes in weight measurements as the material subjects to increasing temperatures. Figure 4.9 shows TGA curves from locations 1,2, and 3 within the same pipe weld fabricated with 1500 RPM, 25.4 mm/min welding parameters. Locations 1 and 3 experience greater heating than location 2 due to their close proximity to the beginning and end of the weld. Tool dwelling at the weld start and finish in conjunction with prolonged contact of the heated stationary shoulder during these periods contribute to a bias in heat input on this side of the pipe weld. The weld loca-

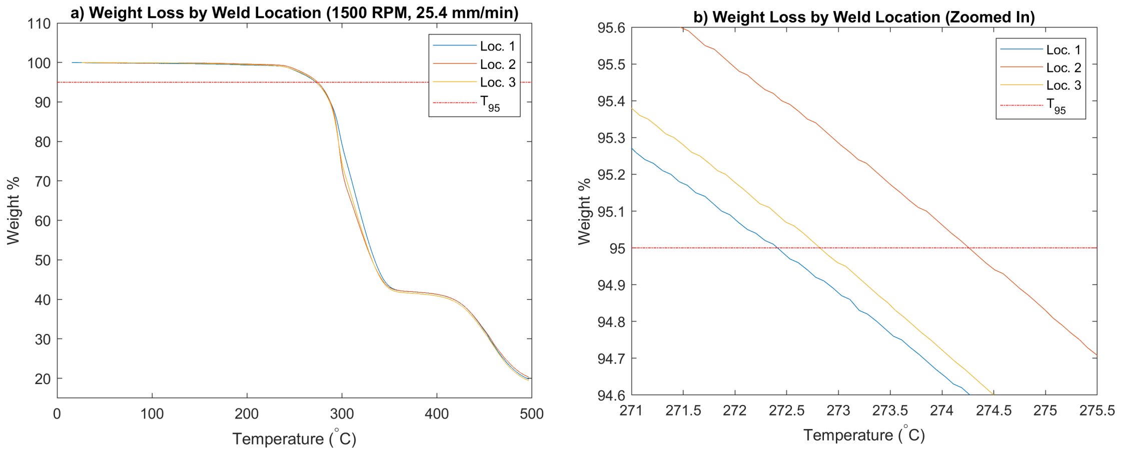

Figure 4.9: TGA comparison between weld locations. a) Full curve. b) Zoomed in comparison at $T_{95}$ for each weld location.

tion produces nearly identical TGA curves between locations along the weld. Each location has very similar $T_{95}$ values, which is the temperature with a 5% mass loss. Location 2 has a slightly larger $T_{95}$ than locations 1 and 3, though the difference is less than 1% and within the instrument's range of precision.

Several 1800 RPM welds exhibit discolouration near location 1, shown in figure 4.10. The discolouration goes through the thickness of the stir zone, though the discolouration ceases further from the weld keyhole. Discolouration of polymers during FSW typically indicates thermal degradation and burning [9]. The high tool rotation speeds in 1800 RPM welds contribute to greater tool heat input and have the potential to degrade the polymer. Figure 4.11 plots TGA curves of browned weld regions in 1800 RPM, 25.4 mm/min welds and compares them to virgin PVC couplings. Each 1800 RPM specimen was clipped from the same weld, with the third specimen closest to the weld keyhole. $T_{95}$ values decrease closer to the keyhole and indicate reduced thermal stability caused by higher degrees of thermal degradation. The gradient of thermally degraded material is sharp, however, as these specimens were clipped from the weld within a range of 5 mm. Thus, it appears that slight adjustments to the dwell time at the beginning and end of the weld can easily reduce onset of thermal degradation. The discolouration also does not present itself in all 1800 RPM welds. Inconsistency of discolouration between replicates and the relatively small degradation zone suggests that these welding parameters produce temperatures at the borderline of thermal degradation. Table 4.3 summarizes the values from all TGA runs, and demonstrates that with the exception of 1800 B2 and 1800 B3, FSW has little impact on PVC's thermal stability. Thus, mitigating prolonged heating of the polymer in the stir zone ensures that FSW does not thermally degrade PVC. Maintaining the chemical composition of PVC in FSW joints not only ensures retained joint performance, but also ensures that it is a safe joining process without releasing toxic gases.

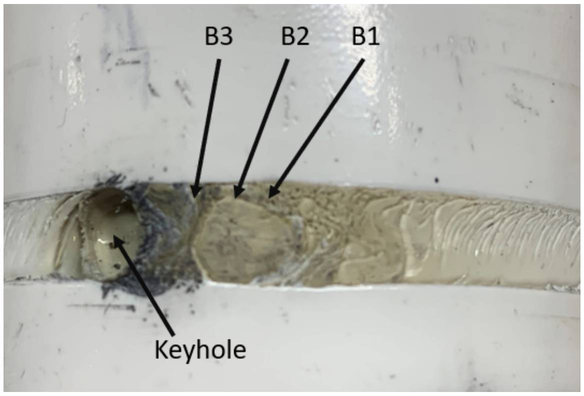

Figure 4.10: Discolouration due to excessive heat input.

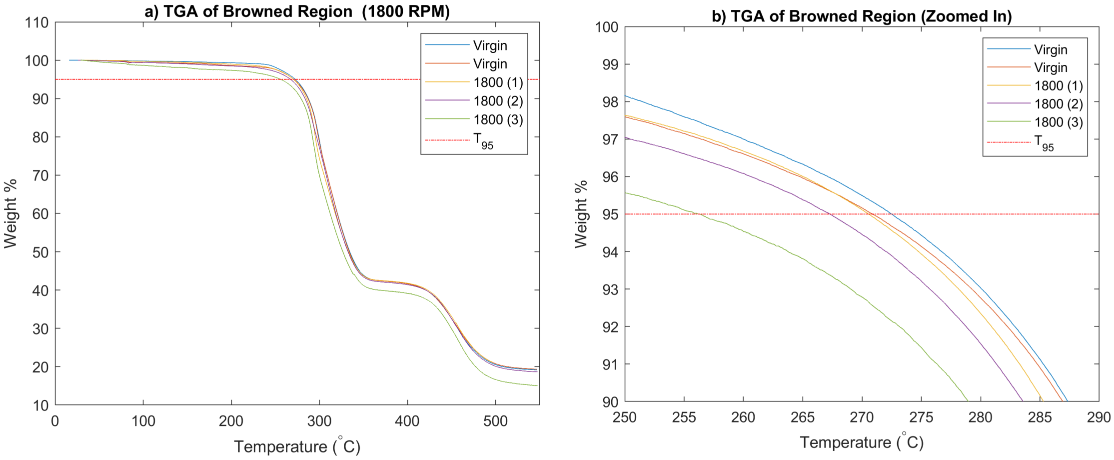

Figure 4.11: TGA for discoloured weld regions. a) Full curve. b) Zoomed in comparison at $T_{95}$.

Table 4.3: Summary of TGA results.

| **Specimen** | $T_{95}$ (°C) |
|---|---|
| Virgin 1 | 272.5 |
| Virgin 2 | 270.9 |
| 1500 loc. 1 | 272.4 |
| 1500 loc. 2 | 274.3 |
| 1500 loc. 3 | 272.8 |
| 1800 B1 | 270.6 |
| 1800 B2 | 267.3 |
| 1800 B3 | 256.2 |

### 4.3.3 Mechanical Properties

#### 4.3.3.1 Tensile Tests

The motivation of tensile tests was to identify not only welding parameter effects on joint strength, but also weld location discrepancies due to uneven exposure to the heated stationary shoulder based on the circumferential distance from the weld start and finish. The circumferential locations tested along the weld line with respect to the weld initiation and completion do not have significant contribution to ultimate tensile strength (UTS), which suggests that the location of weld failure under pressure may not be predictable. A possibility for homogeneous joint strength around the weld circumference may be a result of the stationary shoulder's design. Since the stationary shoulder contacts the welded joint 47 mm beyond the tool pin, prolonged annealing has marginal gains according to the diffusion/annealing relationship, where polymer diffusion is proportional to the fourth root of annealing time under contact [122]. Lack of weld line location dependency on joint strength also agrees with indifferent TGA results between joint locations in section 4.3.2.

Table 4.4 reports the average UTS for each combination of parameters **A** (tool rotation speed) and **B** (circumferential welding speed). The maximum average recorded UTS occurs with 1800 RPM tool rotation speeds and 25.4 mm/min circumferential welding speeds. The average solvent welded joint had a 0.145 kN/mm UTS, meaning the FSW joints have up to 56% the UTS of a solvent welded joint. The solvent joint under tensile load has an advantage over the FSW joint due to the larger surface area under shear. The fracture mechanics between solvent welded joints and FSW joints in lap configuration under tensile load also differ. The solvent welded joint experiences failure through peeling due to torques from lapped offset. The welded joints fail at the interface between the weld zone and base material.

Table 4.4: Average UTS values for tool rotation (**A**) and circumferential (**B**) speeds.

| A (RPM) | B (mm/min) | UTS (kN/mm) | $\sigma$ (kN/mm) |
|---|---|---|---|
| 1200 | 25.4 | 0.075 | 0.012 |
| 1200 | 44.5 | 0.054 | 0.011 |
| 1200 | 63.5 | 0.032 | 0.016 |
| 1500 | 25.4 | 0.073 | 0.023 |
| 1500 | 44.5 | 0.063 | 0.011 |
| 1500 | 63.5 | 0.043 | 0.015 |
| 1800 | 25.4 | 0.081 | 0.013 |
| 1800 | 44.5 | 0.079 | 0.011 |
| 1800 | 63.5 | 0.067 | 0.011 |

Rotation speed and circumferential speed have both linear and interactive effects on UTS, shown in figure 4.12. Generally, faster rotation speeds and lower traverse speeds facilitate the greatest joint strengths in polymer FSW due to low thermal conductivity. The rotation speed contributes to heat generation while the traverse speed contributes to the immediate post-weld annealing time. Since polymer adhesion across a joint is proportional to the fourth root of annealing time under contact [122], slow traverse speeds play a critical role in enhancing polymer interdiffusion. Additionally, polymer FSW creates a low pressure zone along the RS behind the tool, and fast traverse speeds can pull the polymer in the weld zone from the RS wall before it has time to adhere [123]. Figure 4.12b shows the importance of slow traverse speeds on joint strength through parameter interactions. The rotation speed has less influence on UTS at the slow traverse speed, indicated by a shallow slope on the plot.

Figure 4.13 shows statistically significant contribution to UTS from parameters **B** (p= 0.000) and **AB** (p = 0.004). **A** does not have statistically significant contribution alone (p = 0.300) due to the large interaction influence mentioned previously. A regression model containing the presented terms has a coefficient of variance of $R^2 = 55.30\%$, $R^2_{adj.} = 53.27\%$, and $R^2_{pred} = 49.81\%$. Poor regression may be a product of the strength test nature, as offset in the lapped tensile specimens add to the complexity of joint fracture.

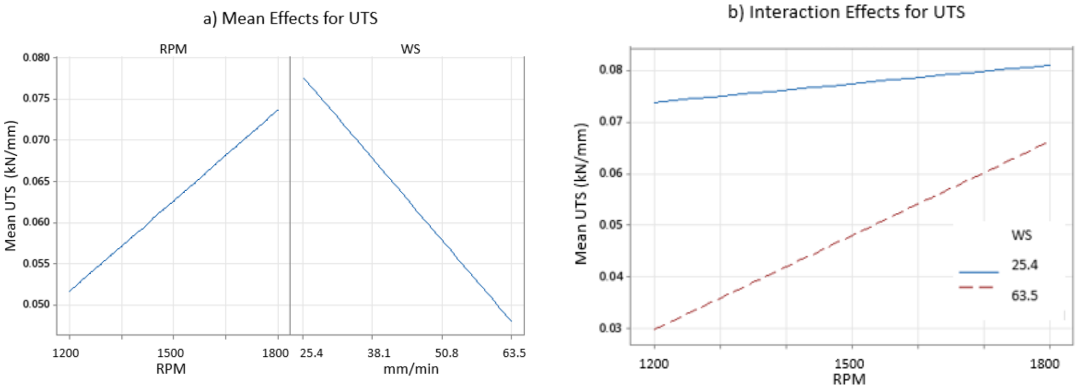

Figure 4.12: a) Mean parameter effects on ultimate tensile strength. b) Tensile strength parameter interaction.

#### 4.3.3.2 Pressure Tests

Hydraulic pressure tests provide improved insight to welded pipe joint performance under real-world applications. All pressure tested joints were fabricated using 1800 RPM tool rotation speed since the UTS results and model suggest that the highest tested rotation speed provides the best joint performance. Generally low machine requirements across all welding parameters means that a portable FSW device can easily be designed to operate under a wide range of tool rotation speeds. Circumferential speed contributes to the overall joint processing time and therefore FSW's practicality as an alternative joining method to current PVC cement

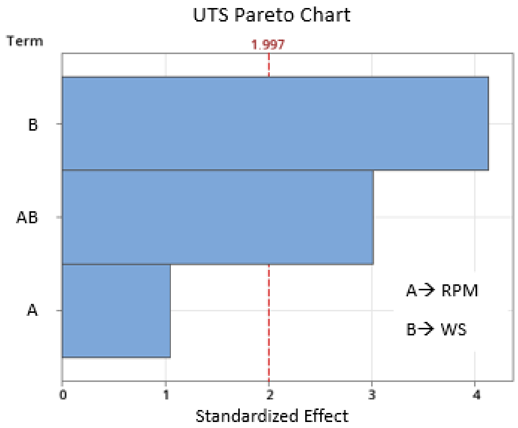

Figure 4.13: Pareto chart for parameter effects on ultimate tensile strength. The red dotted line is the threshold for statistical significance.

techniques. Though the UTS model shows improved strength from the 25.4 mm/min circumferential welding speed, 50.8 mm/min and 63.5 mm/min welds were subjected to pressure tests to analyze their performance, as reducing the overall processing time makes FSW more attractive.

Pressure tests for 25.4 mm/min, 50.8 mm/min, and 63.5 mm/min circumferential speeds will be referred to as C1, C2, and C3 respectively. The lowest pressure failure occurred in specimen C1-1 with a burst pressure of approximately 3.6 MPa (525 psi), shown in figure 4.14. In this specimen, a crack initiates along the weld zone AS in the pipe coupling. The location of initiation occurs 39 mm prior to the weld keyhole. The crack propagates as the coupling bursts and releases fluid. The highest recorded burst pressure was in specimen C3-1 at approximately 8.44 MPa(1225 psi). The weld in C3-1 failed uniformly around the weld, shown in figure 4.15. The initial weld failure in C3-1 occurs 20 mm following the keyhole. The weld keyhole was hypothesized to initiate joint failure due to the cavity in the joint line. Failure locations in C1-1 and C3-1 do not agree with this hypothesis. Prolonged tool contact at the keyhole during the dwelling period may promote further polymer diffusion that has greater resistance to splitting of the virgin coupling material and weld line.

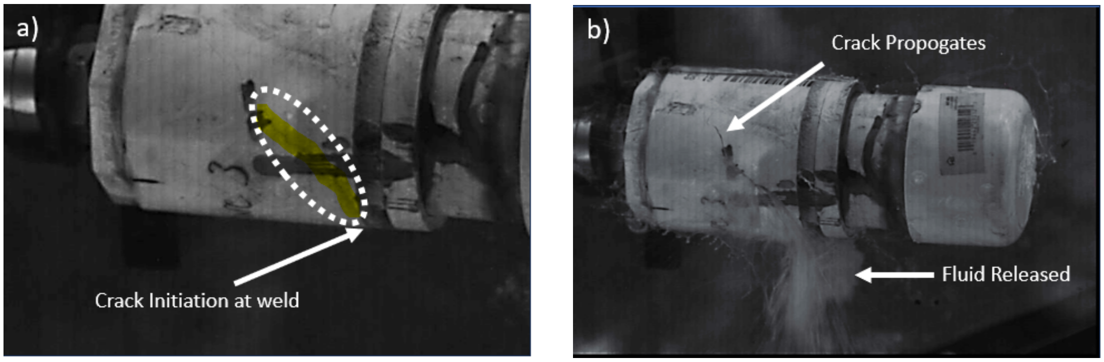

Figure 4.14: Weld failure under pressure. a) Crack initiates at weld zone. b) Crack propagates through pipe coupling and releases fluid.

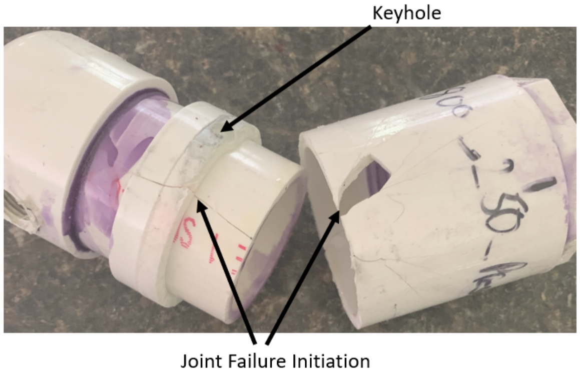

Figure 4.15: Fractured C3 pipe weld after a burst pressure of 8.44 MPa (1225 psi).

Comparing the weld surface morphology of specimens C1-1 and C3-1 reveals that a localized defect in C1-1 served as a crack initiator, allowing for the pipe coupling to split. Meanwhile, C3-1 has a consistently consolidated surface. Figure 4.16 shows the weld surface in specimens C1-1 (figure 4.16a) and C3-1 (figure 4.16b). C1-1 displays pulling of the polymer away from the RS during the welding process. This defect does not contribute to the poor joint performance, as the RS provides no load bearing support in this joint configuration. Small polymer agglomerations throughout the weld surface suggest poor consolidation of the polymer in the weld pool and possibly reduced processing temperatures than optimal. A faint line along the AS indicates sub-par adhesion and polymer interdiffusion between the weld zone and pipe collar. C3-1 does not display these defects. No channel lies along the RS. The center of the weld zone is fully consolidated and the AS shows substantially improved interdiffusion between the weld zone and pipe coupling.

Poor material consolidation in specimen C1-1 does not agree with tensile results of other joints formed using the same welding parameters with the 25.4 mm/min circumferential welding speed. However, further investigation shows that C1-1 lacks consistency in the total joint thickness measured from the weld surface to the interior pipe. Characteristic bulging of the polymer below the weld zone occurs due to lack of inner

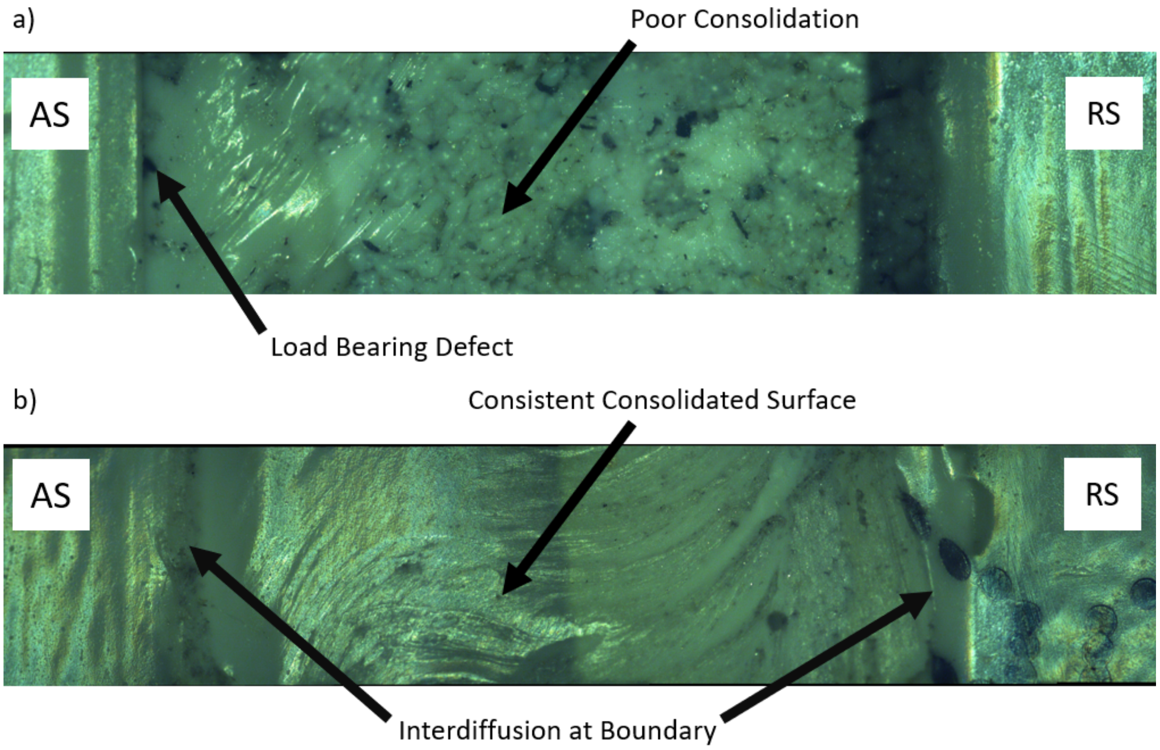

Figure 4.16: Comparison of C1-1 (a) and C3-1 (b) weld surfaces. a) reveals a defect that initiated weld failure. b) has a consistent weld morphology around the pipe circumference.

support during the FSW process, shown in figure 4.17. In C1-1's fracture location, the average thickness from weld surface to the bottom of the weld bulge measures 9.360 mm while the average thickness around the rest of the joint circumference measures 8.801 mm. Similarly, the average joint thickness around C3-1 measures 8.778 mm. The additional thickness in the failure region of C1-1 reduces polymer contact with the stationary shoulder and pressure in the weld zone that forces the softened material to fully consolidate. It is likely that the 1800 RPM, 25.4 mm/min welding parameters used in C1-1 lie on the border of oversoftening material and may result in inconsistent joints. Thus, surface defects such as those in figure 4.16a are indicative of a joint weakness under pressure and non-destructive visual inspection may be sufficient for in-the-field quality control. Figure 4.17 also shows faint red polymer in the weld zone throughout the entire weld thickness. The red colour change results from printed numbers stamped on the surface of the inner pipe by the manufacturer. The uniform red colour in this weld region indicates sufficient material flow and mixing between the pipe coupling and inner pipe.

Of the 9 specimens subjected to pressure tests, only C1-1 and C3-1 failed at the weld zone. All other specimens failed by release of the PVC cement at the end caps with an average burst pressure of 7.34 MPa (1065 psi). According to ASTM D2466-21, the required burst pressure for water at 23°C is 7.31 MPa (1060

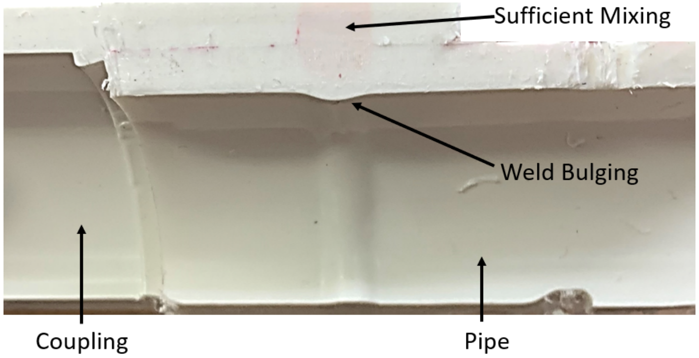

Figure 4.17: Bulging in inner pipe caused from material softening below the weld zone.

psi) for a 38.1 mm (1.5") nominal size PVC pipe [124]. Therefore, the quality of joints in the cemented pressure vessels meets the standards of ASTM D2466-21. Though these tests do not confirm the true failure burst pressures of the FSW joints, these experiments confirm that the FSW joints between the PVC pipe and PVC coupling meets or exceeds ASTM standards for all tested circumferential welding speeds.

### 4.4 Discussion

Two disadvantages of FSW for polymeric materials include use of non-portable equipment and slow joining times. Polymers with a high melt flow viscosity can be especially challenging to adhere at the weld RS, further requiring slow welding speeds. Joining of existing PVC couplings finally offers a polymer joining application where FSW can flourish. Welded pipe coupling joints biases loads to one side of the weld, reducing the detriments of poor RS adhesion in FSW joints. FSW of PVC pipe couplings does not require inner supports due to PVC's inherent rigidity and the fact that lap welding does not require full penetration through the bottom workpiece. Coupling joints also do not necessitate flush end mating surfaces between cut pipes. Thus, FSW can easily be adapted to most existing PVC pipe coupling configurations with appropriate tooling design. FSW may not be appropriate for butted PVC pipe joints as softening in the weld zone may require inner supports, and the RS becomes load bearing in butt joint configuration. For butt joints, current fusion welding technology may still be the best option.

These experiments also suggest the possibility for portable FSW devices to join PVC pipe couplings. All reported welding forces are manageable within small fixtures. The low torque values can be easily achieved with portable cordless equipment. For example, consider the DeWalt DCD991P2 drill, a cordless drill top rated by Consumer Reports in 2023 [125]. Weighing only 2.13 kg (4.7 lb), it can output 820 W of power and run up to 2000 RPM. Considering the average torque measured during FSW of PVC pipe couplings, only approximately 40 W must be supplied to the spindle for several minutes to form each joint. Thus, existing tool manufacturers already have the technology to build portable devices with the power necessary to FSW PVC.

Finally, possibly the greatest determining factor of FSW's practicality to join PVC pipes is the overall processing time. Total welding time including tool plunge, dwell, traverse, final dwell, and retraction when using the 63.5 mm/min circumferential welding speeds takes 300 seconds. Assuming insertion of the pipe into the coupling and mounting a portable device takes 1 minute, then the total processing time to FSW a PVC pipe coupling requires 6 minutes. The joint can be put into service immediately after joint completion. Next, consider a solvent welded PVC joint using the Oatey Handypack mentioned in section *Materials and Methods*. Assume 30 seconds to apply the primer and cement. Per the instructions, the joining pieces must be held for 30 seconds to prevent the parts from disassembling. It takes 15 minutes for the joint to be set for handling, and 2 hours or more to fully cure depending on the temperature. Comparing the two methods, PVC pipe couplings joined by FSW can outperform cemented joints under pressure with significantly reduced total processing time. Unlike the solvent weld, FSW does not produce strong odors that necessitates considerable ventilation.

This work demonstrates promising results for PVC pipe coupling FSW, though plenty of other considerations may further improve the process. For example, previous experiments show that the stationary shoulder temperature affects the mechanical properties in polymer FSW [73]. Thus, varying the stationary shoulder temperature may realise improved mechanical properties or allow for faster circumferential welding speeds. The process may also benefit from testing faster welding speeds to reduce processing times, as joints formed with faster circumferential welding speeds may still provide sufficient mechanical performance. This concept can also extend to the tool plunge speed and dwell times. The location of the weld with respect to the coupling and pipe overlap may also have an influence on joint performance under pressure, as a weld along the edge of the inner pipe would prohibit fluid from squeezing between the pipe and coupling under pressure. As a final note, modeling the effect of bulging beneath the weld in the inner pipe should be considered, as the variable geometry can contribute to head loss [126].

### 4.5 Conclusion

This work expands the applications of polymeric friction stir welding (FSW) to join off-the-shelf PVC pipe couplings. The criteria for this research was to explore the feasibility of PVC pipe FSW in terms of machine requirements, health/safety, joint performance, and processing time. The following list summarizes the key findings:

- The welding setup included a rotating pin and heated curved stationary shoulder with step design that permitted joining of schedule 40 PVC pipe couplings to 1.5" (38.1 mm) diameter schedule 40 PVC pipe.

- Overall processing forces were low, indicating that portable equipment can handle the FSW process that traditionally requires larger machinery in metal FSW.
- Thermogravimetric analysis results indicate little to no chemical changes in welded specimens, suggesting that FSW can join PVC pipe couplings without health hazard.
- Tensile tests around various locations in the friction stir welded pipe joint indicates that a pipe joint has consistency and no inherent weak points.
- Welded coupling joints subjected to hydraulic pressure testing surpass ASTM burst pressure standards for all circumferential welding speeds. Burst pressures up to 8.44 MPa (1225 psi) were recorded.
- Joining a 1.5” (38.1 mm) diameter PVC pipe and coupling by FSW requires approximately 6 minutes with the 63.5 mm/min circumferential welding speed. A solvent welded joint on the other hand, can require several hours to fully cure.

# CHAPTER 5

## Forming A Conductive Large Area AA6061 HDPE Metal-Polymer Composite via Top Plate Friction Stir Processing

The following work was previously published in the *Journal of Manufacturing Processes* as:

L. Wilkins, A. Strauss, Forming A Conductive Large Area AA6061 HDPE Metal-Polymer Composite via Top Plate Friction Stir Processing. Journal of Manufacturing Processes. July 2021; 68:(34-42).

### Abstract

In this study, a new method of forming conductive large area metal/polymer composites called top plate friction stir processing was performed using a thin aluminum plate and HDPE sheet. To form the composite, a rotary tool uses friction to heat and stir lapped aluminum into HDPE. This method differs from other forms of friction stir processing polymers because the base material does not need modification prior to processing, increasing the total manufacturing efficiency. Upon processing, the top plate becomes the composite filler material in addition to controlling surface quality by containing the molten polymer and distributing heat. Optical analysis, electrical and thermal conductivity tests, and tensile tests were performed to determine the material distribution, conductivity, and mechanical properties of processed specimens. These tests revealed that top plate friction stir processing improved the electrical and thermal conductivity over the base HDPE . Electrical resistance across specimens measured just several ohms and thermal conductivity increased up to 108%, but mechanical properties have room for improvement.

### 5.1 Background

Aerospace and other industries are constantly looking for advanced lightweight and high performance materials to improve the efficiency and capability of future products. According to TA 12: Materials, Structures, Mechanical Systems, and Manufacturing of the 2015 NASA Technology Roadmaps, "NASA has an immediate need for more affordable, lightweight materials and processes across its unique missions, systems, and platforms." Many polymers possess rivaling strength capabilities to traditional aerospace materials, such as aluminum. However, their use is limited as a replacement for metals due to poor thermal, electrical, and other surface properties [127]. These limitations can be mitigated by adding fillers to polymers. Metal filled polymer composites have the potential for numerous applications including electromagnetic interference shielding [128], radiation shielding [129], lightweight structures, and components requiring wide temperature and corrosion resistance [33].

Electrical, thermal, and mechanical properties of metal filled polymer composites greatly depend on the filler's properties, particle shape, volume fraction, and distribution of particles [130, 131]. Each composite property has a percolation threshold, or minimum filler content for it to have saturated gains. Because the percolation threshold depends on several variables, predicting it and ideal filler parameters is challenging. However, a general trend is that for a given filler content, decreasing particle size on the order of nanoscales improves electrical conductivity [130], thermal conductivity [131], and mechanical properties [132] because the particles are likely to have a more homogeneous distribution. Additionally, a large particle axial ratio, or the particle's elongation, also tends to improve electrical conductivity [130]. Achieving high performing composite properties with the lowest filler content possible keeps polymer composites valuable as a lightweight alternative to metal structures.

Thermoplastic composites can be prepared in several ways including melt mixing [128], injection molding [33], mechanical milling [133], and friction stir processing (FSP) [95, 127, 134, 135]. FSP is a simple, efficient variant of TWI's 1991 development of friction stir welding (FSW), traditionally used to form composites and refine grain structures in metals [136]. It is advantageous over other composite forming methods due to its simplicity and ability to modify existing components [127]. FSP polymers has challenges compared to metals due to different thermo-mechanical properties that induce defects when using traditional FSP methods [95, 133]. Though extensive study has been explored regarding FSW of polymers, significantly less publications are available for FSP of polymers.

Barmouz et al. used FSP to create polymer nanocomposites with in-situ dispersion of clay particles into high density polyethylene (HDPE) [127]. This was accomplished by using a pinless tool to seal packed clay nanoparticles in a groove followed by a secondary tool with a pin to mix the clay particles in the HDPE. It was determined that certain processing parameters resulted in intercalated and exfoliated morphologies in the composite structure. Intercalated composites are products of polymer chains inserted between interlayers of the nanoparticles, while exfoliation occurs due to delamination of layers within the nanoparticles that allows for improved interaction between the polymer and filler particles [137]. These morphologies only occur at the nanoscale, which is why nanodispersed particle composites tend to perform better than microdispersed particle composites. Barmouz et al. determined that the polymer nanocomposite formed by FSP had significantly improved microhardness over both the parent HDPE material and nanocomposites formed by melt mixing due to high amounts of thermomechanical stress during FSP [127].

Large voids typically form in polymers when regions cool much faster than others, creating a hard boundary between the regions that allows for separation upon contraction from cooling [134]. Preheating, in-situ heating, and slow cooling of polymers during FSW and FSP has been shown to promote better mixing, increase crystallinity, reduce defects, and increase strength [83, 95, 134]. Several publications suggest that using auxiliary equipment such as heat plates to preheat the polymer, induction heated tools, or heated stationary shoes that prevent ejection of molten material and provide gradual and uniform heating and cooling [9, 83, 95, 102, 134, 135, 138] are necessary to FSW and FSP polymers. Azarsa et al. used a heated stationary shoe in conjunction with a rotating pin to form a copper/HDPE composite with nano-sized copper powder in a groove. The heated shoe simultaneously contained the filler material and processed composite while providing temperature control. They found improved mechanical properties ,which they attributed to interfacial adhesion between the filler and polymer, but did not comment on thermal or electrical properties of the composite [134]. Alyali et al. also used a heated shoe and pre-fabricated groove to form $PP/Al_2O_3$ nanocomposites and attributed improved mechanical properties to nucleation effects of the dispersed particles that reduced polymer spherulite size [135]. They also determined that too high of a filler content results in particle agglomeration which in turn reduces mechanical properties.

Though these FSP methods effectively formed polymer composites with enhanced mechanical properties, they require prior modification to the base material, which increases manufacturing complexity and diminishes the advantages of FSP over other composite forming methods. Furthermore, auxiliary equipment such as heating shoes may not be useful for curved surfaces due to inconsistent heating of the base material [83] in addition to geometric limitations. These works also do not address FSP of large areas and only focus on single passes. Thus, the feasibility of producing large processed areas through multiple passes and the resulting composite's properties at the interfaces between each pass requires exploration [17].

This work explores a novel method for FSP polymers called top plate friction stir processing, where a thin sheet of aluminum is processed into HDPE. Unlike other methods of FSP polymers, this method does not require preparing the polymer with grooves or using specialized heated stationary shoulders because the top sheet of aluminum simultaneously acts as the additive material and performs the duties of a heated shoe to contain the material and provide additional heat. This work explores the feasibility of performing composites with processed regions greater than one tool width, with an emphasis on improving electrical and thermal conductivites over the parent polymer.

## 5.2 Materials and Methods

6.35$mm$ (0.25") high density polyethylene (HDPE) sheet was the base polymer in this study and 1.01$mm$ (0.040") 6061 aluminum sheet was the top plate used as a filler material in the metal-polymer composite. A modified Milwaukee Model K milling machine performed the friction stir processing using a tool with a 25.4$mm$ (1") scrolled parabolic shoulder and threaded pin, which was expected to provide sufficient heat and material mixing in comparison to other tool pin types [61, 95]. The pin's dimensions were 6.35$mm$ (0.25") diameter and 4.5$mm$ length, and had left-handed threads with a pitch of 1.27 (20 TPI), which directs material flow downward when rotating clock-wise. Figure 5.1 shows a model of the tool used in this study.

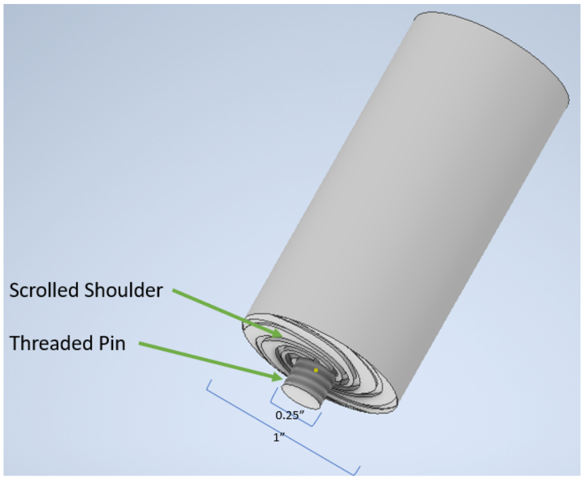

Figure 5.1: Model of FSP tool with 25 *mm* scrolled parabolic shoulder and 6 *mm* pin with left-hand 1.27 pitch threads. The tool is designed to rotate clock-wise.

Clamps secured the lapped aluminum on top of the HDPE to the milling machine anvil. Successive linear processing paths formed one large processed area on each sample. For each pass, the tool had a 1200 rpm rotation speed, 5.59*mm* (0.220”) plunge depth, 1.5° tilt angle, and a $64\frac{mm}{min}$ (2.5 ipm) traverse speed. These processing parameters were chosen from a preliminary study and were found to provide the best material mixing and surface finish with the tool and top plate used. Following the completion of a linear pass, the tool retracted from the material and returned to the starting location, where it shifted laterally to the retreating side before completing the next pass. Trials included tool shifts of 3.2*mm* (0.125”) and 2.5*mm* (0.1”) to determine the significance of tool shift between passes. This cycle continued for the number of desired processing passes, where a 25*mm* wide processed area could be accomplished using 8 successive passes for the 3.5*mm* tool shift and 10 passes for the 2.5*mm* tool shift.

An optical microscope was used to analyze cross sections of processed samples. Lenses magnified samples 50× so that particle distribution in different regions could be observed.

Electrical resistance measurements provided the means to determine electrical conductivity on processed samples. Initial resistance measurements were performed using a volt-ohm-milliameter (VOM) with two point probes on the top surface of each sample similar to those done in Tsai et al. [139]. This method provided inconsistent measurements for this work, and instead each sample was incorporated into a Wheatstone bridge. The following equation makes it possible to determine the electrical resistance through a composite specimen when incorporated into a Wheatstone bridge:

$$R_s = \frac{R_2 V_s - (R_1 + R_2) V_G}{R_1 V_s + (R_1 + R_2) V_G} R_3 \tag{5.1}$$

$R_1$, $R_2$, and $R_3$ are the resistances of the three other resistors in the Wheatstone bridge. $V_s$ is the voltage source, and $V_G$ is the measured potential difference between the two legs of the bridge circuit.

To connect each specimen to the Wheatstone bridge circuit, 25$mm$ copper pigtails were soldered to the top surface of each sample at approximately 17$mm$ apart (figure 5.2). The single pass samples had pigtails soldered along the center of the processed zone. The multi-pass samples had pigtails attached along the transverse and lateral axes in order to study directional conductive dependencies.

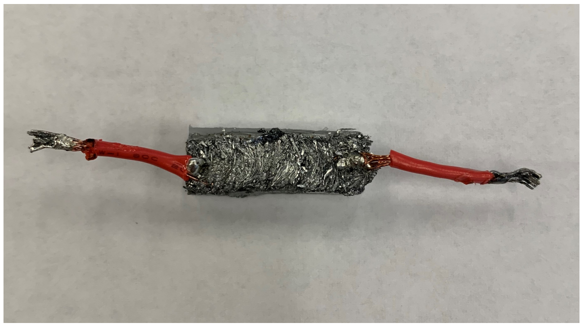

Figure 5.2: Copper wire pigtails soldered to processed composite samples.

Each composite sample underwent thermal conductivity tests in the same orientation as the electrical resistance measurements. The single pass composite samples were milled to 19$mm$ in the transverse direction and 9$mm$ lateral direction centered around the pin influence zone. The multi-pass samples were milled to 19$mm \times$ 19$mm$ so that the transverse and lateral directions had the same dimensions. Figure 5.3 shows the device used to perform thermal conductivity tests. A thermal-controller held the heat plate at a constant 80°$C$, and each sample was clamped in the device with one cross section face touching the heat plate. The steady state temperature at the opposing cross section was recorded with a thermocouple cemented in a small hole drilled into the sample. Fiberglass insulation packed around the specimens in the holder allowed for an improved 1-D heat transfer approximation. These tests were performed in a room at approximately 20°$C$.

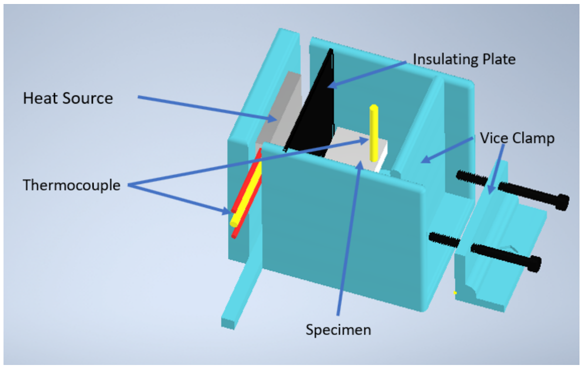

Figure 5.3: Specially designed vice to perform thermal conductivity tests. A vice clamp secures the face of a specimen against a heat source. The notched insulating plate reduces convective heating from the rest of the heat source. Fiberglass insulation (not shown) packed around the open faces further insulates the specimen. A thermocouple inserted at the opposing end of the specimen measures the temperature.

The thermal conductivity of each specimen was calculated using Fourier's Law:

$$k = \frac{QL}{A\Delta T} \tag{5.2}$$

where $Q$ is the heat flux, $L$ is distance between the heat source and the temperature reading, $A$ is the cross sectional area, and $\Delta T$ is the difference in temperature between the heat source and the maximum temperature recorded at the opposing end of the specimen. Assuming that the thermal conductivity of the pure HDPE is $0.44\frac{W}{mK}$ [140], $Q$ can be calculated using $\Delta T$ corresponding to a pure HDPE specimen.

Tensile tests on an Instron load frame were the basis for mechanical testing. $5mm$ wide specimens were cut along the transverse and lateral axes of specimens with both tool shifts to determine directional strength dependencies.

## 5.3 Results and Discussion

### 5.3.1 Parameter Effects

In this study, the top plate's high thermal conductivity provides increased heat distribution from the tool to the base polymer without auxiliary heating plates, heated tools, or stationary shoes. The plate preheats the unprocessed polymer forward of the tool, which reduces large temperature gradients that lead to material separation at the pin influence zone described in Simoes et al.[9]. Additionally, the top plate prevents ejection of the molten polymer, allowing for a consistent surface finish.

Initial tests used a $5.97mm$ (0.235") plunge depth to have full shoulder engagement. Excessive heating caused overmelting and squeezing of the HDPE, bulging the aluminum plate (figure 5.4). Plate bulging effectively further increased the plunge depth, resulting in flash and voids in the pin influence zone similar to those found in Azarsa et al. [134]. Reducing heat input can be accomplished by decreasing the plunge depth, which effectively reduces the shoulder contact area. Mitigating excessive heat input can only be accomplished with limited shoulder retraction, since the shoulder provides forging pressure necessary to contain the molten polymer on the aft end of the tool in the stir zone. A plunge depth of 5.59*mm* provided enough shoulder engagement to heat and soften the aluminum and HDPE without inducing plate bulging. Good processing quality is only possible with proper parameter selection. The tool must rotate fast enough to generate sufficient heat to melt the polymer, but overheating can cause the polymer to burn and degrade [9]. Likewise, the traverse speed affects local heat input, but also affects the cooling rate after the tool passes [134]. For HDPE, it is generally optimal to implement a high rotation speed and a slow traverse speed for good material mixing and low porosity [83]. While these parameters certainly affected processing quality, the plunge depth had the greatest impact on the processed surface finish in this study since it had the highest contribution to heat input.

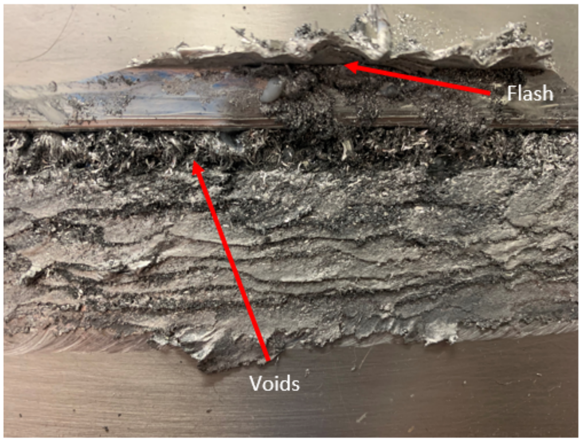

Figure 5.4: Poor processing quality as a result of top plate bulging.

Lateral tool shift distance employed in multi-pass specimens also had an effect on processing quality. Too large of a lateral shift between passes can reduce mixing, illustrated in figure 5.13. Sections *Electrical Conductivity*, *Thermal Conductivity*, and *Mechanical Properties* further discuss the implications of tool shift.

### 5.3.2 Material Distribution

### 5.3.3 Macro Analysis

A processing path shows distinct shoulder and pin regions following tool engagement. A single path produces a slight dwell in the aluminum surface due to shoulder contact. From the surface, there is very little evidence of HDPE since the aluminum sheet contains the polymer underneath. The pin's influence zone has a partially consolidated surface with some mixing that protrudes above the shoulder path. This region becomes elevated because the pin displaces molten polymer, causing it to flow upward after the tool passes. As a result of HDPE's low thermal conductivity [102], the polymer completely melts only in the pin's direct contact zone and under the hottest region of aluminum that is in contact with the tool shoulder. A small gap forms next to the pin's path due to a wall of forged aluminum that is pulled down into the plastic by the tool pin, but not mixed. This wall creates a mechanical interlock to secure the top plate to the lower polymer, shown in figure 5.5. However, the mechanical lock offers very little strength, as the top plate can be peeled from the HDPE base with little effort (figure 5.6). Thus in a manufacturing setting, the excess aluminum can be easily removed post processing.

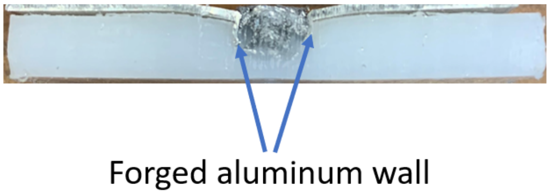

Figure 5.5: Cross section of single pass specimen. The arrows point to forged aluminum walls on the sides of the tool path.

The mechanical lock closely resembles the joints of friction stir lap welded Nylon 6 to AMXS6020 Mg alloy in Gao et al., though their configuration plunged the tool through the polymer lapped on top of Mg [141]. They report mechanical locking by means of Mg "horns" similar to the walls of forged aluminum in this study. Specimens failed under shear loads through separation of the nylon/Mg horn interlock. Maximum loads of $603N$ showed that lap welded polymers to metals, which is essentially a single pass top plate FSP, can offer shear strength, but tensile or peel load results were not reported. The mechanical lock has an even greater resemblance of a FSW joint between aluminum 6111 and polyphenylene sulfide (PPS) [142]. They report a very similar particle distribution in the stir zone along with a mechanical interlock with the lapped aluminum. Upon fracture, their specimens left a matrix path of aluminum chips and plastic similar to those shown in figure 5.6c.

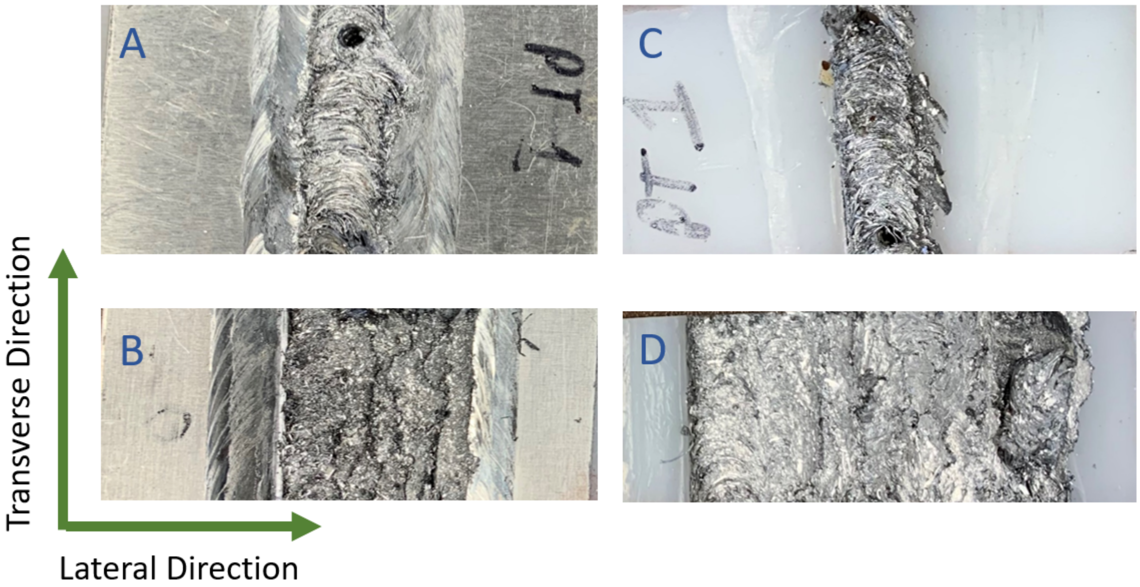

Figure 5.6: Single (A) and multi (B) pass processed sheet. Single (C) and multi (D) pass processed composite after removing unprocessed aluminum sheet.

Figure 5.7 shows the result of performing 9 successive overlapping passes. The material flow resembles the behavior reported in Simoes et al., with an asymmetrical thermo-mechanically affected zone (TMAZ) [9]. The first path in a series has relatively transparent material on the advancing side of the pin's influence zone with most aluminum deposited to the retreating side. Nine dark lines materialize from a high concentration of aluminum deposits along either side of the tool. The deposit tracks indicate aluminum fragments beyond the cross sectional surface, darkened by HDPE's opaqueness. Some aluminum fragments reside along a deposit track at the cross sectional surface. Therefore, the deposit tracks must not be continuous walls of deposited aluminum but are a high occurrence of deposited aluminum at the sides of the pin's influence zone. No deposit track exists on the advancing side of the first pass, which indicates that all of the large material deposited towards the retreating side. Other authors also report that the retreating side contains the most deposited material during FSW of polymers, which is unlike FSW and FSP of metals [83, 102]. However, a deposit track resides in the center of the first processing path. Because the tool shifted half of a pin width between each pass, the first deposit track resides on the advancing side of the second pass, which indicates increased mixing after the first pass. Increased mixing likely occurs after the first pass because the pin's leading edge only has contact with the aluminum sheet at the surface during the first pass, but has contact with both the aluminum sheet at the surface and deposited aluminum fragments during the successive paths (figures 5.8 and 5.9).

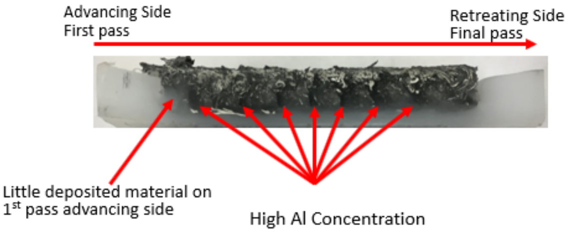

Figure 5.7: Cross section of 9 successive passes. The first pass is on the left, with each successive pass shifted towards the retreating side.

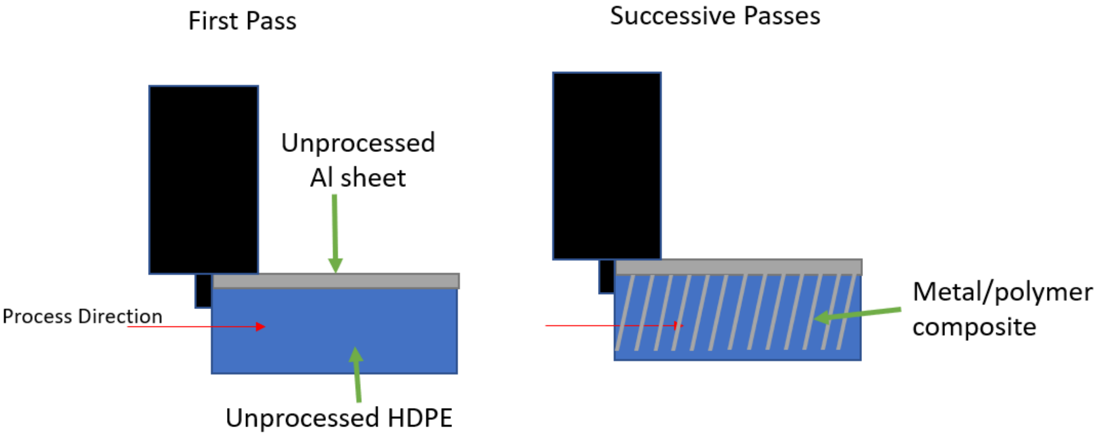

Figure 5.8: Left: Leading edge of tool pin in contact with unprocessed aluminum sheet on top and unprocessed HDPE on bottom during the first pass. Right: Shifted tool pin during successive passes is in contact with both processed composite and virgin material.

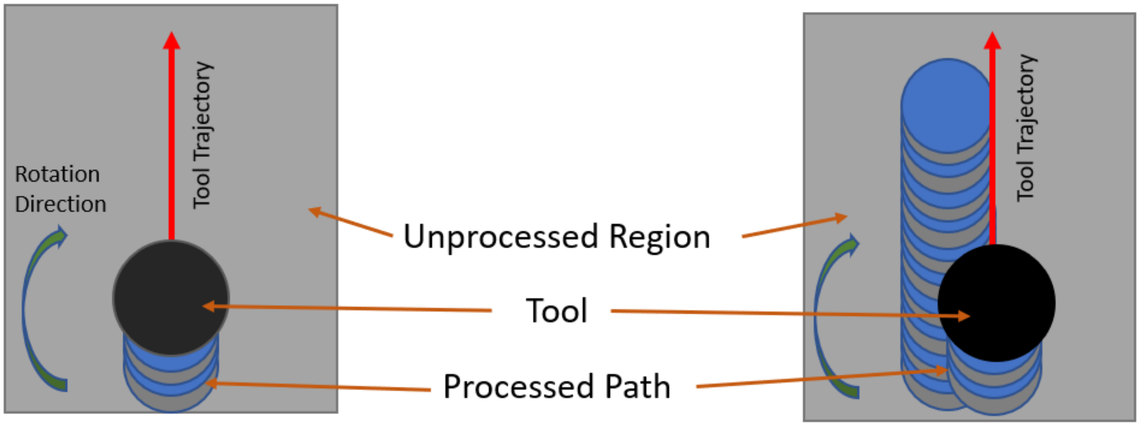

Figure 5.9: Top view of action described in figure 5.8

.

### 5.3.4 Optical Microscope Analysis

Microscope images of the processed cross sections sufficiently displays the material distribution and proximity of aluminum particles at varying depths of the newly formed composite. Figure 5.10 displays cross sections at various material depths from the top processed surface. Aluminum composes nearly all of the top surface with the largest fragments and close proximity. In this region, particles are approximately 50 $\mu m$ in size and have a large axial ratio. Figure 5.10a. shows a cross section at the top surface, indicating that most of the aluminum fragments have contact with other aluminum fragments. High concentration of aluminum near the surface provides the most contribution to electrical conductivity, as mentioned in section *Electrical Conductivity*. The volume fraction of aluminum decreases deeper into the HDPE base (figure 5.10b.) which explains the lower electrical conductivity below the surface. Significantly fewer particles reach the bottom of the pin influence zone (figure 5.10c.), but some larger aluminum fragments make their way to the bottom of the tool pin. Opacity variations in the HDPE show the heat affected zone (HAZ) boundary [102].

Though the following sections describe significant improvements to the electrical and thermal conductivity in the processed specimens over the parent HDPE, the clusters of large particles shown in figure 5.10 do not resemble optimal particle size and distribution described by Xue [130], Li et. al [131], and Fu et. al [132]. Exclusively changing typical processing parameters such as tool traverse rate, RPM, and plunge depth alone is not an effective solution to modifying the microstructure of the composite filler since the processing quality is so sensitive to these parameters. Rather, optimizing particle size and distribution may be achieved through modifications to the tool pin. For example, a shorter pin would reduce the spread of deposited particles and effectively increase the filler content at the surface. Variations in pin size and thread pitch may have an effect on the particle size since the tool pin pulls aluminum from the top plate into the polymer similar to a milling process [142]. The thread pitch will also have an influence on particle distribution and heat generation, where decreasing the thread pitch will increase heat generation and material flow [61].

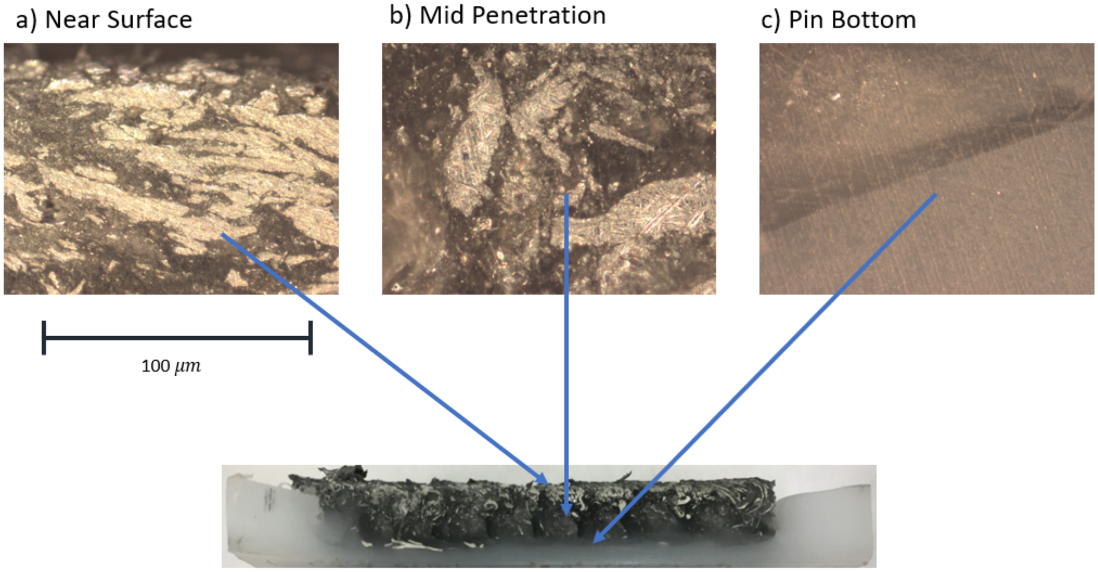

Figure 5.10: Microscope images of a processed sample cross section at various material depths. The 100 $\mu m$ scale bar applies to each magnified image.

### 5.3.5 Electrical Conductivity

VOM measurements were likely inconsistent due to aluminum oxidation and the differences in hardness between the aluminum and HDPE, though the top surface of each specimen consistently tended to have significantly less electrical resistance than the cross sections when probed. In Tasi et al., copper was spray coated on a polymer. Copper like most metals oxidizes when exposed to air, but copper oxide is highly conductive [143], making accurate VOM measurements on copper possible. Oxygen deposits on the aluminum create a thin film (on the order of $10\AA$) of chemisorbed atoms that increases contact resistance. Electrons can penetrate through these films via the tunnel effect, which results in a total contact resistance consisting of a constriction and tunneling resistance [144]. The tunneling resistance reduces given a high enough potential through fritting [144]. It is likely that a standard ohm meter does not produce a high enough potential for fritting to occur at the contact between the VOM probes and processed sample. However, the VOM was capable of making consistent resistance measurements with the unprocessed aluminum plates. Because the contact surfaces are not smooth at very small scales, the contact area is very small unless an applied load increases the contact area through elastic and plastic deformation [144]. The aluminum sheet easily deforms under load and makes good contact with the point probes. The processed samples, on the other hand, likely lack deformation in the aluminum fragments since the HDPE encompassing it deforms under load. Thus, even when a large load is applied to the point probes onto the processed samples, there is little increase in the contact area between the probes and aluminum fragments.

Incorporating specimens with soldered wire pigtails into a Wheatstone bridge provided significant improvements to the consistency of electrical resistance measurements. A good solder contact required that the pigtails be embedded in a melted region of the composite. The solder itself did not bond to the composite, but its flux likely helped to reduce oxidation in the aluminum, which in turn lowered contact resistance between the pigtails and composite samples.

Figure 5.11 shows box plots of the measured resistances of all samples. The single pass samples showed overall lower electrical resistance than the multi-pass. The multi-pass exhibit similar median values between lateral and transverse measurements, but the lateral measurements present a greater variance. Figure 5.12 shows boxplots of the same multi-pass data, but separates the composites that had different lateral tool shifts between passes. Again, the transverse resistance measurements exhibit a lower variance than the lateral measurements, but overall they report similar values.

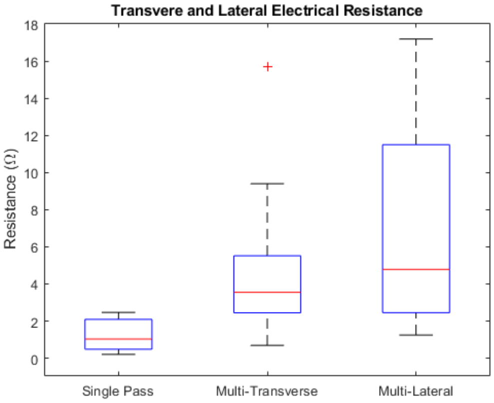

Figure 5.11: Electrical resistance for composite samples. The median electrical resistances are Single pass: 1.03 Ω, Multi-pass transverse: 3.55 Ω, Multi-pass lateral: 4.78 Ω.

The slightly different behavior between the 3.2 *mm* shifted samples and 2.5 *mm* shifted specimens is likely due to the following explanation. Many of the 3.2 *mm* shifted specimens contain solid rails of aluminum embedded along the transverse axis, shown in figure 5.13. These rails are remnants of the forged aluminum walls described in section *Macro Analysis*. Noise in the lateral motor's positioning in addition to table movements from backlash in the milling machine allowed for the tool to have lateral displacements greater than the intended 2.5 *mm* during some passes, preventing the tool from mixing and distributing the aluminum walls from a previous pass. During transverse resistance measurements, the solid aluminum rails provided a low resistance electrical path to the other end of the sample. The opposite effect was observed for the lateral resistance measurements. Contact resistance between the aluminum rails and mixed composite contributed to additional resistance in the lateral direction. Furthermore, the 3.2 *mm* samples did not all have the same number of aluminum rails, which contributes to the greater variance of electrical resistance in the lateral direction over the transverse direction.

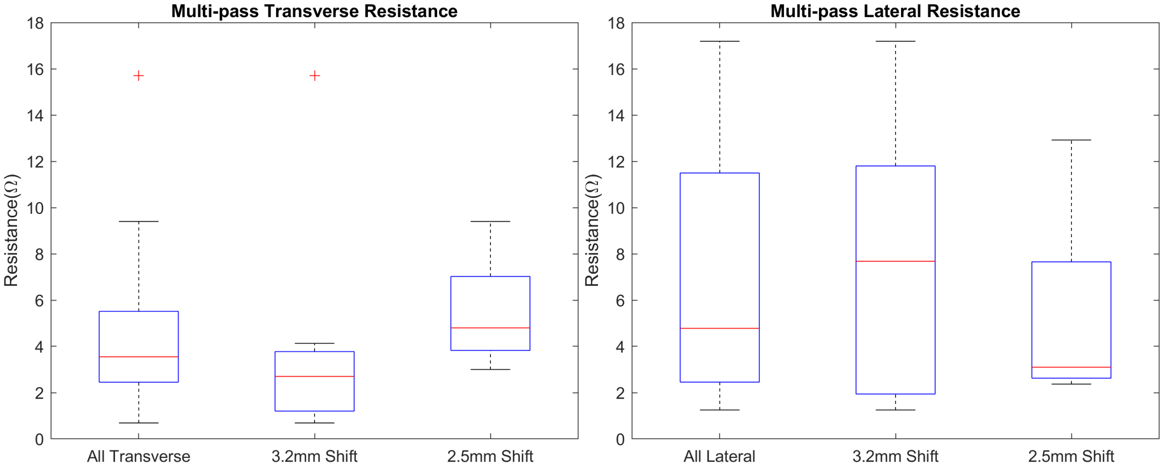

Figure 5.12: Multi-pass resistance measurements split between 3.2 *mm* and 2.5 *mm* lateral shifts between passes.

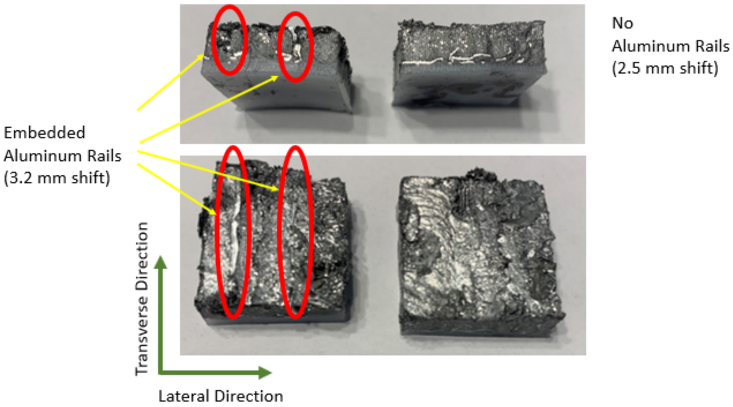

Figure 5.13: Top: Cross section view. Bottom: Surface view. Left: 3.2 *mm* shifted sample with embedded rails present along transverse axis. Right: 2.5 *mm* shifted sample with no embedded rails present along the transverse axis.

The following conclusions can be made from the electrical resistance measurements. Top plate FSP can effectively form electrically conductive paths in a polymer. Though Azarsa et al. suggests the possibility to improve electrical properties in polymers with FSP [134], these results show that composites with relatively low electrical resistance can be formed. However, forming a good electrical contact with the polymer composite is significantly more challenging than a pure metal, which may limit the methods to connect electrical equipment to polymer composites, especially in low voltage situations where fritting does not occur. Lower voltage applications may require the use of metal fillers with higher conductivity and lower contact resistance, such as copper. There does not appear to be a significant directional dependency for the electrical resistance in polymer composites formed by top plate FSP, but consistent electrical properties in processed polymer composites will require careful monitoring of equipment during processing for good composite quality. The low electrical resistance is attributed to the high filler content at the composite surface and large aluminum particle axial ratio, but the deposited micro particles present in section *Optical Microscopy* suggest that further particle size will further improve electrical conductivity [130].

### 5.3.6 Thermal Conductivity

Figure 5.14 shows the distribution of calculated thermal conductivities for all specimens. The median values for the single pass, multi-pass transverse, and multi-pass lateral are $\kappa_{single} = 0.65\frac{W}{mK}$, $\kappa_{trans} = 0.92\frac{W}{mK}$, and $\kappa_{lat} = 0.74\frac{W}{mK}$. These values correspond to a 48%, 108%, and 69% increase in thermal conductivity compared to unprocessed HDPE, respectively.

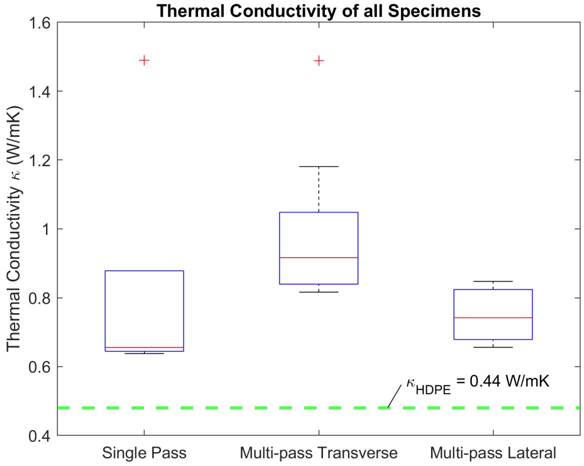

Figure 5.14: Thermal conductivity calculated for all specimens. The horizontal line within each box represents the median values. The pluses are outliers. The dashed line represents the thermal conductivity for unprocessed HDPE for reference.

Single pass processed paths had the smallest median improvement on conductivity compared to the multi-pass specimens. This is attributed to the formation of forged aluminum walls described in section *Macro Analysis*, which causes a lower density of aluminum in the formed composite. The aluminum rails were removed prior to testing to better capture the conductivity of the composite itself. However, one single-pass sample contained an aluminum rail that was deeply embedded, making removal impossible without complete destruction of the specimen. This explains an outlier value of $1.48\frac{W}{mK}$ seen in figure 5.14. During the successive passes in the multi-pass specimens, the aluminum walls become mixed into the composite, which increases the density of aluminum particles and effectively improves thermal conductivity.

Figure 5.15 plots the distribution of the transverse and lateral thermal conductivities with the variable tool shifts between lateral passes. Lateral tool shifts between transverse passes has a small influence on thermal conductivity, corresponding to observations in section *Electrical Conductivity*. Embedded rails visible in $3.2mm$ shifted specimens provided paths of lower thermal resistance in some samples, which contributes to the larger range of values between specimens. The thermocouple in one transverse specimen was cemented very close to one of the embedded rails, which explains the high outlier thermal conductivity of $1.49\frac{W}{mK}$. The smaller tool shift between passes reduced the directional dependency in thermal conductivity. The transverse and lateral directions had a $0.19\frac{W}{mK}$ difference in median thermal conductivity for the $3.2mm$ shifted specimens, while the $2.5mm$ shifted specimens had only a $0.12\frac{W}{mK}$ difference. The smaller directional dependency in the $2.5mm$ specimens is attributed to lower contact resistance between mediums in the lateral direction and greater material homogeneity.

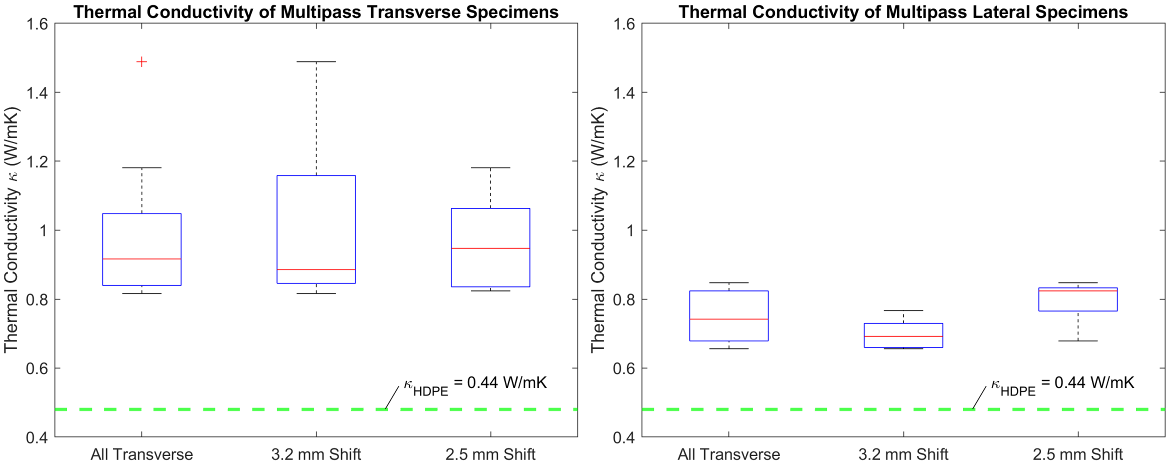

Figure 5.15: Multi-pass calculated thermal conductivities split between tool shifts. The horizontal line in each box represents the median values. The pluses are outliers. The dashed line represents the thermal conductivity for unprocessed HDPE for reference.

The values reported are merely estimates for the change in total thermal conductivity of an HDPE base, and do not solely represent the thermal conductivity of the composite region since the calculations include HDPE beneath the stir zone. The thermal conductivity likely varies with material depth, since the density of embedded aluminum and matrix of touching aluminum particles varies, as seen in section *Optical Analysis*. Though top plate FSP greatly improves the thermal conductivity of HDPE, it is still orders of magnitude less than pure aluminum. Increasing the filler content in a composite will effectively improve the thermal conductivity. However, increasing the filler content of HDPE with a highly conductive material up to around 20% has been shown to form a composite with $\kappa \approx 3\frac{W}{mK}$ [140], which is still comparatively low to the thermal conductivity of the sole filler material. The filler content may be altered in top plate FSP by simply changing the thickness of the aluminum sheet used. Doing so would require further study, as the processing parameters would likely need adjusting to control heat input. Similar to electrical conductivity, reducing the aluminum particle size may also improve thermal conductivity for a given filler content from greater particle dispersion due to the aggregation effect [131]. Though metal/polymer composites formed by top plate FSP have significant improvements to the thermal conductivity over the base polymer, they will not be a direct substitute for metal structures requiring significantly higher thermal conductivity.

### 5.3.7 Mechanical Properties

Table 5.1 reports the median ultimate tensile strength ($UTS$) and load vs deflection slope in the linear regime for the HDPE and composite samples of both tool shifts. Figure 5.16 shows the distribution among specimens.

Table 5.1: Ultimate tensile strength and load vs deflection slope reported in $MPa$. $T_{2.5}$ and $T_{3.2}$ refer to samples of the respective tool shifts with loads applied along the transverse axis. $L_{2.5}$ and $L_{3.2}$ refer to samples of the respective tool shifts with loads applied along the lateral axis. $UTS\%$ refers to the percentage of ultimate tensile strength in the processed specimens compared to the parent HDPE.

| **Type** | $UTS$ **(MPa)** | $UTS$ **%** | **Load vs Deflection Slope (MPa)** |
|---|---|---|---|
| Unprocessed HDPE | 28.1 | 100% | 849 |
| $T_{2.5}$ | 11.9 | 42% | 1034 |
| $T_{3.2}$ | 15.0 | 53% | 1216 |
| $L_{2.5}$ | 13.5 | 48% | 757 |
| $L_{3.2}$ | 5.7 | 20% | 676 |

The specimens experienced a severe decrease in UTS compared to the base HDPE, though $T_{2.5}$, $T_{3.2}$, and $L_{2.5}$ have comparible values to the 50% FSW joint efficiency between HDPE and AA5059 reported in Khodabakhshi et.al [145]. The 2.5 *mm* tool shift produced ultimate strength relatively homogeneous between each axes. The 3.2 *mm* tool shift produced a large disparity in ultimate strength between directions, with the lateral direction being significantly weaker than the transverse direction. The weakness in the lateral direction is due to poor mixing between passes; each specimen fractured at the boundary between passes, predominantly at the embedded unmixed aluminum rails mentioned in section *Electrical Conductivity*. Strength between the parent HDPE and deposited aluminum comes from a combination of mechanical interlocking and interfacial adhesion, though the interfacial adhesion is inferior to the mechanical interlock [145].

The composite region is brittle by comparison to the parent HDPE, adding complexity to tensile fracture since an approximate 2 *mm* thick unprocessed region is at the bottom of each specimen. Additionally, the particle loading and particle size varies with depth of the composite region, so it is expected that the strength and elasticity varies with material depth. The slopes of load versus deflection curves for the transverse and lateral specimens show that the processed specimens have directional dependent stiffness. The transverse specimens have similar slopes that are significantly greater than the lateral specimens, which may be a consequence of deposited particle orientation and concentration. As mentioned in section *Macro Analysis*, higher concentrations of aluminum deposit along the tool path, which gives the composite higher rigidity along the transverse direction compared to the lateral direction.

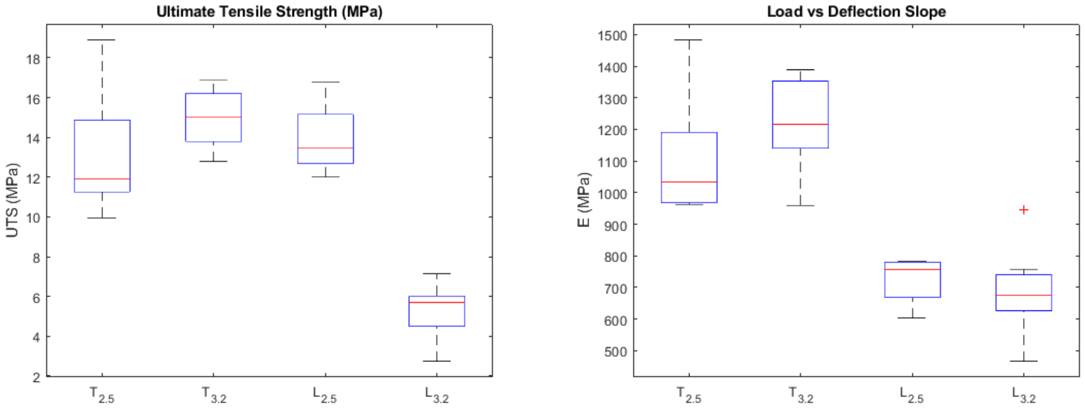

Figure 5.16: Distribution of $UTS$ and load vs deflection slope for all specimens. The horizontal line in each box represents the median values.

The processed specimens have an overall density of 1025 $\frac{kg}{m^3}$ compared to the parent HDPE's density of 950 $\frac{kg}{m^3}$. The significant reduction in strength with an increase in weight leaves room for improvement. However, reducing particle size to small micron and nano-scales will drastically improve the mechanical properties because it increases the surface area for interfacial adhesion and stress transfer between the polymer and filler material [132]. It has been shown that forming clay-polymer [127], metal-polymer [134], and alumina-polymer [136] composites via FSP can improve mechanical properties over the parent polymer. In these studies, however, the embedded particles were nano-sized prior to processing. The improved mechanical properties from nano-sized fillers are attributed to improved particle interaction due to intercalation and delamination in the composite structure [127], high interfacial adhesion between dispersed particles and polymer matrix [134], and nucleating effects of the deposited particles that reduces polymer spherulite size upon cooling [135].

Top plate processing in this study requires the tool to form small particles from a large sheet. The suggested tool optimization to reduce particle size described in section *Optical Analysis* will potentially improve mechanical properties. The composite may also benefit from enhanced heat input from the suggested tool optimization due to increased melting of longer polymer chains specifically in the stir zone [134], as increasing heat input through the top plate may cause overmelting and shape deformation throughout the entire polymer structure beyond the targeted processing region. Tool optimization will also allow more experimentation with traverse rate, which effects compression in the stir zone. Higher compression of the polymer in the stir zone induces more thermo-mechanical stress which improves dispersion of particles [95, 134]. If the traverse rate were increased, then a finer thread pitch would be necessary to counter the increase in particle size from the top plate [142]. Thus, improving the composite strength requires an extensive study to match optimized tool geometry with compatible processing parameters.

## 5.4 Conclusion

In this study, metal-polymer composites were formed using top plate friction stir processing. The following describes the benefits of this new technology:

- Metal-polymer composites can be formed without prior modification to the base polymer material. The top plate conveniently serves multiple purposes, including temperature control, polymer containment, and filler material supply. Reducing the number of processing steps increases manufacturing efficiency.
- This study demonstrates the feasibility of producing large processed areas from multiple passes, which has yet to be shown prior to this study [17].
- Eliminating a bulky heated shoe may allow FSP on contour surfaces. In order to do so, the top plate may be stamped to match the contour surface of the base polymer.
- Top plate FSP effectively creates electrically conductive paths in the base polymer with relatively low resistance. FSP electrically conductive paths may be used for multi-functional structural polymers for housing electronics. It may also be used solely to dissipate build up of charges, such as those resulting from space plasma [146].
- The aluminum-HDPE composite formed by top plate FSP has greater capability to conduct and transfer heat than the base HDPE. This may reduce the amount of heat dissipating equipment needed, such as thermal straps, for structures made from polymers which may reduce an assembly's size and weight.

Though top plate friction stir processing shows promise to efficiently form metal-polymer composites, further study is needed to make it a competitive alternative to other manufacturing processes. The parameters and tool geometry presented in this study form composites with a significant reduction in strength from the parent HDPE, giving it a poor strength and weight trade-off for improved electrical and thermal properties. Thus, in its current form top plate FSP is only viable to form thin surface composites rather than bulk composites. Reducing the aluminum particle size through tool optimization in future work is necessary to improve metal-polymer interaction.

Other composites formed from different combinations of metals and polymers may also benefit from top plate FSP. Further studies will require experimentation with tool type and operating parameters due to different material mixing behaviors.

# CHAPTER 6

## Friction Stir Welding of Lapped Low-melt Polyaryletherketone Carbon Fiber Reinforced Thermoplastic Laminate

The following work was previously published in the *Journal of Composite Materials* as:

L. T. Wilkins, A.M. Strauss, Friction Stir Welding of Lapped Low-melt Polyaryletherketone Carbon Fiber Reinforced Thermoplastic Laminate, *Journal of Composite Materials*. August 2023;57:25;

### Abstract

Carbon fiber reinforced thermoplastics (CFRTP) have increasing use in aerospace structures due to improved process-ability and weldability. In this study, lap joints between carbon fiber reinforced low-meltpolyaryletherketone (LMPAEK) are formed by friction stir welding (FSW). This study presents novelty by applying FSW to continuous carbon fiber composites in woven laminate form. FSW disrupts the fibers in the weld zone and distributes fragments as small as several microns in length. Thermal analysis shows that the weld zones degrade at 40°C cooler temperatures than the base laminate material due to enhanced polymer mobility surrounding the disrupted carbon fibers. Though optimized joints have regions of over 9% porosity, tensile strengths of up to 73.8 MPa retains up to 50% joint efficiency of a comparable short carbon fiber reinforced composite. CFRTP also requires lower processing forces during FSW than metals, and the power consumption of 67 W during the traverse period for strength optimized welds retains energy efficient characteristics.

### 6.1 Introduction

Implementing lightweight structures into aerospace vehicles is imperative to increase cargo capacity and improve efficiency. Carbon fiber reinforced plastics have increasing popularity due to improved specific strength, corrosion resistance, and damping capacity [147] that allows for a 20%-40% weight reduction compared to conventional metallic materials [148]. Carbon fiber reinforced thermoplastics (CFRTP) have growing attention in aerospace industries due to non-definite shelf life, rapid cure times, high tensile strength, high fracture toughness, and good chemical resitance [149, 150]. Unlike thermosetting polymer matrices, the molecular arrangement in thermoplastics allows them to re-melted, re-processed, and ultimately, welded. Aerospace structures regularly use polymer matrices from the family of polyaryletherketones (PAEK) such as PEEK and PEKK due to their attractive mechanical properties, chemical resistance, and glass transition temperatures suitable for aerospace applications. Most PAEK's have a ratio between the melting and glass transition temperature of 1.5. Their high melting temperatures make them difficult to process and weld. Recently, low-melt polyaryletherketone (LMPAEK) was developed with a reduced ratio between the melting and glass transition temperature of 1.35 [151]. LMPAEK is easier to process and weld than PEEK with little compromise to mechanical properties and rigidity at high temperatures. The Clean Sky 2 Multifunctional Fuselage Deomstrator [43] and PROCOMP's upper stage $LH^2$ propellant tank [42] are examples where LMPAEK serves as the matrix in welded composite structures.

Recently, extensive research has explored joining various fiber reinforced thermoplastics using friction stir welding (FSW). FSW utilizes a rotating tool plunged into the joining materials to heat and soften them through friction and plastic deformation [44]. The rotating tool sweeps and mixes the joining materials in the weld zone. Because intertwined polymer chains require them to be melted during thermoplastic welding processes, FSW is a liquid state joining process for polymer composites [9].

A typical FSW joint contains several zones including the base material, heat affected zone (HAZ), thermo-mechanically affected zone (TMAZ), and the nugget. Most polymer weld joints do not have a heat affected zone extending beyond the TMAZ due to their extremely low thermal conductivity. Without consideration of finely tuned welding parameters, inadequate heat transfer through the weld thickness can induce poor material flow and poor polymer diffusion, resulting in tunneling, porosity, root defects, and kissing bonds that hinder mechanical strength [9, 17].

The tool rotation speed and traverse speed affects the size of the material flow zone in a polymeric FSW joint which has been shown to correlate with weld strength [68]. Though many parameters ultimately affect joint integrity, a general consensus is that the tool rotation and traverse speeds are of greatest influence [152]. Tool rotation speed is responsible for heat generation [31]. Kordestani et al. joined both 30% wt. glass fiber and 30% wt. carbon fiber reinforced polypropylene in butt weld configuration, citing large tunneling defects when using low rotation speeds due to inadequate processing temperatures [153]. However, too high of a rotation speed can overheat and eject materials from the weld zone [83]. Not only can overheating the polymer oversoften it, but it can also thermally degrade the polymer in the form of oxidation, cross-linking, and chain rupture that ultimately leads to losses in mechanical properties and changes in appearance [23].

The tool traverse speed is the most influential in controlling the heat transferred through the material thickness [68]. Slow traverse speeds maintain a molten polymer pool behind the tool and further promote interdiffusion across the joint [17]. Ahmadi et al. joined 20% wt. short carbon fiber (SCF) reinforced polypropylene in lap joint configuration [13]. A maximum tensile shear strength of 6.06 MPa was achieved through parameter optimization, with the traverse speed as the greatest contributor to strength. Other influential welding parameters include the tool tilt angle and plunge depth. The tool tilt angle is usually considered when utilizing shouldered tools as it influences vertical and horizontal material flows [153, 154]. The plunge depth dictates the degree of pin interaction with the joining material as well as the forging pressure of the shoulder at the surface [155]. Adequate axial pressure promotes material consolidation necessary to prevent formation of voids and other defects. The tool shoulder and pin geometry influence heat generation and material flow. Required spindle torque and peak temperatures have been shown to be proportional to shoulder diameter [156]. Additional shoulder features, such as spiral scrolls, can act as wipers to smooth the weld surface. They can serve the purpose of directing material towards the center pin and reduce expulsion of material [157]. Researchers have excessively studied the influence of center pin geometry during polymer FSW. Of all pin geometries, threaded probes generally result in the best weld quality since they promote vertical flow of material that adequately mixes the weld zone. Threaded pins also have a large surface area to generate frictional heat and ultimately produce the least porosity of other pin geometries [152]. Kordestani et al. studied the effects of tool pin geometry on butt welded joints between similar 30% wt. SCF reinforced polypropylene. Tools with threaded tapered pins produce the maximum tensile strength, achieving up to 34% of the base composite's strength [158].

Reinforcing fibers add complexity to polymeric FSW due to fiber disruption. Carbon fiber is an extremely abrasive material [159] and causes premature wear on standard FSW tools made of H13 tool steel [160]. Fiber disruption during FSW and related processes also reduces fiber size and changes their reinforcing properties [161, 162, 163]. For example, General Motors Global R&D report 50% reduced fiber length in the weld zone of friction stir scribe joined SCF 45-polyamide 6 and aluminum.

The critical fiber length $L_c$ is the minimum length of reinforcing fiber that improves the mechanical strength over the neat polymer. $L_c$ can be calculated by equation 6.1 [162]:

$$L_c = \frac{\sigma_{Fb} d_f}{2\tau_b} \tag{6.1}$$

$\sigma_{Fb}$ is the fiber breakage resistance, $d_f$ is the diameter of the fiber, and $\tau_b$ is the shear strength of the polymer. According to Meyer et al. fragmentation and reduction of glass fiber length below the critical fiber length in the weld zone limits the joint strength to that of the neat polymer [162]. However, fiber disruption in FSW joints can be beneficial to mechanical properties due to realignment of fibers. Czigany et al. observed random deposited fiber orientation and interlacing across the joint in glass fiber reinforced polypropylene. The unique material transfer during FSW was attributed to improved joint strength compared to conventional welding methods [161].

There are a limited number of studies concerning FSW joints between similar CFRTP. Additionally, the majority of studies joining CFRTP use SCF reinforcement. However, most large aerospace structures manufactured with CFRTP utilize continuous fibers, both in laminate and unidirectional tape form. Thus, a greater focus on welding technologies to join CFRTP composed of continuous carbon fibers is necessary to meet the needs of future aerospace industries. FSW lags behind other welding technologies for thermoplastic applications, though it may prove to be highly beneficial in joining thermoplastics reinforced with continuous carbon fibers. This study is the advent of such research with the formation of woven carbon fiber reinforced LMPAEK lap joints using FSW. Parameter optimization of tensile strength, morphology characterization, and thermal analysis lay the groundwork for future study and identify areas of necessary improvement.

## 6.2 Material and Methods

### 6.2.1 Materials

Carbon fiber reinforced low-melt polyaryletherketone (LMPAEK) sheet supplied by Toray Advanced Composites served as the joining material in this study. Four layers of Toray Cetex TC1225 2/1 twill weave in [(0.90)]2S layup composed the laminate sheets with a thickness of 1.2 mm. Figure 1 illustrates the orientation of the fabric weave with respect to the 0° and 90° directions.

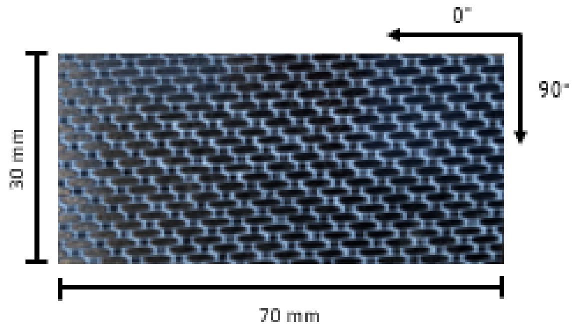

Figure 6.1: Cut laminate sheet dimensions and respective fiber orientations.

Specimens were cut to dimensions of 30 mm × 70 mm using a wet tile saw with a diamond tipped blade. Due to the abrasive nature of carbon fibers and risk of delamination, the tile saw provided the highest quality cuts over other cutting methods available. The cut sheets were lapped along the 0° direction with a 15.75 mm overlap. FSW was conducted using a Simulink controlled modified Kearney and Trecker Milwaukee Model K milling machine at the Vanderbilt University Welding Automation Lab (VUWAL). The tool consisted of a 25.4 mm scrolled parabolic shoulder and removable 6.35 mm diameter threaded pin set to 1.14 mm in length. The threads had a pitch of 0.79 mm (32 TPI) in the left-hand orientation, facilitating downward material flow during a clockwise rotation [71].

### 6.2.2 Preliminary Experimentation

The material novelty of in this study required preliminary experiments to establish general welding parameters. All preliminary and further studied welding experiments in this manuscript used a weld sequence

Table 6.1: CFRTP Welding Parameters

| Level | | 1 | 2 | 3 | 4 | 5 |
|---|---|---|---|---|---|---|
| **A** | Rotation Speed (RPM) | 600 | 800 | 1000 | 1400 | 1800 |
| **B** | Traverse Speed (mm/min) | 10.2 | 30.5 | 50.8 | n/a | n/a |

following the VUWAL's default weld program, which utilizes a 5.08 mm/min plunge rate, a four second dwell at maximum plunge depth, tool traverse, and a four second dwell at the end of the weld followed by tool retraction. Tool pin length and overall plunge depth was established through incremental adjustments using a 1500 RPM rotation speed and 25.4 mm/min traverse speed. A 1.52 mm plunge depth was found optimal for the tool used in this study by visual inspection as shallower plunge depths did not consolidate the surface and deeper plunges cause further thinning of the welded joint. A 1.5° rearward tool tilt proved adequate across a variety of material types with this tool shoulder geometry, justifying its implementation in this study. Further preliminary experiments focused on determining the effect of weld traverse direction, since one direction places the tool's advancing side along the lapped edge, and opposite welding direction places the tool's retreating side along the lapped edge. The preliminary study was conducted using all combinations of levels 3 and 5 for rotation speed and levels 1 and 3 for traverse speed listed in table 6.1. The welding direction orienting the advancing side along the lapped edge produced greater average tensile strengths and was used for the remainder of the study.

### 6.2.3 Parameter Experimentation

The effects of tool rotation speed (A) and traverse speed (B) were tested in a 2 parameter, full-factorial design of experiments. Table 6.1 lists the ranges of A and B. Levels 3-5 were originally of interest for parameter A based on a similar range used by other researchers [163]. However, levels 1 and 2 were later added to capture the effects of lower rotation speeds. A minimum of three replicate welds for each parameter combination performed in separate blocks accounted for unintended environmental variations.

### 6.2.4 Evaluation

Mechanical tests consisted of tensile testing on an Instron load frame. Specimens were cut 14 mm wide across the lap welded sheets using a wet diamond saw with a 10 mm minimum distance from the plunge location. Two tensile specimens were cut from each weld. Emory cloth bonded to carbon fiber pads compensated for the lapped sheet offset during tensile testing. The load frame crosshead travelled at a constant 2

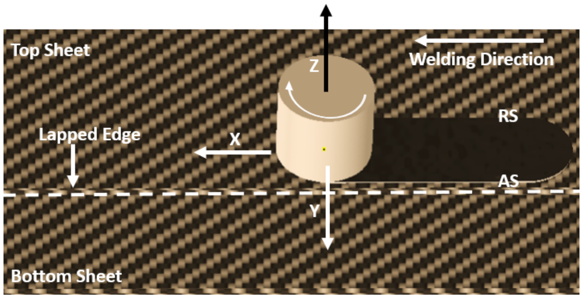

Figure 6.2: Schematic of welding setup. The dynamometer measures forces in the axial (Z), lateral (Y), and traverse (X) directions in addition to the torque around the rotation axis. The weld direction goes from right to left.

mm/min according to the ASTM designation D3039-08. Microstructure characterization consisted of optical microscopy and scanning electron microscopy (SEM). Weld cross sections were sanded with up to 600 grit sand paper. Polishing with 5 $\mu$m and 1 $\mu$m particle slurries concluded the surface preparation. Particle sizing and dimensional analysis was performed using ImageJ. Thermogravimetric analysis (TGA) and differential scanning calorimetry (DSC) was used for thermal analysis on a TA Instruments Q600 SDT. Neat laminate and weld zone specimens were clipped using diagonal pliers. Analysis used heating curves sweeping from 20°C to 600°C at a rate of 10°C/min. Welding forces in the axial, lateral, and traverse directions and spindle torque were measured using a Kistler type 9123C dynamometer mounted to the machine spindle. Figure 6.2 references the welding directions with respect to the weld setup.

Parameter effects on mechanical properties and welding forces were analyzed using Minitab Statistical Software, where a parameter's statistical significance was evaluated on a 95% confidence interval ($p \leq 0.05$ ).

## 6.3 Results

### 6.3.1 Surface Integrity

Figures 6.3a, 6.3b, and 6.3c display the surface appearance of multiple welds with varying parameters. Generally, FSW created joints with smooth and consistent surfaces for most parameter combinations. Severe surface delamination was characteristic of 600 RPM and 800 RPM welds and welds with 50.8 mm/min traverse speeds. The delamination results from cold welding parameters that fail to provide the thermal input necessary to promote polymer diffusion. Welds with the parameter combination of 1000 RPM and 30.5 mm/min had the most consistent and highest quality top surface appearance. Excessive flash occurred during 1800 RPM welds due to over softening of the material. This material expulsion reduced shoulder contact with the top surface and formed voids and inconsistent surface appearance from the lack of forging pressure.

Figure 6.3d shows the underside of the welded sheets. The weld zone does not penetrate through the entire thickness of both sheets, leaving a completely unaltered surface appearance under the weld zone. Figure 6.3e shows an edge on view of the lap welded sheets.

### 6.3.2 Microstructure

FSW influences non-homogeneous material morphology throughout the width and thickness of the weld as a result of mechanical material interaction with the tool and variable processing temperatures. Figure 6.4 reveals the cross section of a welded specimen with 1000 RPM and 30.5 mm/min parameters. All weld parameter combinations present similar morphological characteristics as those presented in figure 6.4 from a wide view, though further discussion highlights parameter influence at microscopic scales.

The weld cross section can be characterized into five distinct zones. Zone I represents the base material (BM) outside of the thermomechanically affected zone (TMAZ). Regions II and III represent the boundary between the TMAZ and BM, where region II lies at the advancing side (AS) interface and region III lies at the retreating side (RS) interface. The TMAZ comprises regions IV and V, where the shoulder affected zone (SAZ) lies in region IV and the pin affected zone (PAZ) extends into region V. Region V primarily lies within the bottom laminate sheet.

The composite laminate undergoes heavy transformation in the TMAZ since the FSW process must disturb the fibers in order for mass material flow and mixing to occur. Material flow is complex as the polymer has a sharp temperature dependent gradient between a solidus state, a highly ductile material, and a liquid, while the continuous carbon fibers are processed into short particles. Shearing effects further reduce fiber sizes post fragmentation from the long fibers. Figure 6.5 and figure 6.6 show the transformation of continuous fibers to small fragments. In figure 6.5, the continuous fibers have relatively uniform circularity with a $7\mu$m diameter. In figure 6.6, chopped fibers show splintered surfaces of variable sizes encapsulated in the matrix.

Flow stresses orient the fibers to the flow field [163]. In region IV, fibers up to 150 $\mu$m long orient primarily parallel to to the weld cross section. The shoulder sweeps the fibers in region IV and deposits them tangent to the shoulder's aft end, thus orienting many of the fibers across the weld. Fiber orientation in the weld is analogous to injection molding of SCF composites. It has been shown that SCF's located near part/mold edges tend to orient parallel to mold walls in the flow direction, resulting in the part's mechanical properties favoring that of the fiber orientation [164]. Thus, particles in the center of the weld zone orient mostly across the joint, while particles near the edges of the weld zone favor orientation to the weld seam.

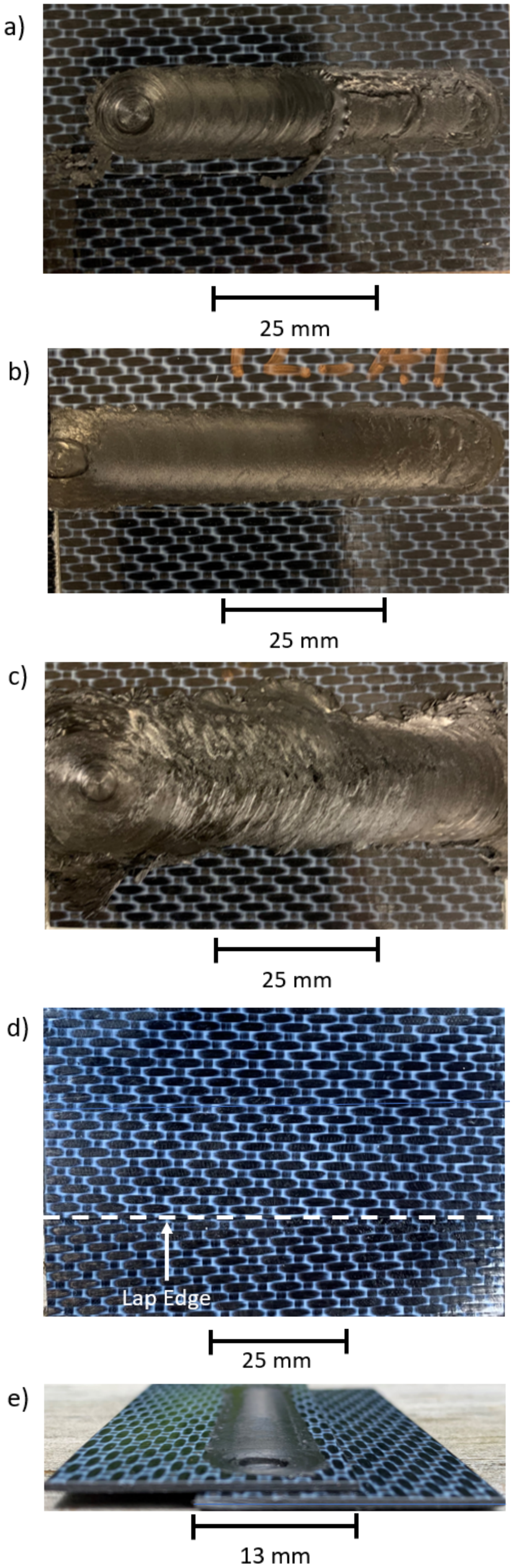

Figure 6.3: Typical surface appearance of selected welds. a) 800 RPM b) 1000 RPM c) 1800 RPM d) Bottom view e) End view

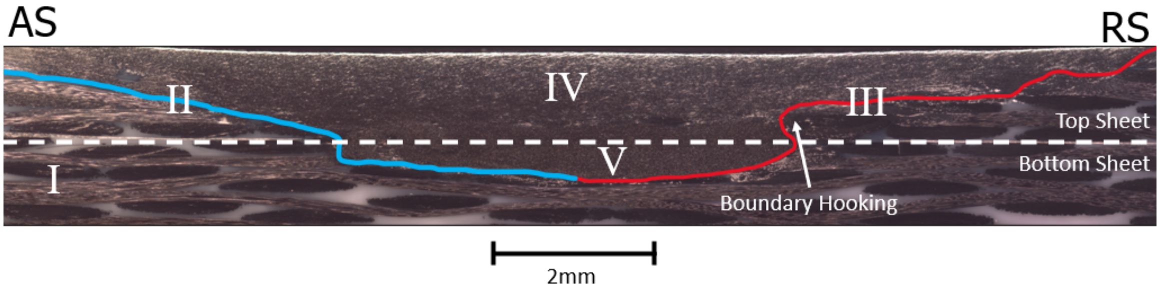

Figure 6.4: 1000 RPM, 30.5 mm/min weld specimen cross section

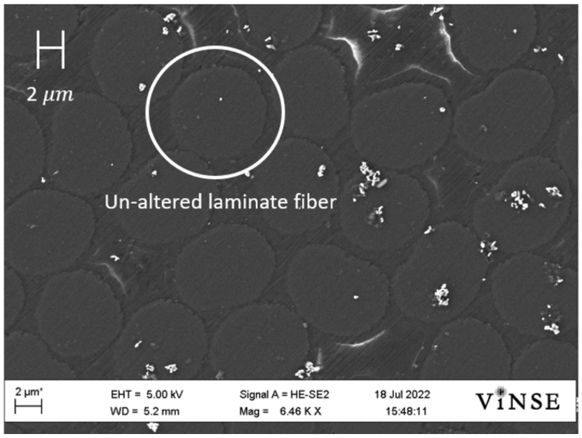

Figure 6.5: SEM cross section of carbon fiber laminate. The fibers are oriented normal to the page.

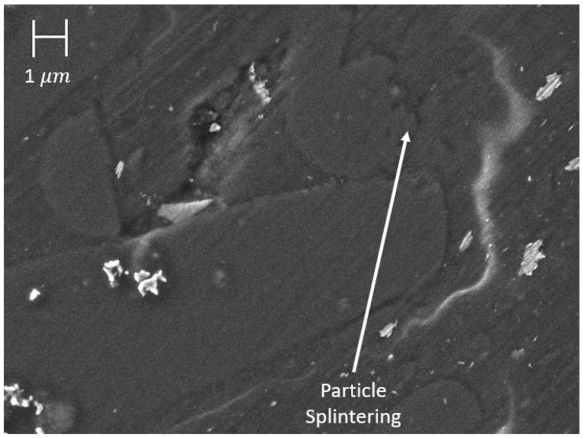

Figure 6.6: SEM micrograph of the stir zone cross section. Broken fiber ends show splintering.

Table 6.2: Void content and carbon fiber particle dimensions for regions IV and V.

| **Region** | **Void %** | **Sphericity** | **Avg. Size** | **Max. Fiber Length** |
|---|---|---|---|---|
| IV | 9.3 % | 0.67 | 1 $\mu$m | 150 $\mu$m |
| V | 2.4% | 0.88 | 0.68 $\mu$m | 54 $\mu$m |

Particles in region V have further refined size and greater sphericity compared to those in region IV as depicted in table 6.2. The average particle size in region V is 68% of that in region IV. Of important consideration, though, is that these cross section measurements do not account for fiber orientation and long particles angled towards the weld path direction will appear small. The maximum observed particle lengths in region V are approximately one third of those in region IV, indicating significant reduction in particle size. The particle refinement in region V results from contact with the threaded tool pin. Greater complexity in the tool pin, especially in terms of the number of edges, increases particle fragmentation [161]. The pin threads also promote particle mixing in the PAZ [61]. Thus, enhanced particle-particle interaction in region V increases fragmentation.

From equation 6.1 the critical fiber length $L_c$ is estimated to be 81$\mu$m, where $\sigma_{Fb} = 3530$ MPa [165], $d_f = 7$ $\mu$m (measured from the fiber diameter in figure 6.5), and $\tau_b = 152$ MPa [166]. These results suggest that the longer fibers in zone IV provide greater reinforcement than zone V.

Figure 6.4 shows an asymmetry between the weld advancing side (AS) and retreating side (RS). In this instance, the RS presents a hooking effect around fiber clusters along region III, resulting in region III having approximately a 20% longer interface from weld center to the weld surface than region II. The weld asymmetry results from greater stresses on the AS than the RS, contributing to higher temperatures [7, 17]. The higher temperatures on the AS in turn lead to greater polymer mobility [68] and allows for improved sweeping of carbon fibers along the weld zone interface.

The weld shown in figure 6.4 has the greatest ultimate strength of all tested parameter combinations, which is further discussed in section 6.3.3 *Mechanical Properties*. However, microscopic images reveal substantial defects and voids in the polymer matrix that vary in size and prevalence depending on the location in the weld. Voids in the matrix occur from poor matrix mobility due to insufficient heating [163] and uneven cooling rates [167]. Figure 6.7 shows a large void that occurs along region II. A fiber cluster frozen in the solid base material has partially exposed ends in the SAZ. Material flow in the SAZ induces tugging on the exposed fibers, but low temperatures prohibit the polymer and chopped fibers from replacing the displaced fiber cluster.

Large voids are especially common along region III which is characteristic of the RS in polymer FSW. These voids develop due to lower processing temperatures and lack of swept material forging around the back

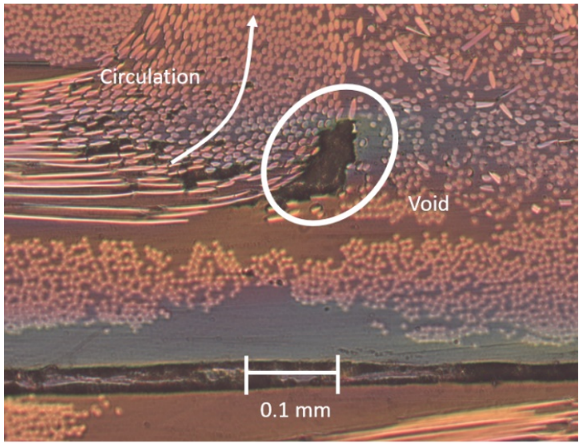

Figure 6.7: Large void visible along the AS from fiber tugging.

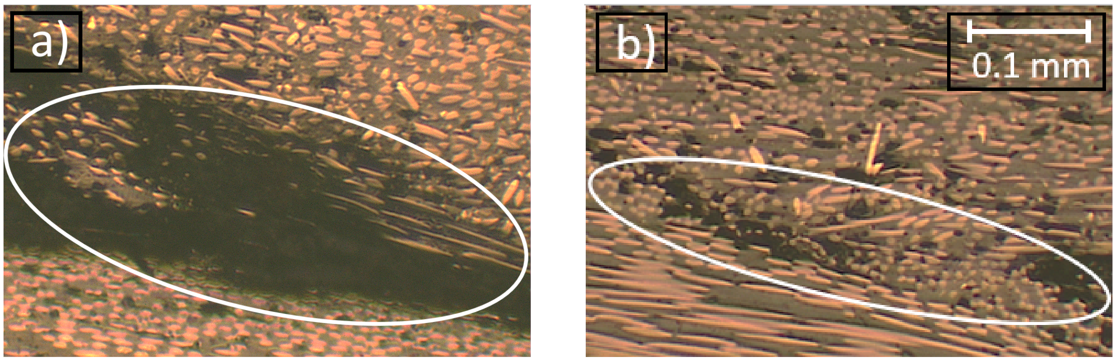

Figure 6.8: Fracture initiation locations. Scale bar applies for both sub figures. a) 600 RPM, 50.8 mm/min weld b) 1000 RPM, 30.5 mm/min weld

of the tool compared to the AS [9]. Tool rotation and traverse speeds have pronounced contribution to the prevalence of voids along region III. Figure 6.8 compares region III defects between two sets of parameters. Figure 6.8a demonstrates a cold weld fabricated using the lowest tested rotation speed and fastest traverse speed. It is well understood that the rotation speed affects heat input, while the traverse speed dictates the thickness of heat diffusion [67, 68]. Thus, too fast of a traverse speed outpaces the thermal conductivity of the composite, resulting in enhanced void formation. Figure 6.8b shows the same region fabricated from a faster rotation speed and slower traverse speed, allowing for more bulk melting and consequently a reduction in void size [68]. The void locations shown in figure 6.8 correspond to the fracture location described in section 6.3.3.1 *Fracture Surface*, indicating these defects are the main source of joint failure initiation.

Microvoid content typically increases with material depth during polymer FSW with shouldered tools due to the inverse relationship between processing temperatures and weld depth that promotes less polymer mobility [67, 68]. However, figure 6.9 shows a conflicting trend compared to those typically observed in polymer FSW. White highlights improve the void visibility for the reader. Region IV (figure 6.9a) has a 9.3%

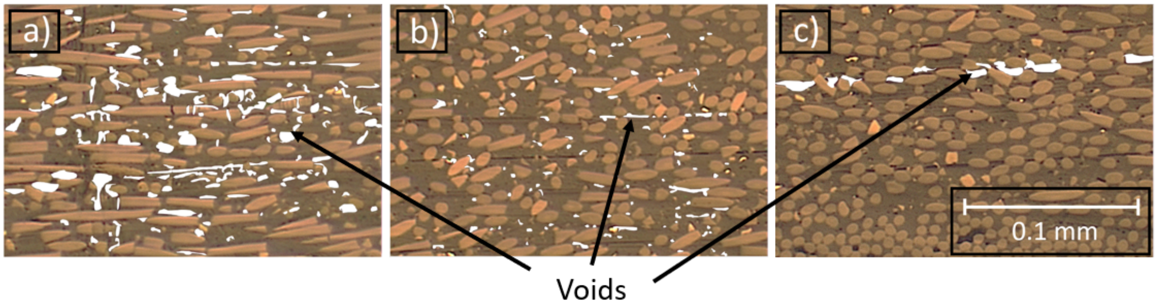

Figure 6.9: a) Region IV (void content 9% b) Region V (void content 2%) c) Bottom of stir zone. Void regions are artificially colored with white overlays to highlight them. Scale bar applies for all three subfigures.

void content, while region V (figure 6.9b) has a 2.4% void content. The discrepancy in void distribution compared to conventional polymer FSW is the advent of variable fiber size fabricated by in-situ processing. Reduction in fiber size increases particle sphericity. Typically, processing of particles with greater sphericity results in a lower fraction of voids in a composite since the flowing polymer can more easily displace voids and encapsulate particles [168]. Thus, higher average particle sphericity in region V contributes to the lower void fraction.

Figure 6.9c shows a trend common to conventional polymer FSW and polymer composite FSW with a lack of material consolidation at the bottom of the PAZ. This region has the coolest processing temperatures, limiting bulk material melting between the PAZ and ultimately limiting interdiffusion across the interface [67].

### 6.3.3 Mechanical Properties

#### 6.3.3.1 Fracture Surface

All specimens failed under stress via tensile fracture along the RS, shown in figure 6.10. This region is essentially an SCF composite bridging the continuous fiber laminate and the cross-sheet boundary region. Since the disruption of fibers inherently weakens the laminate, this region is the weakest on a lapped carbon fiber FSW joint non-exclusive to the advancing or retreating side configuration. Therefore, the joint tensile strength with the sheet thickness used in this study depends on the integrity of the weld in the top sheet rather than the shear strength between the lapped sheets.

#### 6.3.3.2 Tensile Load

Table 6.3 summarizes the results from mechanical testing. **Run** refers to a specific combination between parameters **A** (rotation speed) and **B** (traverse speed). **UTS** and $\boldsymbol{\sigma}$ report the effective average ultimate tensile strength and standard deviation from each set of parameters based on the base material sheet thickness of 1.2

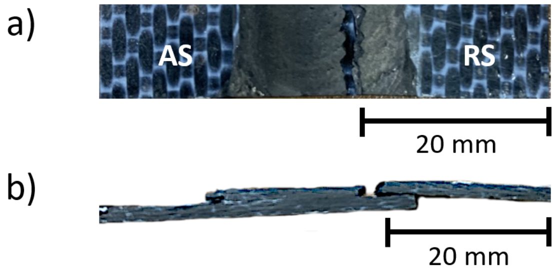

Figure 6.10: a) Top view of fractured specimen. b) Cross section of fractured specimen.

Table 6.3: Average UTS and weld thickness adjusted UTS for each welding parameter combination along with their respective standard deviations $\sigma$. Units for for UTS and $\sigma$ are MPa.

| **Run** | **A** (RPM) | **B** (mm/min) | **UTS** (MPa) | $\boldsymbol{\sigma}$ | **UTS** (adj.) (MPa) | $\boldsymbol{\sigma}$ (adj.) |
|---|---|---|---|---|---|---|
| **1** | 600 | 10.2 | 33.0 | 2.0 | 41.8 | 3.1 |
| **2** | 600 | 30.5 | 40.1 | 0.1 | 45.5 | 0.1 |
| **3** | 600 | 50.8 | 34.7 | 1.8 | 41.4 | 4.3 |
| **4** | 800 | 10.2 | 33.4 | 8.8 | 39.9 | 10.1 |
| **5** | 800 | 30.5 | 41.5 | 6.4 | 48.9 | 9.3 |
| **6** | 800 | 50.8 | 45.6 | 9.3 | 52.8 | 11.3 |
| **7** | 1000 | 10.2 | 46.5 | 4.3 | 57.6 | 6.0 |
| **8** | 1000 | 30.5 | 56.0 | 10.4 | 73.8 | 10.3 |
| **9** | 1000 | 50.8 | 39.8 | 7.8 | 49.0 | 13.2 |
| **10** | 1400 | 10.2 | 35.6 | 3.4 | 45.0 | 8.3 |
| **11** | 1400 | 30.5 | 52.4 | 16.2 | 56.7 | 17.3 |
| **12** | 1400 | 50.8 | 39.2 | 6.0 | 46.0 | 7.4 |
| **13** | 1800 | 10.2 | 36.5 | 7.4 | 39.7 | 5.8 |
| **14** | 1800 | 30.5 | 37.4 | 6.0 | 39.0 | 6.2 |
| **15** | 1800 | 50.8 | 39.2 | 3.7 | 46.0 | 1.8 |

mm. FSW thins the materials in the weld zone when implementing a rotating shoulder, ultimately reducing the load bearing cross section. Therefore, **UTS** (adj.) and $\boldsymbol{\sigma}$ (adj.) consider reduced material thickness at the fracture location to better represent the weld zone's strength. To make thickness adjustments, the material thickness was measured in unstressed weld specimens. The measurement location was mapped from the fracture location in each weld's respective tensile specimens.

Parameters A and B have quadratic effects on the ultimate tensile strength, making the necessity of testing a minimum of three parameter levels apparent. Figure 6.11 plots the average effects of each parameter on UTS and figure 6.12 does similarly for UTS adjusted.

The three originally tested tool rotation speeds did not produce quadratic effects on the UTS as hypothesized. 600 RPM and 800 RPM runs added curvature to the mean effects on UTS, placing 1000 RPM at the maxima. These results differ from those in a similar study [163], but the rotating shoulder in this work generates more heat at lower RPM's.

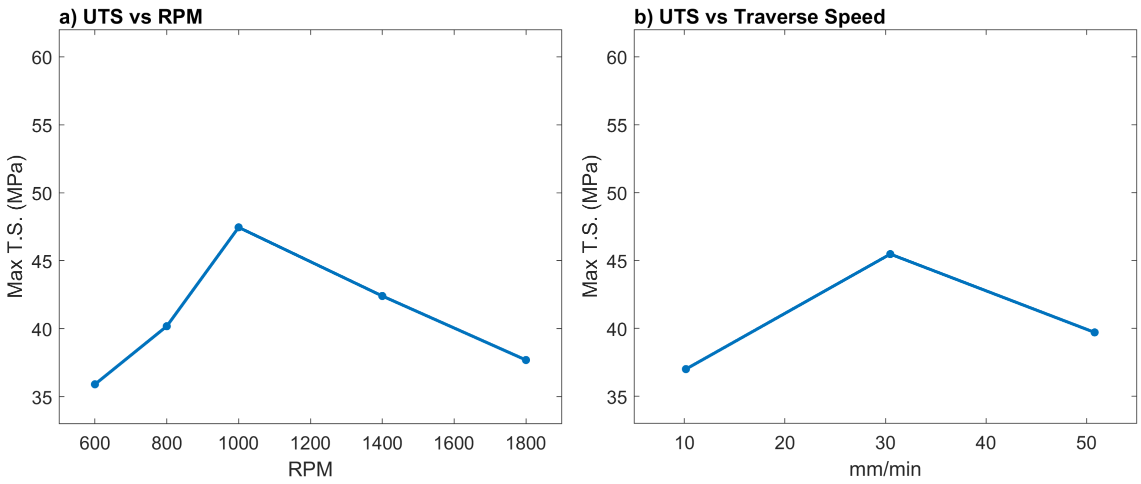

Figure 6.11: Fitted mean effects on the effective ultimate tensile strength from a) rotation speed and b) traverse speed.

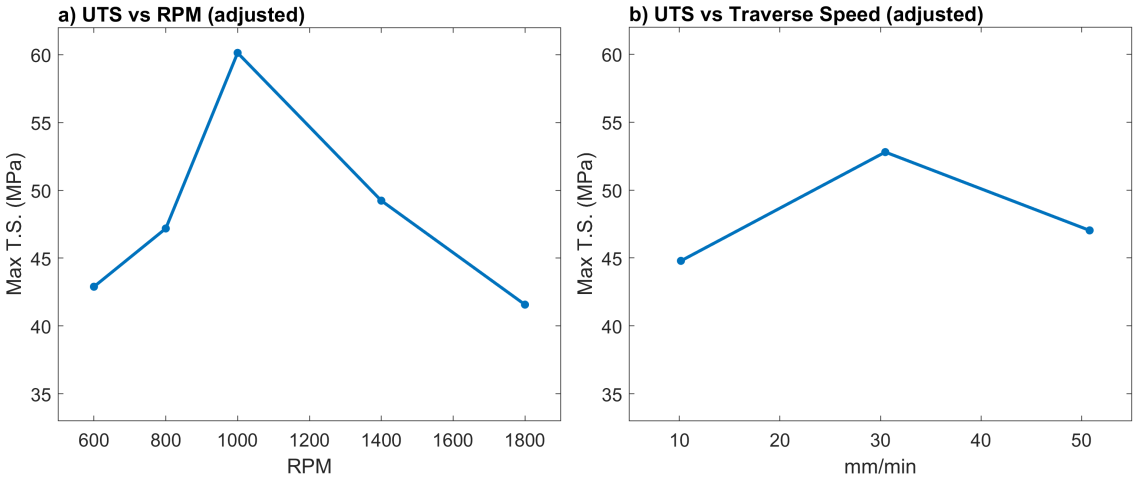

Figure 6.12: Fitted mean effects on the thickness adjusted ultimate tensile strength from a) rotation speed and b) traverse speed.

Weld parameters of 1000 RPM and 30.5 mm/min consistently formed the strongest joints with 56.0 MPa average effective UTS and 73.8 MPa average thickness adjusted UTS. Tool rotation and traverse speeds often produce the greatest contribution to weld strength in polymer FSW [83] due to their influence on thermal input, mechanical interaction, and and material consolidation. 600 RPM and 800 RPM rotation speeds lacked sufficient thermal input from friction and plastic deformation to promote polymer diffusion across zones II and III. 1400 RPM and 1800 RPM rotation speeds have greatly accelerated work piece velocities that promote excessive void formation and material expulsion. A 1000 RPM rotation speed provided sufficient thermal input without overly agitating the weld pool. Likewise, the traverse speeds influence curved behavior on the UTS. A low pressure zone follows the tool during FSW, which can limit polymer adhesion in the weld zone with fast traverse speeds [123]. Slow traverse speeds allows for more contact time between the molten polymer pool and joining surfaces. However, traverse speeds also influence the amount of thermomechanical stress, and it has been shown that a faster traverse speed can use the enhanced thermomechanical stress to further distribute particles in composites [127]. Therefore, it appears that the 30.5 mm/min traverse speed balances the effects of thermomechanical stress induced particle distribution and polymer weld pool contact time.

The tensile data presented considerable variation between replicate welds and between replicate tensile specimens within the same weld. Runs 8 and 11 had the greatest non-adjusted variation with standard deviations of 10.4 MPa and 16.2 MPa, respectively. Runs 8 and 11 also had the two highest non-adjusted average tensile strengths at 56.0 MPa and 52.4 MPa but had tensile specimens with strengths of up to 68.0 MPa and 80.2 MPa, respectively. Adjusted UTS values contributed to additional variation within parameter sets since the small tensile cross sections have high sensitivity to calculations. There was no correlation to the tensile specimen strength with respect to its location along a weld. In other words, tensile specimens cut closer to the initial weld plunge did not have consistently higher tensile strengths than specimens cut further from the initial plunge. CFRTP's inherently present variations in mechanical performance due to their non-homogeneous structure. Mentioned in section *Microscructure*, the woven structure greatly affects the composite morphology in the weld zone and contributes to highly localized mechanical characteristics. Since weld specimens were cut from a larger laminate sheet, the fiber sequence at the edge of each cut specimen is unique and affects the alignment of fiber clusters for each weld. Runs with large $\sigma$ likely have instances where the fiber clusters local to the weld promote exemplary strength. 600 RPM and 1800 RPM welds have the least variability, though they have fewer replicate runs since it was clear early in the experimentation that the optimal welding parameters laid somewhere in between them.

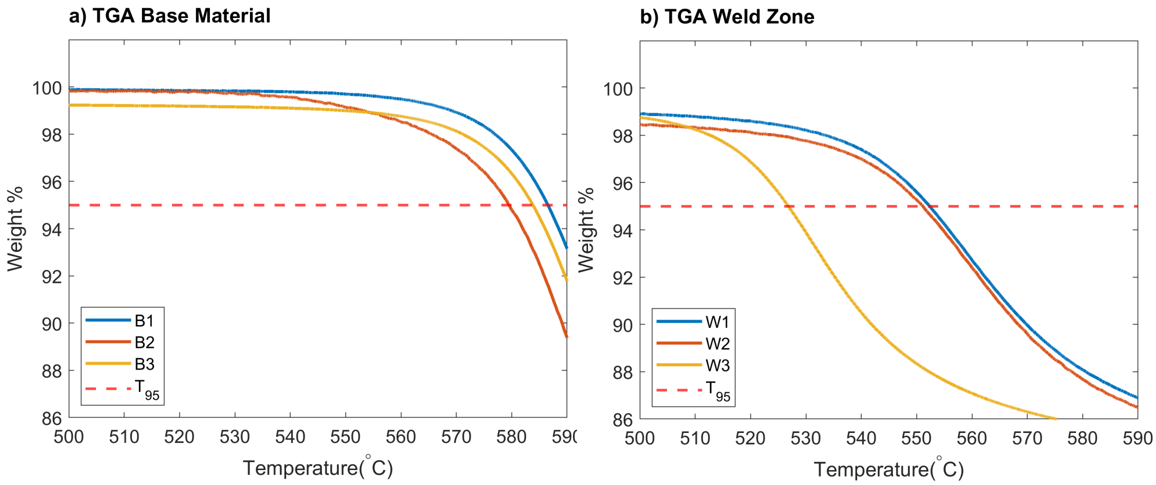

Figure 6.13: TGA curves for a) base carbon fiber laminate and b) 1000 RPM, 30.5 mm/min weld zones.

Table 6.4: $T_{95}$ values for base material and weld zones.

| **Base Specimen** | $T_{95}$ (°C) | **Weld Specimen** | $T_{95}$ (°C) |
|---|---|---|---|
| B1 | 579.5 | W1 | 526.6 |
| B2 | 583.8 | W2 | 551.2 |
| B3 | 586.5 | W3 | 552.3 |
| **Average** | **583.3** | **Average** | **543.4** |

### 6.3.4 Thermal Properties

#### 6.3.4.1 Thermogravimetric Analysis

Figure 6.13 shows thermogravimetric analysis (TGA) curves for the base carbon fiber laminate and the weld zones of 1000 RPM, 30.5 mm/min specimens. The base material runs are denoted as B1, B2, and B3. The welded material runs are denoted as W1, W2, and W3. $T_{95}$ refers to the temperature with 5% weight loss. Table 6.4 reports the $T_{95}$ values for each TGA run. The base material has an average $T_{95}$ of 583.3°C while welded specimens have an average $T_{95}$ of 543.4°C.

The lower thermal stability in welded specimens is a result of the short fiber length in the weld zone. The addition of carbon fiber into a polymer matrix increases the overall absorption capacity of the composite, and longer fibers allow the composite to withstand greater temperatures since they absorb more heat [169]. Highly localized temperatures around the tool/composite interface may also contribute to slight reduction in thermal stability, but the low thermal conductivity further limits widespread thermal degradation throughout the weld. Confirmation of decreased thermal stability due to overheating of the polymer requires the capability to accurately measure the temperature at the interface between the tool and polymer during welding.

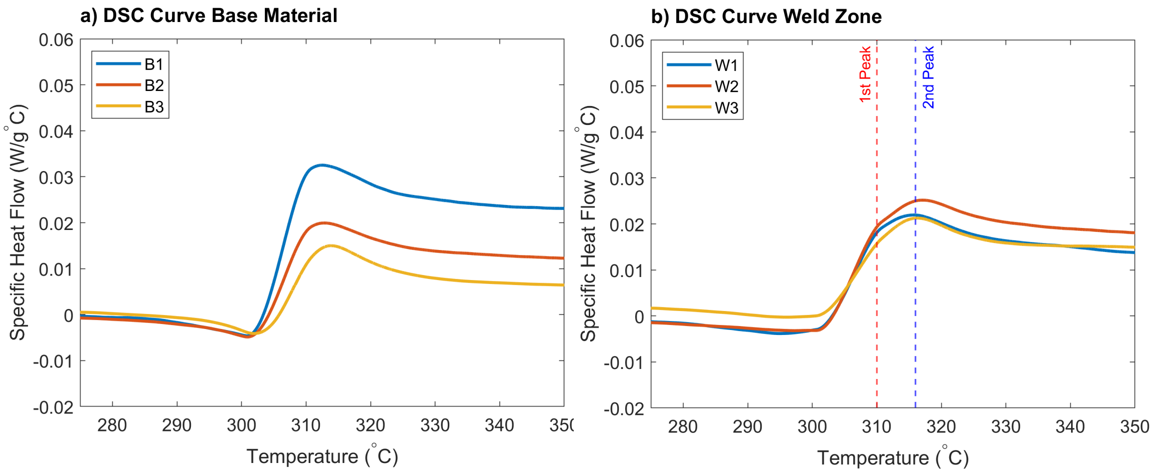

Figure 6.14: DSC curves for a) base carbon fiber laminate and b) weld zones of 1000 RPM, 30.5 mm/min specimens. Endothermic curves point upwards.

Table 6.5: Summary of DSC results. B1, B2, B3 refer to base specimens. W1, W2, W3 refer to specimens from 1000 RPM, 30.5 mm/min welds.

| **Base Specimen** | $T_{onset}$ (°C) | $T_m$ (°C) | **Weld Specimen** | $T_{onset}$ (°C) | $T_{m1}$ (°C) | $T_{m2}$ (°C) |
|---|---|---|---|---|---|---|
| B1 | 303.3 | 312.6 | W1 | 302.6 | 310.6 | 315.9 |
| B2 | 303.3 | 312.9 | W2 | 302.6 | 309.9 | 316.3 |
| B3 | 305.6 | 312.0 | W3 | 302.5 | 310.6 | 317.0 |
| **Average** | **304.1** | **312.5** | **Average** | **302.6** | **310.4** | 316.4 |

#### 6.3.4.2 Differential Scanning Calorimetry

Figure 6.14 shows the differential scanning calorimetry (DSC) melting endotherms obtained for specimens while undergoing TGA, as the TA Instruments Q600 SDT performs these measurements simultaneously. Table 6.5 summarizes the DSC results. Toray reports the melting temperature for the base composite to be 305°C [166]. The onset melt temperatures ($T_{onset}$) for both the base material and weld zones are in good agreement with the manufacturer's reported melting temperature. The average peak melting temperature $T_m$ for the base laminate material is 312.5°C, reported in table 6.5. Specimens cut from weld zones exhibit a broader melting curve with two inflection points indicating two peaks. The double-melting behavior results from reorganization of the crystal structure as the temperature increases [170]. The chopped fibers in the weld zone improve chain mobility and allow for this double-melting behavior.

### 6.3.5 Welder Inputs

#### 6.3.5.1 Welding Forces

The rotation and traverse speeds have statistically significant contribution to the average axial and lateral welding forces during the weld traversing period, with a greater contribution from the rotation speed in both

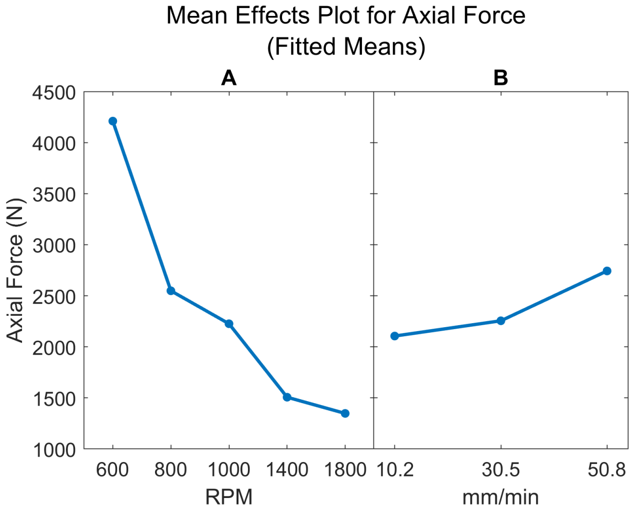

Figure 6.15: Fitted mean effects for tool rotation speed (A) and traverse speed (B) on axial force.

cases. Only the rotation speed has statistically significant contribution to traverse forces, and there does not appear to be interaction effects between the two parameters. Table 6.6 displays the average axial, lateral, and traverse forces measured by the dynamometer during weld traverse periods. Generally, faster tool rotation speeds reduce all forces due to its improved heat generation. Figure 6.15 shows the average axial force response for each respective parameter, illustrating rotation speed's greater contribution from the steeper slope. The axial forces range from approximately 900 N-4700 N during the weld traversing period, whereas the traverse and lateral forces are significantly less by an order of magnitude. Figure 6.16 shows the effect of tool rotation speed on traverse force. The rotation speeds reduce in magnitude between 600 RPM and 1000 RPM due to improved material softening on the leading edge of the tool. At 1400 RPM and 1800 RPM, the traverse forces measured at the spindle slightly dominate towards the welding direction. The positive measured traverse forces are attributed to the resultant component of axial force induced by the rearward tool tilt. For welds producing the optimal tensile strengths with 1000 RPM, 30.5 mm/min parameters, the required forces during the traversing period for the tool used in this study are approximately 2200 N in the axial direction and 190 N in planar directions. Thus, the tool forces during FSW of laminate sheets are on the order of polymer FSW in comparison to metal FSW [70, 103, 120].

#### 6.3.5.2 Power Consumption

Equation 6.2 calculates the power consumption by the tool during welding:

$$P = \omega \times \tau \tag{6.2}$$

Table 6.6: Average welding forces during traverse period for each parameter combination. A and B refer to rotation speed and traverse speed, respectively. All forces are reported in Newtons (N).

| A | B | Axial | Lateral | Traverse |
|---|---|---|---|---|
| 600 | 10.2 | 3543 | 233 | -207 |
| 600 | 30.5 | 4345 | 377 | -330 |
| 600 | 50.8 | 4742 | 458 | -351 |
| 800 | 10.2 | 2348 | 220 | -82 |
| 800 | 30.5 | 2490 | 310 | -139 |
| 800 | 50.8 | 2808 | 387 | -182 |
| 1000 | 10.2 | 1844 | 154 | -32 |
| 1000 | 30.5 | 2222 | 186 | -42 |
| 1000 | 50.8 | 2612 | 247 | -20 |
| 1400 | 10.2 | 1344 | 51 | 81 |
| 1400 | 30.5 | 1290 | 152 | 117 |
| 1400 | 50.8 | 1886 | 83 | 83 |
| 1800 | 10.2 | 1449 | 7 | 81 |
| 1800 | 30.5 | 928 | -9 | 73 |
| 1800 | 50.8 | 1667 | 21 | 23 |

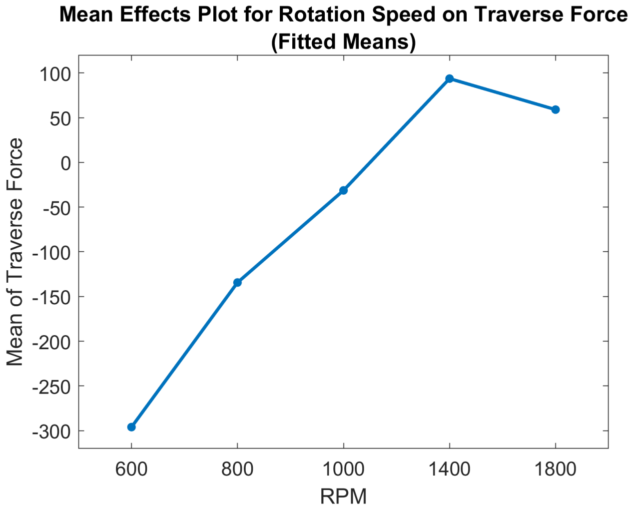

Figure 6.16: Fitted mean effects for tool rotation speed on traverse force.

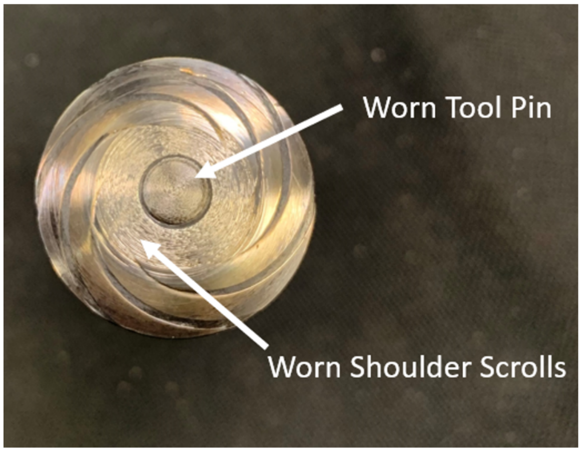

Figure 6.17: Worn tool shoulder and pin from carbon fiber abrasion.

where $\omega$ is the tool spindle angular velocity and $\tau$ is the spindle torque measured by the dynamometer. Calculating the power from the spindle torque eliminates mechanical losses from the welder and gives a pure power input to the weld piece. Strong correlations were not present between the welding parameter values and spindle torque. It is hypothesized that small carbon fiber particles act as a lubricant under the tool shoulder and limit spindle torque. Any correlations in torque between parameter inputs are within the baseline signal noise. The average power across all parameter combinations is 98.2 W during the traversing period. For the 1000 RPM, 30.5 mm/min welds, the average processing power was 67.4 W, making FSW an energy efficient method to join composites. Of course, the actual value is higher when considering the total power to run the machine from on board control systems and mechanical losses.

### 6.3.6 Discussion

Until now, extensive study pertaining to FSW of CFRTP laminate sheets have yet to be explored. The feasibility and applicability of this process over other joining methods depends on joint strength, processing time, joint configuration, and tooling requirements. Processing of CFRTP inherently has challenges due to its non-homogenous structure. FSW of carbon fiber laminate sheets has complexity due to the disruption of carbon fibers in the weld zone and poor through-sheet thermal conductivity. This study shows promising results with instances of high strength, but also clear indications of improvements needing attention.

Some tool wear was evident throughout the course of the study, shown in figure 6.17. Tool wear influence likely has little significance on studied parameter effects contributing to weld strength in this study, as the order of blocked welding replicates were randomized. However, tools in large volume production of CFRTP FSW joints should be constructed of materials with higher abrasion resilience such as A11 tool steel [160].

It is imperative to recognize the mode of fracture in this study. Carbon fiber laminates obtain their high specific strength from continuous carbon fibers, and any disruption or discontinuity along a fiber length requires the polymer matrix to distribute loads to other fibers, inherently providing weaker mechanical properties over continuous fibers. Thus, even welding methods that do not disrupt the fibers in the adjoining sheets are limited to the shear strength of the polymer matrix if the fibers do not cross he joint interface. Reported UTS values for the base laminate TC1225 woven sheet are 805 MPa in the 0° direction and 739 MPa in the 90° direction [166]. These strength values are vastly superior to the 73.8 MPa UTS observed in this study's FSW joints. However, discontinuity and chopped carbon fiber in the joint requires joint comparison to the UTS of a polymer reinforced with SCF's. Existence of studies reporting the mechanical properties of LMPAEK reinforced with SCF are unknown to the authors at this time. However, LMPAEK and PEEK have similar mechanical strength, shown in table 6.7. Tensile strengths for injection molded SCF/PEEK composites range between 152.5 MPa and 211.9 MPa, though the higher strengths result from alignment of fibers in the tensile direction at the edge of the mold [164]. Thus, the optimal FSW parameters in this study produce joints with approximately 50% joint efficiency in relation to a comparable SCF composite that has variable fiber orientation. The low joint strength in the reinforced composite weld compared to the neat polymer results from sub-critical fiber lengths [162] and favored fiber orientation to the weld zone walls [161]. Ultimately, matrix porosity in the weld zone likely has the greatest contribution to detrimental weld performance. Future study to further optimize joint strength in friction stir welded CFRTP laminates requires consideration of avenues for both higher processing temperatures and retainment of fiber length. Auxilliary heating such as heated tools [72], hot shoes at the weld surface [127], and heat sources below the welding materials [67] are likely to improve processing temperatures and reduce porostiy. Optimizing fiber length may be accomplished with studies in the tool geometry, though balancing fiber size with trade-offs in matrix porosity may be especially challenging unless significantly improved processing temperatures counteract low mobility around longer fibers.

Though complications persist for carbon fiber laminate FSW, there are several attributes that may qualify it as an attractive process to join CFRTP laminates in the future. Since the fracture mode for thin sheets in CFRTP laminate FSW is purely tensile in the top sheet, structural strength can be further improved by increasing the thickness of the top adjoining sheet. Whether or not the load bearing capacity of friction stir welded laminate sheets scales linearly with top sheet thickness is reserved for future study. The lap shear strength between the weld zone and bottom sheet is also a mechanical feature to consider when increasing the top sheet thickness since excessive thickening of the top sheet may encroach on the lap shear load bearing capacity.

CFRTP laminate FSW has an advantage over ultrasonic welding since it does not require integration of energy directors that makes consistent continuous welds and in-situ monitoring challenging tasks to achieve

Table 6.7: Comparison of PAEK tensile properties.

| **Reinforcement Type** | **UTS** | **Reference** |
|---|---|---|
| Neat LMPAEK | 95 MPa | [171] |
| Neat PEEK | 97.2 MPa | [171] |
| FSW LMPAEK Weld Zone | 73.8 MPa | Current Study |
| SCF PEEK | 152.5-211.9 MPa | [164] |
| LMPAEK Laminate 42% RC, 0° | 805 MPa | [166] |
| LMPAEK Laminate 42% RC,90° | 739 MPa | [166] |

[172]. Further, FSW does not use consumables such as gas in hot gas welding, and does not leave embedded wires such as those in resistive welding. A drawback to FSW in CFRTP joints is the welding speed. Continuous ultrasonic welders can join CFRTP on the order of several meters per minute [173], while FSW traverses on the order of several centimeters per minute. However, the simplicity of FSW improves the overall process efficiency when considering material preparation and post-weld processing [53]. Current FSW equipment designed to join metal alloys used in components such as rocket fuel tanks and pressure vessels can be easily adapted to weld newer composite versions of these components since metal and polymeric FSW share the same basic tooling principles. Thus, improvements in future study of continuous CFRTP FSW will make it a viable and competitive process in the manufacture of composite structures.

### 6.4 Conclusions

This work uses FSW to join LMPAEK CFRTP laminate sheets in lap joint configuration. Joining two laminate carbon fiber sheets via FSW has novelty in the field and presents challenges since it requires disruption of the woven fibers in the laminate. A parameter study was conducted to determine the effects of tool rotation speed and traverse speed on weld integrity. The results indicate the following:

- Fiber disruption in the weld zone forms distinct zones with variable fiber size and orientation.
- Parameters of 1000 RPM rotation speed and 30.5 mm/min traverse speed produce tensile strengths of 73.8 MPa, which is approximately 50% the strength of a comparable short carbon fiber reinforced composite.
- Weld porosity appears to have the greatest influence on strength reduction, with failure initiating defects located along the base material/weld zone interface.
- Thermal analysis shows slightly reduced thermal stability in the weld zone at high temperatures due to

greater polymer mobility for discontinuous fibers with thermal degradation occurring at approximately 40°C cooler temperatures than the base laminate material.

- Optimized welding parameters require 2200 N of axial force and 67.4 W of power during traversing periods requiring lower machine requirements than FSW of metal alloys.

Advancements in aerospace technology requires increased used of high-performance materials and solutions to join them that better harness their capabilities in space systems. Though pre-existing welding methods exist to join CFRTP laminates, FSW offers additional versatility and competitive joint strengths to other joining methods.

# CHAPTER 7

## Post-weld Annealing of Friction Stir Welded Carbon Fiber Reinforced Low-melt Polyaryletherketone

The following work was previously published in the *Journal of Composite Materials* as:

L. T. Wilkins, A.M. Strauss, Post-weld Annealing of Friction Stir Welded Carbon Fiber Reinforced Low-melt Polyaryletherketone, *Journal of Composite Materials*. November 2023;

### Abstract

This study explores the influence of post-weld annealing on friction stir welded (FSW) carbon fiber reinforced thermoplastic (CFRTP) in woven laminate form. Field advancement occurs in three key areas including furthering the understanding low-melt polyaryletherketone (LMPAEK) welding/processing, effects of post-weld annealing on CFRTP joints, and determining feasibility for friction stir welding of thermoplastics reinforced with continuous carbon fibers. High temperature annealing just below LMPAEK's melting point improved ultimate tensile strength by up to 30% and weld toughness by up to 91%. Improvements to mechanical performance result from increases in joint crystalline content from 14.09% in non-annealed joints to 27.91% in joints subject to 280°C annealing. Annealing does not reduce porosity in the weld zones, rendering necessary further improvements to the FSW process for CFRTP joints. Further analysis also indicates that despite its slight molecular modifications, LMPAEK has highly similar crystalline structure and response to thermal treatment compared to PEEK.

### 7.1 Introduction

Carbon fiber reinforced thermoplastics (CFRTP) are gaining popularity in aerospace sectors as a replacement for epoxy based composites due to their ability to be thermoformed, high impact resistance, and potential for recycling. Their thermoformability also allows for welded joints, reducing added weight from mechanical fasteners and limiting stress concentrations. Welded CFRTP joints are already used in industry. The following examples highlight industry applications that implement CFRTP welding [174]. GKN Fokker used induction welding to join elevator and rudder components on the Gulfstream G650 and Dassault Falcon 5X aircraft. They also used ultasonic welding to join parts to CFRTP floors in the G650. The airbus A340, A350, and A380 aircraft have resistance welded wing leading edges. Recently, researchers applied friction stir welding (FSW) as an alternative joining method to weld CFRTP. FSW was patented by Wayne Thomas et al. of the Welding Institute on December 6, 1991 as a novel process to join metal alloys [44]. The first available documentation on polymer FSW became available in the late 1990's [12] and a significant portion of the research occurred within the last decade, expanding to polymer composites.

Most studies concerning CFRTP FSW join thermoplastics reinforced with short carbon fibers (SCF) [153, 160, 163, 175, 176, 177]. Many large structures such as fuselages and propellant tanks utilize continuous carbon fibers (CF) in their reinforcement. Many stamp formed components, such as mounting/support clips on the Airbus A350, utilize woven fabric reinforced laminates of just several layers from thin sheets [178]. Therefore, studies where FSW joins composites reinforced with continuous fibers are necessary to make FSW a potential competitive joining technology in future aerospace composite structures. The first known study to consider FSW of thermoplastics reinforced with continuous CF's occurred recently. Wilkins et al. demonstrated friction stir welded lap joints of woven carbon fiber reinforced low-melt polyaryletherketone (LMPAEK) laminate which differs from traditional CFRTP welding methods in that the fibers are disturbed in the weld zone. They achieved approximately a 50% joint efficiency when comparing the FSW joint to a short carbon fiber reinforced thermoplastic (SCFTP). [179].

The rapid heating and cooling cycles presents challenges when welding thermoplastics. Thermoplastic welding involves interdiffusion and entanglement of molecular chains to connect two or more components [122]. Welding requires melting of the polymer at the joint interface and pressing the joining components together for them to consolidate upon solidification [180]. This process creates a cycle of chain disentanglement and re-entanglement [122].

Temperatures above the polymer's glass transition temperature ($T_g$) relaxes the molecular chains, allowing for them to slide past each other and diffuse across the joint. The amount and rate of molecular diffusion depends on the temperature and amount of time of time at said temperature [6]. For semi-crystalline polymers, rate of cooling from the melt affects not only polymer diffusion but degree of crystallinity as well. Ultimately, these elements affect mechanical performance. Higher degrees of crystallinity associate with increased modulus, shear strength, interfacial strength, and chemical resistance in CFRTP [25]. The formation of a transcrystalline region, or crystals oriented along the fiber/matrix interface, promotes improved interfacial shear strength between the polymer and fibers [26]. Low crystallinity can be beneficial under circumstances that requires ductility. However, low crystallinity increases permeability in the polymer that allows for diffusion of gases [23].

Rapid cooling rates common to polymer welding techniques can limit chain diffusion and crystallinity. Increasing the processing times during thermoplastic welding to decrease the cooling rate from the melt has been shown to improve crystallinity in ultrasonically welded polyphenylene sulfide (PPS) joints [25]. However, increasing individual joint processing times reduces the overall manufacturing efficiency. Semi-crystalline polymers can crystallize both from the melt and heating from the glass [181]. Crystal types and orientation biases have temperature dependency as nucleation and spherulites form at higher temperatures and rod-like growth occurs near $T_g$ [181]. Crystal growth below the melting temperature ($T_m$) makes post-weld annealing possible, which can improve process times since annealing can commence in large batches.

Most of the CFRTP annealing research focuses on molded and 3D printed parts. Kishore et al. found that post-fabrication annealing of CF reinforced PPS improves the torsional storage modulus as a result of increased crystallinity. They also indicated that annealing promoted crosslinking of polymer at the surface, but these effects were not representative of the bulk material [182]. Handwerker et al. observed a 50% increase in the ultimate tensile strength (UTS) of additively manufactured SCRTP when subjected to annealing. Void formation during the manufacturing process was the highest contributor to tensile failure and was not completely resolved by annealing [183]. Yu et al. found a similar trend in printed CF/PEEK (polyetheretherketone) composites with a 55.4% increase in interlaminar shear strength (ILSS). Annealing reduced porosity in their case, though did not completely remove the voids [184]. Um et al. considered the post annealed temperature dependent mechanical properties of CF/PET (polyethylene terephthalate) composites. In both 25°C and 100°C environments, slowly cooled specimens exhibiting higher crystallinity exhibited greater tensile strength and modulus. They attribute improved fiber/matrix adhesion from transcrystallinity and thermal stability as cause for increased performance [185]. Generally, annealing's role in improved thermoplastic mechanical performance results from bulk crystallization that increases molecular chain order [181]. Improvements from annealing on bulk composites indicates that welded CFRTP joints will reap the benefits as well.

LMPAEK is a recent addition to the PAEK family of polymers. It is nearly identical to PEEK, except that it contains one extra aryl group in approximately 25% of the monomers [5]. As a result, LMPAEK has nearly identical mechanical properties and $T_g$ as PEEK with a reduced $T_m$ which makes it easier to process for injection molding, fiber impregnation, and welding. In addition to its nearly identical mechanical properties to PEEK, LMPAEK has also been shown to have a very similar response to thermal treatment as PEEK despite its slight chemical modification [186]. Schiel et al. studied the effects of process parameters on mechanical properties for CF/LMPAEK tape layup. They found that LMPAEK is less sensitive to layup processing speeds than PPS and PEEK, which allows for faster initial fabrication of components. However, LMPAEK was highly responsive to post-layup tempering. When heated to 290°C for 17 hours, it reached near 30% crystallinity and improved lap shear values by up to 76% [187].

The following work explores the effects of post-weld annealing on friction stir welded LMPAEK reinforced with woven carbon fibers. The heat treating aspect of this research is the next phase to follow previous work studying the feasibility of joining woven CFRTP using FSW and utilizes previously established optimized welding parameters [179]. The manuscript aims to further establish the feasibility of CFRTP FSW and identify key weaknesses to address in future study. The principles of post-weld annealing not only apply to friction stir welded joints, but to all CFRTP welding.

## 7.2 Materials and Methods

### 7.2.1 Joint Fabrication

Toray Advanced C omposites supplied TC1225 woven laminate, with T300 carbon fibers and a polymer matrix composed of low-melt polyaryletherketone (LMPAEK). The laminates are four ply in [(0,90)]2S layup with a 1.2 mm sheet thickness. Specimens were cut to 30 mm × 70 mm and arranged by methods in previous study [179]. FSW commenced on Kearney and Trecker Milwaukee Model K milling machine modified with autonomous computer controlled spindle and axial drives. Joints were assembled in lap joint configuration with the top sheet's lapped edge oriented to the FSW tool's advancing side. The laminate sheets were oriented with the 0° fiber parallel to the weld line and a 15 mm overlap. The lap configuration and fiber orientation is identical to that described and illustrated in previous study [179]. The tool consisted of a 25.4 mm diameter scrolled parabolic shoulder with a 6.35 mm threaded cylindrical pin and 0.79 mm pitch left-hand threads set to 1.143 mm length, shown in figure 7.1. The tool rotated clockwise such that the threaded pin facilitated downward material flow. Welding parameters included 1000 RPM rotation speed, 30.5 mm/min traverse speed, 1.524 mm plunge depth, and 1.5° rearward tool tilt.

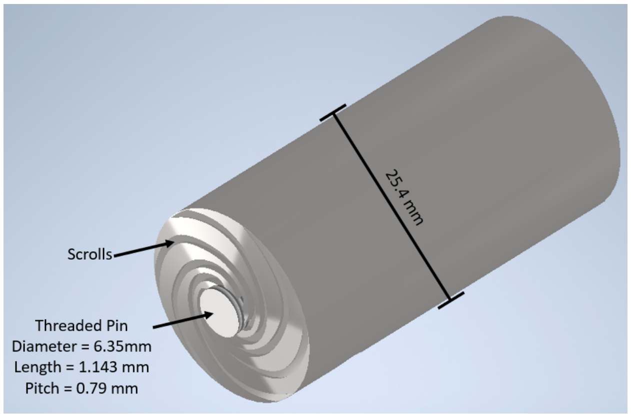

Figure 7.1: FSW tool consisting of threaded pin and scrolled parabolic shoulder.

### 7.2.2 Annealing Procedure

Welds were grouped into three annealing conditions outlined by table 7.1. A1 refers to a non-annealed welded joint, A2 is a low temperature annealed welded joint, and A3 is a high temperature annealed welded joint. Annealing commenced in a programmable tube furnace with a procedure listed in table 7.1 and outlined in the Victrex PEEK processing guidelines [151]. Annealing temperatures were reduced from the processing guidelines for PEEK to account for the lower melting temperature of LMPAEK.

Table 7.1: Annealing procedure

| Condition | Preheat | Ramp Rate | Max. Temp. | Total Time |
|---|---|---|---|---|
| A1 | n/a | n/a | n/a | n/a |
| A2 | 150°C<br>3 hours | 10°C/hour | 200°C<br>4 hours | 17 hours |
| A3 | 150°C<br>3 hours | 10°C/hour | 280°C<br>4 hours | 33 hours |

### 7.2.3 Analysis

#### 7.2.3.1 Imaging

Weld cross sections were polished down to 0.05 $\mu$m with alumina slurry. Polished cross sections were subjected to permanganic etching following the procedure outlined in Olley et al. [188]. The procedure was modified by using a magnetic stirrer to agitate the etchant on submerged specimens rather than a bottle shaker. The etched cross sections were viewed under an optical microscope and an FEI FEG Quanta 650 environmental scanning electron microscope (ESEM). Tensile fracture surfaces were also viewed in the ESEM. ESEM parameters include 10 Pa chamber pressure, 10.00 kV electron beam, and 3.0 spot size.

#### 7.2.3.2 Thermal Analysis

A TA Instruments Q600 SDT simultaneously performed thermogravimetric analysis (TGA) and differential scanning calorimetry (DSC). TGA weight calibration and DSC heat flow calibration preceded experiment runs. Specimens approximately 5 mm in diameter were cut from the weld zone, allowing for precise selection of material to be used in TGA/DSC runs. Figure 7.2 shows the location of test specimens with respect to the weld piece. Nitrogen gas purged the specimens in the furnace with a flow rate of 50 mL/min. The temperature was increased at 10 °C/min with a final temperature of 900 °C. This final temperature was chosen since additional weight loss has been shown to cease at 900 °C in similar PEEK polymers [189]. The final weight was used to calculate the weight % CF. Though Toray publishes a CF weight fraction in their composite [166], highly localized DSC specimens cannot guarantee the published values.

#### 7.2.3.3 X-ray Diffraction

X-ray diffraction (XRD) was performed using a Rigaku Smart Lab powder XRD with a Cu $K_\alpha$ source. Runs swept $2\theta$ from 10°-50° on the weld surface of each annealing condition. An XRD run was also performed on a neat laminate specimen. XRD curves were analyzed using LIPRAS (Line Profile Analysis Software) [190].

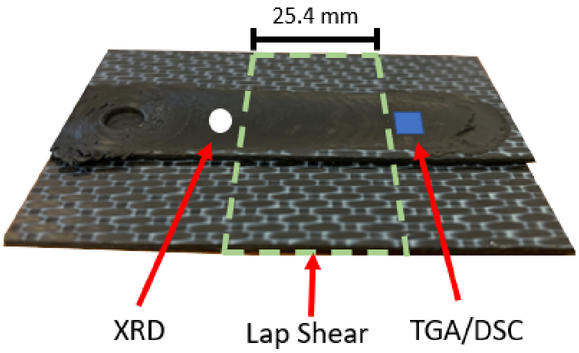

Figure 7.2: Specimen locations for XRD, thermal analysis, and mechanical testing.

Diffraction peaks were fitted using Pseudo-Voigt profile functions. Crystallite size was calculated using the Scherrer Equation:

$$D = \frac{k\lambda}{\beta cos(\theta)} \tag{7.1}$$

k is a correction factor (0.9 is sufficient [25]), $\lambda$ is the wavelength (1.5418 $\AA$ for Cu $K_\alpha$ X-ray source), $\beta$ is the full-width at half maximum (FWHM), and $\theta$ is the Bragg angle.

#### 7.2.3.4 Mechanical Testing

Mechanical testing consisted of single lap shear tests on an Instron load frame. 25.4 mm wide tensile specimens were cut at a minimum of 16 mm from the weld's beginning location. CF pads adhered with abrasive paper accounted for the lapped material offset in the load frame's jaws. All welds were pulled at 2 mm/min until failure. Nine single lap shear specimens were tested for each annealing condition.

## 7.3 Results and Discussion

### 7.3.1 Visual Analysis

All welds resemble the surface appearance observed in previous study [179]. Previous work using FSW to join CFRTP woven laminates states that refined fibers in the weld zone tend to orient along boundaries and have variable sizes dependent on their location [179]. These observations do make assumptions since the true fiber size and orientation is shielded by surrounding matrix. For example, a fiber cut on an angle may appear as an oblong particle in a polished cross section. Figure 7.3 shows a weld cross section prior to and after permanganic etching under an optical microscope. The etching removes some of the polymer at the surface without disrupting the fibers to partially expose them. Polarized light aids in distinguishing between the polymer and matrix. In figure 7.3b, speckled regions in the weld zone surround dark regions. The small

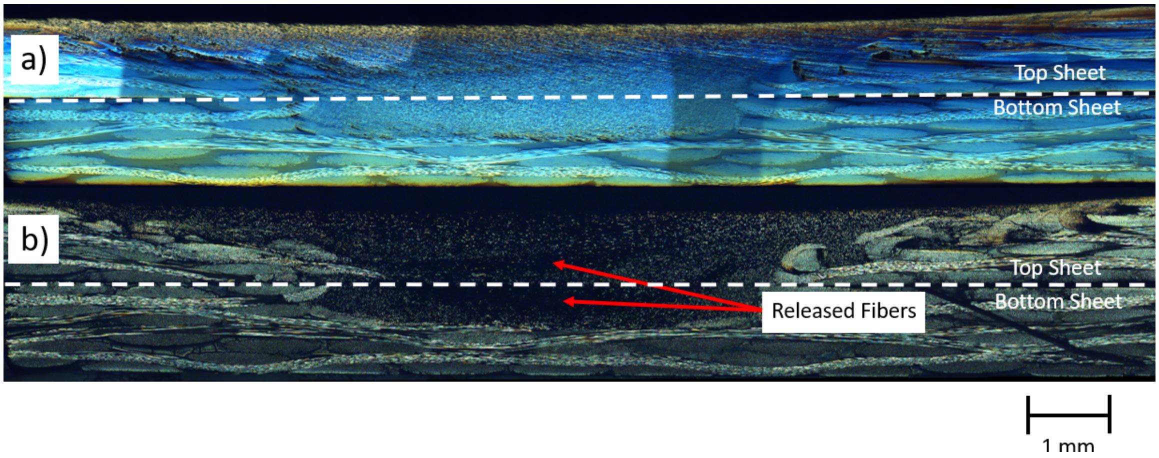

Figure 7.3: Cross section of welded joint a)pre-etching and b)post-etching

bright spots correspond to fiber ends. Smaller fibers populated the dark regions before etching and were small enough to be released once the polymer was removed. Thus, the etched cross sections confirm claims made in the previous study that small particles populate the region deep in the weld zone [179].

Figure 7.4 zooms in on the weld from figure 7.3 under an SEM. The SEM provides a field of depth with the etched cross sections. At the boundary of the weld zone, the fibers orient into the page, or along the interface of the weld zone and base material. In the middle of the weld zone, the fibers tend to orient primarily across the weld zone tangent to the rotating tool. The revealed shape from CF exposure post-etching confirms the validity of those claims made in previous study [179].

Figure 7.5 compares the composite surfaces outside of the weld zone for each annealing condition under polarized light. Conditions A1 (figure 7.5a) and A2 (figure (7.5b)) show sharp contrasts in color under polarized light with very little difference between them. Figure 7.5c does not show these color contrasts in condition A3 with an overall dull appearance which can also be observed upon visual inspection. The dull surface appearance in A3 results from oxidation at higher annealing temperatures [182]. Color variations between annealing conditions are not visible in specimen cross sections due to the lack of oxygen during annealing. A3 specimens also appear opaque compared A1 and A2 specimens in non-polarized light. Increased opaqueness in crystalline polymers often indicates higher degrees of crystallinity since crystallites can scatter visible light [25]. Degree of crystallinity is not the sole metric for a polymer's transparency. After all, many opaque polymers, such as acrylonitrile butadiene styrene (ABS), come in non-transparent forms. Poly 4-methyl pentene-1, though highly crystalline, is transparent since the crystallites are too small to scatter visible light. Rather, the degree of homogeneity greatly influences a polymer's transparency [191], and the increased crystallinity of A3 specimens improves homogeneity.

Figure 7.6 shows defects in the polymer matrix in cross sections of A1 and A3 specimens. Insufficient

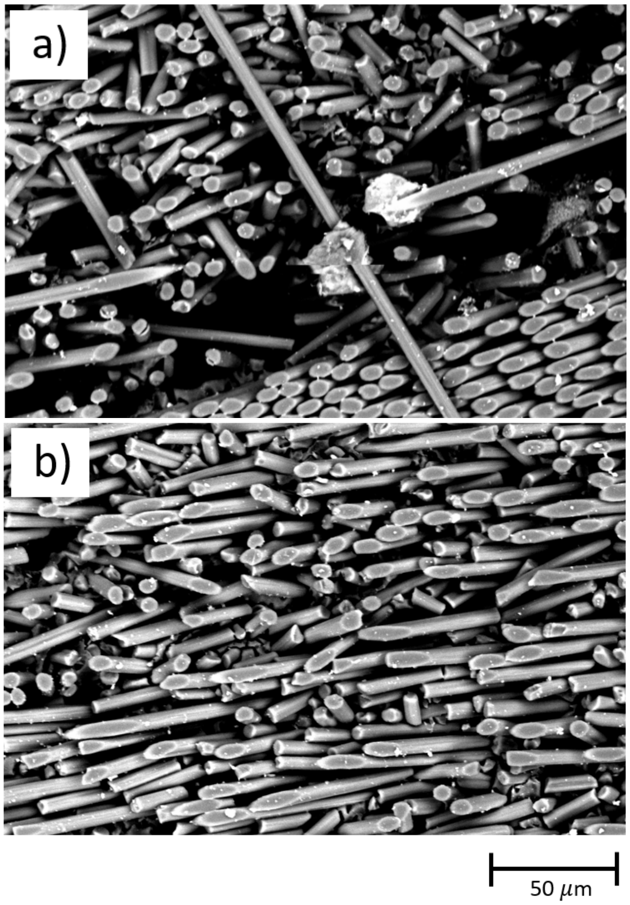

Figure 7.4: Etched SEM cross sections at a)weld zone boundary and b) middle of weld zone.

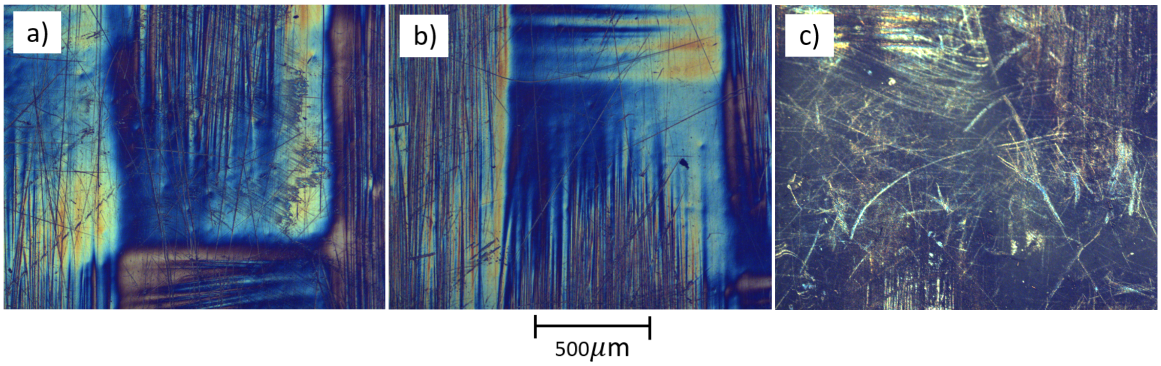

Figure 7.5: Top Surfaces of annealing conditions a) A1 b) A2 c) A3. Scale bar applies to all subfigures.

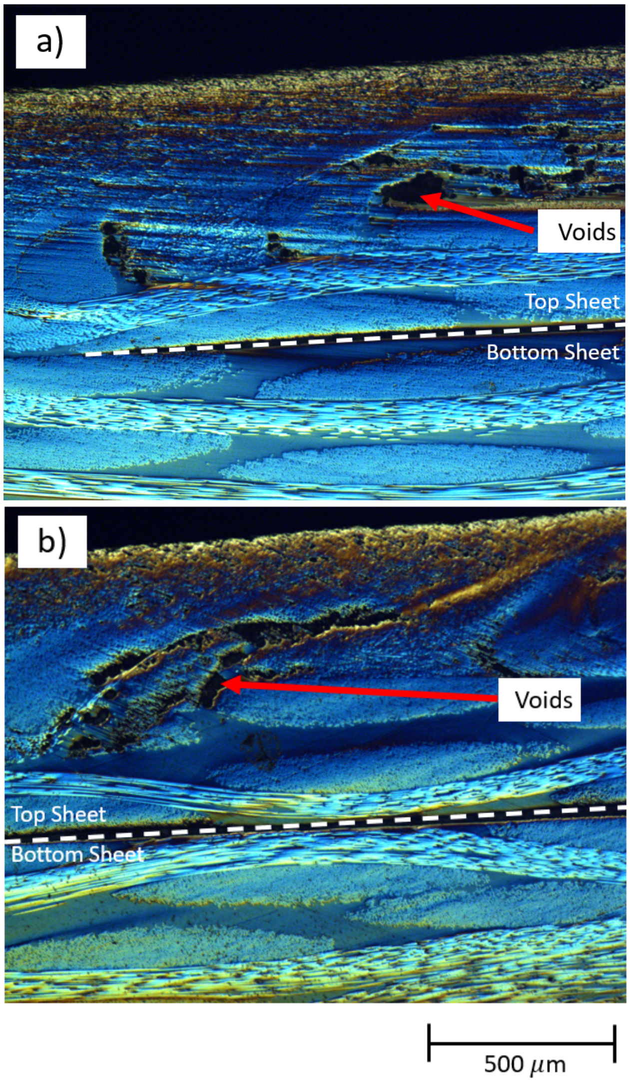

Figure 7.6: Voids visible in weld cross section specimens in conditions a) A1 and b) A3.

heating during FSW causes low matrix mobility and uneven cooling rates that leads to void formation [163, 167]. Lower processing temperatures along the retreating side (RS) of the weld and lack of swept material forging along the backside of the tool contribute to pronounced defects in this region as well [9]. Highly eccentric filler materials such as short carbon fibers also make it difficult for the molten polymer to fully encapsulate them and exasperate formation of defects [168].

Annealing has been shown to reduce the porosity in CFRTP especially in 3D printed parts. Yu et al. report that annealing reduced overall porosity by 41.40% in printed CF reinforced PEEK annealed at 240°C, though individual pore size increased. The mechanism for pore reduction is combination of voids at high annealing temperatures which can travel to the surface and expel from the composite [184]. This phenomenon does not appear to occur in the FSW joints. No significant difference arises in the number of small pores between FSW annealing conditions. The largest voids in the welded specimens form near clusters of long fibers, especially those that protrude across the base material/weld zone boundary. Handwerker et al. observed a similar phenomenon in PA6 reinforced with continuous glass fibers. In their study, large pores formed between long fiber strands and were resistant to expulsion during the annealing process [183]. Thus it appears that void mitigation must be addressed in the FSW process, as post-weld annealing does not annihilate these defects.

Though ineffective at removing pores in the matrix, post-weld annealing does have a pronounced effect on adhesion between the matrix and fibers. Figure 7.7 shows fracture surfaces of specimens pertaining to each annealing condition under an SEM. Figure 7.7a shows fracture surfaces of an A1 condition. The fiber surfaces are nearly stripped clean of polymer indicating adhesive failure and weak fiber/matrix interface. A similar trend presents itself in the A2 condition with adhesive failure on the fiber/matrix interface. Figure 7.7b shows polymer tearing with a smooth texture. In the A3 condition (figure 7.7c), fractured fibers are nearly fully encapsulated in polymer with primarily cohesive failure. The high temperature annealed polymer also consists of a rough surface texture due to the increased crystallinity in the polymer. Fiber encapsulation and texture in A3 specimens suggests improvements to the fiber-matrix interface bond as well as overall bulk matrix strength [181, 192, 193, 194, 195].

### 7.3.2 Thermal Analysis

The base laminate sheet has 42% CF composition by weight according to Toray Advanced Composites [166], but this weight fraction likely does not represent highly localized specimens in the weld zone disrupted by FSW. Thus, the weight fractions of CF and polymer in the composite are estimated using measured changes in mass caused by thermal degradation during TGA runs. Equation 7.2 expresses the weight fraction of carbon fiber in the composite:

$$w_c = \frac{w_f - a}{b - a} \tag{7.2}$$

$w_c$ is the weight percent CF, $w_f$ is the total remaining composite weight fraction taken from the TGA curve, and $a$ and $b$ are the theoretical remaining post degradation weight fractions of pure polymer and CF, respectively. For $T_f = 900°C$, $a$ is estimated to be 0.48 [189], and $b$ is estimated to be 0.96 [196]. $a$ was estimated based on PEEK thermal degradation since the literature for LMPAEK was not available at the time of this research. Due to the near identical local order of PEEK and LMPAEK [186], similar maximum thermal degradation is assumed.

Table 7.2 lists the averaged results from TGA runs including calculated initial % polymer/CF composition. $T_{95}$ represents the temperature for 5% weight loss in the composite to compare thermal stability. Figure

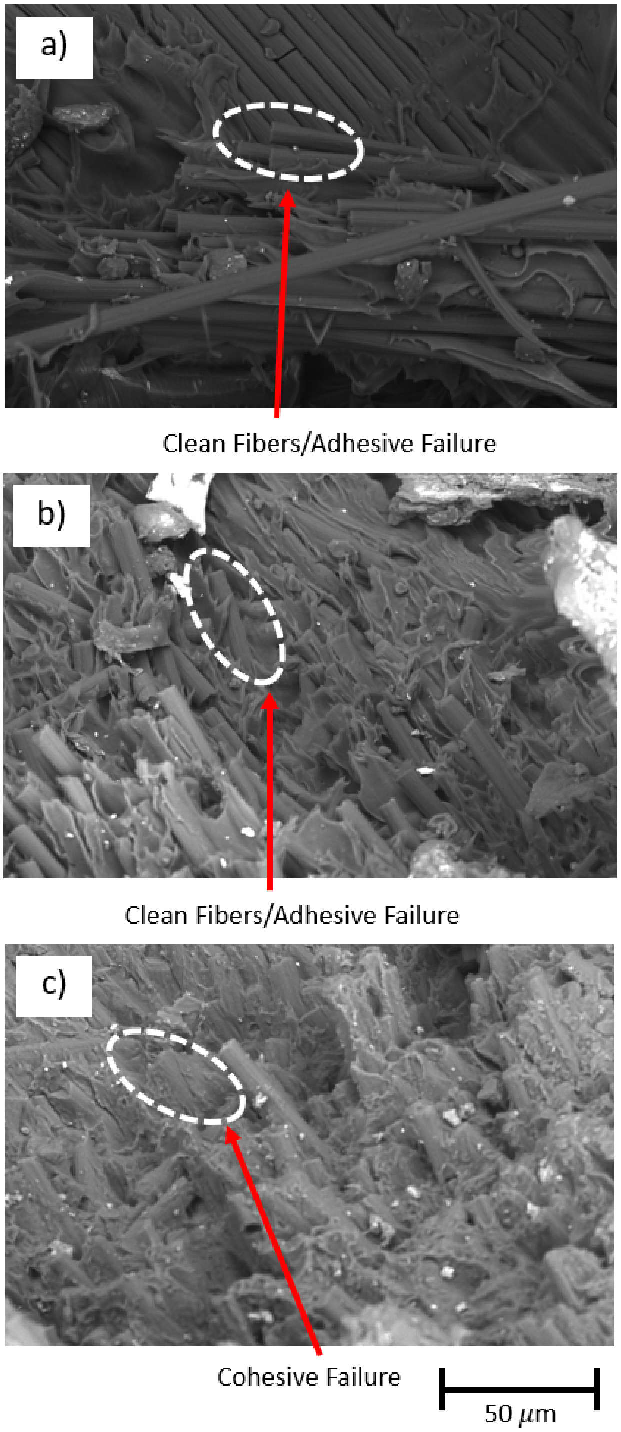

Figure 7.7: Fracture surfaces of annealing conditions under an SEM for a) A1 b) A2 c) A3.

Table 7.2: Summary of average TGA results

| **Anneal Condition** | $w_f$ | $w_c$ | $T_{95}$ (°C) | $\sigma$ (°C) |
|---|---|---|---|---|
| Base | 0.8036 | 0.6742 | 584.30 | 0.71 |
| A1 | 0.8051 | 0.6774 | 553.59 | 5.61 |
| A2 | 0.8065 | 0.6802 | 554.46 | 0.99 |
| A3 | 0.8134 | 0.6946 | 562.29 | 5.51 |

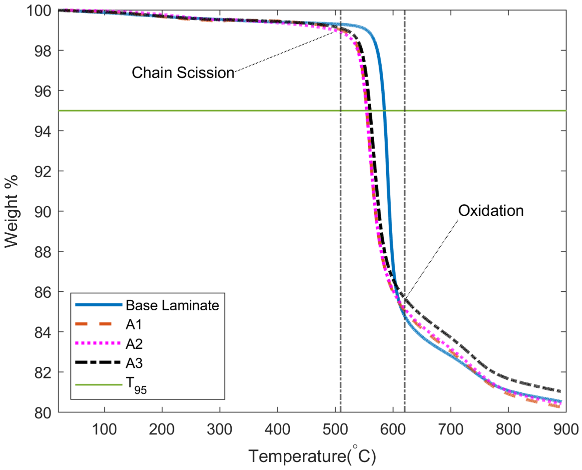

Figure 7.8: TGA curves for weld zones subject to each annealing condition.

7.8 shows the TGA curves for weld zones subjected to various annealing conditions.

All FSW specimens exhibit lower degradation temperatures than the base material. CF's tend to increase degradation temperatures compared to neat polymers due to suppression of bulk heat transmission [197]. The woven fibers in the base material form pockets of polymers that further contribute to this suppression, while the chopped fibers in welded specimens no longer form these boundaries. A3 tends to have slightly higher degradation temperatures than A1 and A2, though these improvements are marginal.

Like PEEK, LMPAEK degrades in a two step process. Changes in the TGA curve slopes in figure 7.8 reveal the degradation steps. The first step involved random chain scission of ether and ketone bonds indicated by a sharp linear drop in weight % [198]. The second step results from oxidation of carbonaceous char produced during the first step [197]. Flattening of the TGA curves at 900°C indicate completion of polymer degradation.

Figure 7.9 shows the DSC curves for each annealing condition and the non-annealed base material. Endotherms point upwards and exotherms point down. A distinct glass transition curve does not present itself in any of the specimen types. The lack of a distinct glass transition peak can be attributed to a high degree of crystallinity since the glass transition forms from the amorphous regions [183]. Table 7.3 summarizes the average peak melting points and crystallinity for specimens subject to each annealing condition. All specimens present a primary melting curve peak ($T_{m1}$) around 315°C. Annealing temperatures cause little shift in the peek primary melting point, which suggests little sensitivity of the primary crystal phase to both welding and annealing [199, 200]. A1 and A2 specimens show an additional endothermic curve at lower temperatures. $T_{m2}$ indicates the peeks of these curves. For A1, this occurs at approximately 20°C above the LMPAEK literature $T_g$ value of 147°C [166]. For A2, the $T_{m2}$ lies approximately 38° above the annealing temperature. These secondary peaks are attributed to the double melting behavior characteristic of polymers in the PAEK family resulting from reorganization of amorphous phases within smaller crystallites [186, 200]. Annealing has been shown to increase the peak of these secondary phases with higher annealing temperatures in LMPAEK [186]. Thus, specimens with higher degrees of crystallinity absorb the secondary phase curves within the primary curves. For this reason, the base material and A3 specimens do not present a secondary melting curve with the exception of one A3 specimen.

Equation 7.3 provides the means to calculate % crystallinity from DSC curves:

$$X_c = \frac{\Delta H_m}{H_{ref}(1 - w_c)} \tag{7.3}$$

$H_m$ is the melting enthalpy calculated from the area under the curve with an extrapolated baseline. $H_{ref}$ is the maximum theoretical crystallization enthalpy (130 J/g°C [187]), and $w_c$ is the CF weight fraction. Table 7.3 displays the resulting % crystallinity for each annealing condition. A1 specimens have reduced crystallinity from the base material resulting from the rapid cooling during FSW. However, these specimens are not completely amorphous with a 14.09% crystalline content, demonstrating the rapid crystallization kinetics of LMPAEK. LMPAEK composites subject to tape layup achieve less than 10% crystallinity without post heat treatment [187]. FSW is has slower processing speeds two orders of magnitude than tape layup that provides additional time for the polymer to crystallize. A2 specimens have near negligible improvements to overall crystalline content, though the shifted and more pronounced secondary enthalpy curves and higher average crystalline content at 16.04% shows beginnings of such improvements. A3 specimens present crystalline content of 27.91% with significant improvements to A1 and A2 and surpasses the crystalline content of the base material.

The crystalline content of A3 specimens has been achieved in LMPAEK in other researchers as well. Audoit et al. reports a maximum LMPAEK crystallinity of 26% for specimens annealed at for two hours at 250°C from the glass while the maximum crystallinity achieved from the melt was 27% in non-reinforced polymer [186]. Schiel et al. achieved 29.55% crystallinity in unidirectional reinforced tapes subject to tempering at 290°C for 17 hours [187]. Thus, the available increased in crystallinity was exhausted in this study. Results from Audoit et al. and Schiel et al. also show that the overall processing time can be significantly

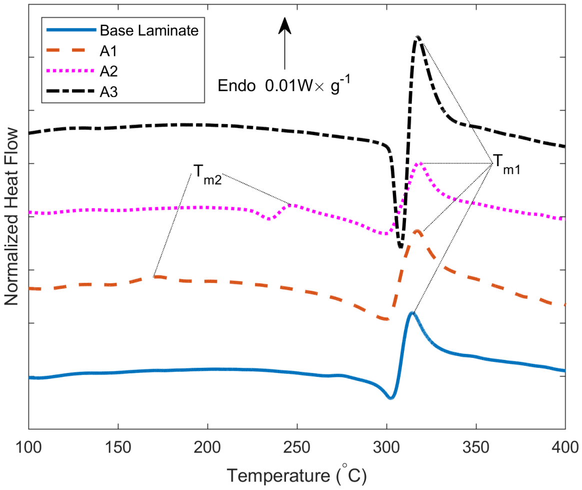

Figure 7.9: DSC curves for weld zones subject to each annealing condition.

Table 7.3: Summary of Average DSC Results

| **Anneal Condition** | $T_{m1}$ (°C) | $T_{m2}$ (°C) | $X_c$ (%) |
|---|---|---|---|
| Base | 314.46±0.43 | n/a | 21.39±5.07 |
| A1 | 315.69±2.62 | 168.79±4.48 | 14.09±2.89 |
| A2 | 316.78±1.24 | 238.85±9.41 | 16.04±2.65 |
| A3 | 319.69±3.51 | 276.5* | 27.91±0.40 |

* indicates measurable in one specimen.

reduced. Therefore, future study requires implementing effects of high temperature heat treatment for less duration to improve the overall manufacturing efficiency.

Lack of information on LMPAEK's degradation behavior required assumptions based on those observed in PEEK to estimate the CF content. It appears from the conclusions in Audoit et al. that making such assumptions about LMPAEK's degradation behavior are justified. Calculating the crystallinity fraction can vary depending on observation method. DSC tends to overestimate crystallinity [201]. Non-isothermal conditions during DSC allows the material to continue annealing while taking measurements. The DSC heating rate has a large influence on the degree to which further crystallization occurs [202]. The non-isothermal nature of DSC runs may overestimate crystallinity in A1 and A2 specimens. This possibility is not of concern for the purposes of this work, as clear imrovements arise from the A3 condition.

### 7.3.3 X-ray Diffraction

Figure 7.10 shows the resulting normalized XRD curves for each annealing condition. Peaks at approximately 25° and 43° indicate the (002) and (101) planes of T300 CF [196]. Since the temperatures experienced during the annealing process are too low to alter the CF's structure, the curves in figure 7.10 are normalized to the intensity of the (002) peak.

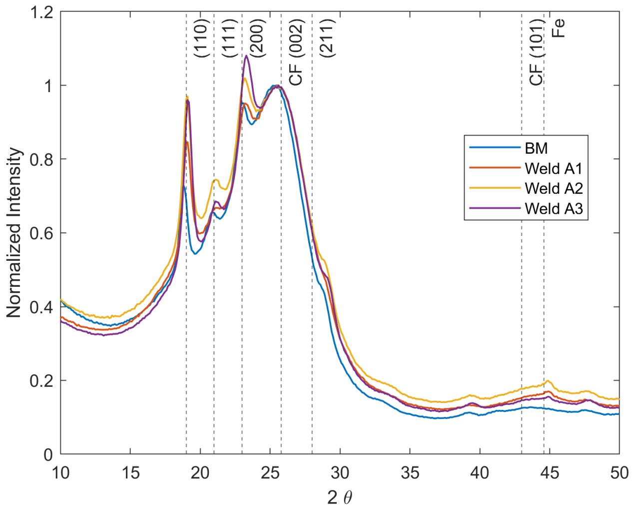

Figure 7.10: XRD Curves

A peak at approximately 45° appears in the weld zones, but not the base material. An XRD peek at 44.6° corresponds to iron according to the Crystallography Open Database CODID 1100108, which indicates deposited material in the weld zone due to tool wear. Powder from these regions also reveal small particles exclusive to the weld zone with magnetic properties.

Four peaks at approximately 19°, 21°, 23°, and 28° correspond to the polymer matrix. These peaks match nearly perfectly to those found from PEEK XRD curves with an orthorhombic structure, indicative of the (110), (111), (200), and (211) crystal planes [201]. The XRD curves were deconstructed into individual diffraction peaks using LIPRAS. Figure 7.11 shows fitted curves corresponding to each crystalline peak in the A3 weld zone. Figure 7.12 plots the intensity of each peak. The CF peak intensity is consistent across each annealing condition, indicating that normalizing the XRD curves around the CF curve is adequate and confirming that the welding and heat treating processes do not change the CF's crystalline structure. The intensity corresponding the (110) crystal plane increases from the base material with each annealing condition. The A3 condition provides the only noticable contribution to the (200) crystal plane. The increased intensity of these crystal planes may indicated more preferred orientation in a transcrystalline layer near the fiber/matrix interface [203].

FSW shifts all of corresponding polymer peaks to the right by an average of 0.30° compared to the base material with no significant alteration to the CF peak measured at $2\theta = 25.8^\circ$. Incorporation of fibers does not change the crystal form of PEEK [26, 204]. Therefore, shifts exclusive to the polymer peaks in welded specimens compared to the non-welded base material indicates that FSW slightly increases the unit cell spacing, resulting in a reduction in crystal packing.

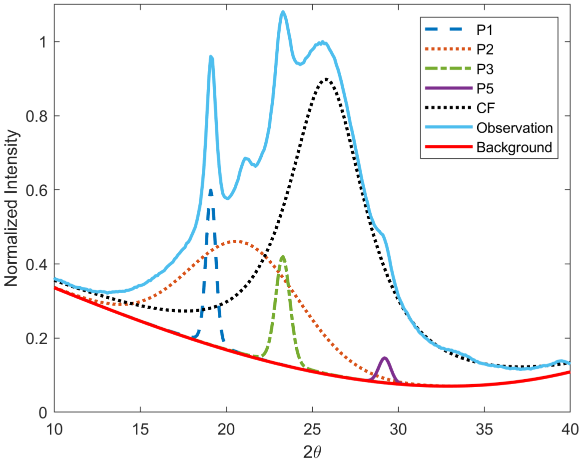

Deconvoluted XRD curves with background and observation.

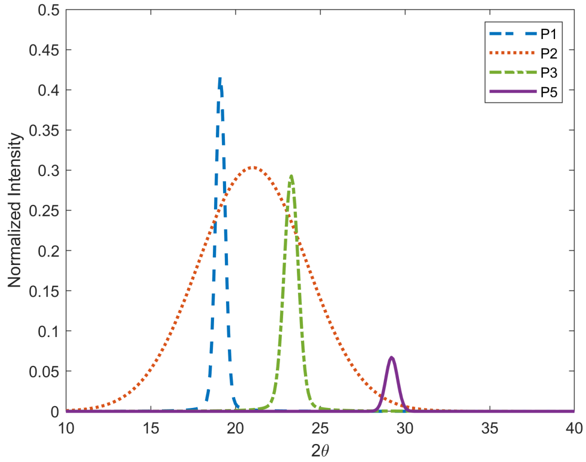

Deconvoluted XRD curves with background removed.

Figure 7.11: Deconstructed A3 XRD curve using Pseudo-Voigt fits for each diffraction peak.

Figure 7.13 reports the crystallite size for each peak under each annealing condition, calculated using equation 7.1. The A3 condition slightly increases the (110) and (200) crystal sizes. FSW reduces the (211) crystal size in all annealing conditions. The XRD curves suggest that FSW and post-weld annealing provide change to LMPAEK's crystal structure. More notably though, is that the XRD curves confirm the structural similarity between LMPAEK and PEEK.

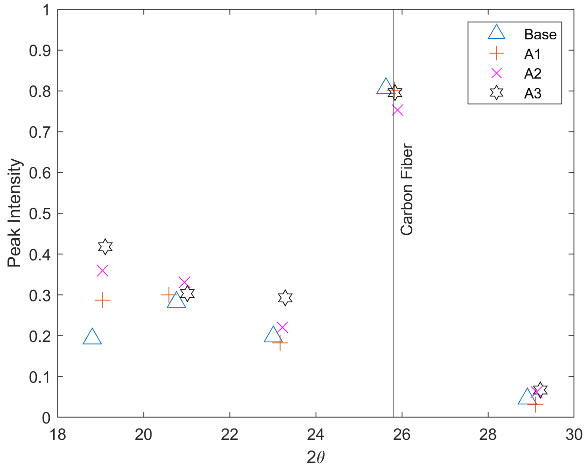

Figure 7.12: Peak intensities for each diffraction peak.

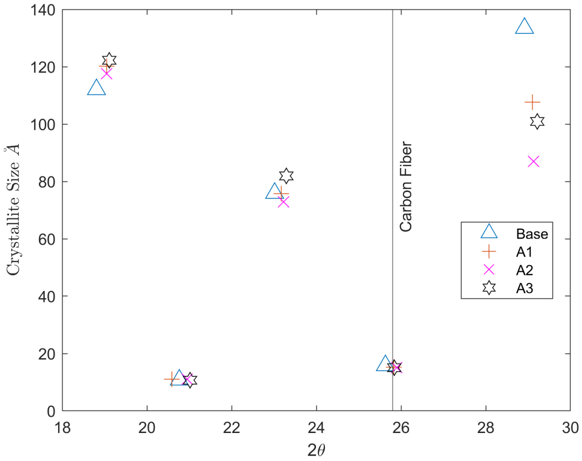

Figure 7.13: Crystallite size calculated by the Scherrer Formula

### 7.3.4 Mechanical Properties

All specimens subjected to single lap shear testing in a load frame fractured via tensile fracture in the top sheet weld zone. Fracture occurred along the weld zone/base material boundary interface in all specimens regardless of annealing condition. The fracture location in single lap shear specimens closely resembles that of those observed in previous work [179]. Figure 7.14 illustrates the fracture location in each annealing condition.

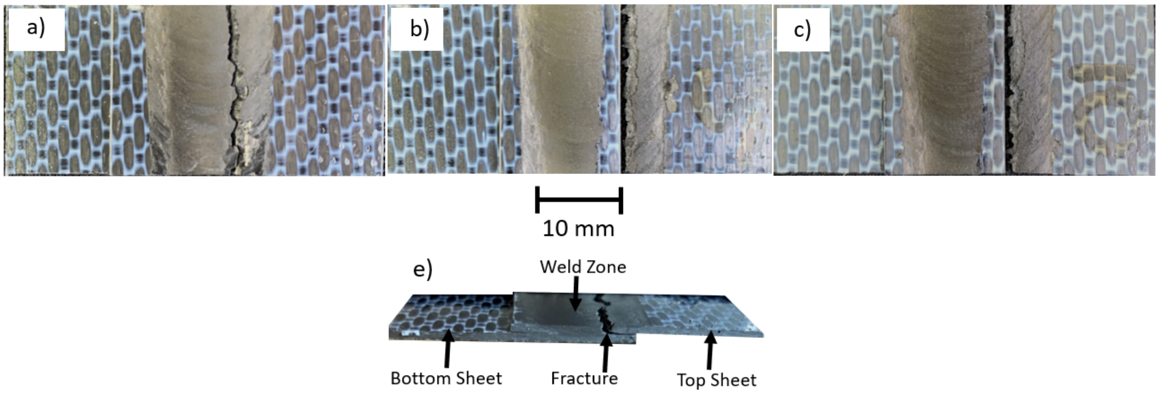

Figure 7.14: Fracture location of single lap shear specimens. a) A1 b) A2 c) A3 e) Cross view of typical fracture specimen.

Identical welding parameters were used in all welded joints as previous study with an identical tool [179]. The only exception to these remarks is that in this current study the tool pins were fabricated from O3 tool steel and hardened, while the aforementioned study utilized non-hardened tool pins. Average weld strengths in non-annealed specimens were lower than comparable welds from the previous study with no obvious justification [179]. The discrepancy in non-annealed weld strength between each study may be caused by highly sensitive shoulder engagement resulting from manual tool tilt angle on the milling machine head. Shoulder contact during welding of thin materials with shallow tool plunges exacerbates manual tool tilt error. However, the mechanical results in this study do indicate influence of post-weld annealing on FSW joint strength in composites. Table 7.4 lists the average tensile strengths and relative toughness measured for each annealing condition. The relative toughness was calculated using the area under the curve of stress vs crosshead displacement plots. The true toughness is not reported since a device to measure true strain was not available at the time of mechanical testing. For comparative purposes, the relative toughness using crosshead displacement is sufficient. Similarly, relative modulus was calculated from the slope of the linear regime of the stress vs displacement plots.

A3 welds present a noticeable increase in both UTS and relative toughness compared to A1 and A2 welds. Table 7.5 lists strength relationships between each annealing condition. A2 does not have a statistically significant improvement in UTS or relative toughness over A1 at a 95% confidence interval ($p < 0.05$). A3 on the otherhand, does have statistically significant improvement in both UTS and relative toughness over both A1 and A2 with up to a 30% increase in average UTS. Relative tensile modulus conditions A1, A2, and A3 were 126.5 MPa/mm, 132.1 MPa/mm, and 135.1 MPa/mm, respectively. Though a positive correlation exists between annealing temperature and tensile modulus, variance in modulus prohibits statistical significance.

Table 7.4: Weld mechanical performance

| **Anneal Condition** | **Avg. UTS** (MPa) | $\sigma$ (MPa) | **Relative Toughness** (MPa · mm) | $\sigma$ (MPa · mm) |
|---|---|---|---|---|
| A1 | 46.36 | 9.06 | 20.24 | 14.60 |
| A2 | 48.18 | 3.49 | 21.80 | 10.51 |
| A3 | 60.64 | 7.53 | 38.64 | 17.16 |

Table 7.5: Comparison of mechanical performance between annealing conditions.

| **Comparison** | **% Increase** | **p-value** | **Statistical Significance** |
|---|---|---|---|
| **UTS** | | | |
| A1 & A2 | 4% | 0.800 | No |
| A1 & A3 | 26% | 0.024 | Yes |
| A2 & A3 | 30% | 0.040 | Yes |
| **Toughness** | | | |
| A1 & A2 | 8% | 0.389 | No |
| A1 & A3 | 91% | 0.019 | Yes |
| A2 & A3 | 77% | 0.011 | Yes |

To further validate the influence of post-weld annealing on UTS, a general linear model with analysis of variance (ANOVA) was used to check for overall statistical significance. The model also incorporated the influence of each tool pin as switching tool pins throughout the experiments may incorporate sources of variation through minuscule deviations in setup and pin dimension. The ANOVA model indicates statistically significant contribution of both the annealing condition ($p = 0.002$) and pin selection ($p = 0.000$). Figure 7.15 plots the mean effects of both the annealing condition and pin used on UTS. Welding runs using pin 4 had drastically reduced mechanical performance. Table 7.6 reports that welds subject to pin 4 had a lower thickness reduction from the base material than pines 1,2, and 3. Pin 4 welds were performed separately from the initial experiment to increase the number of replicates and required resetting the tool tilt angle, which only has 0.5° precision. Thus, very small deviations in the tool tilt can have large effects on the shoulder depth, which produced pronounced effects when welding thin materials. The results highlight the paramount importance of tooling setup since each pin was fabricated to the same specifications. However, pin 4 welds still have the same relationship between the annealing condition and UTS.

Table 7.6: Weld zone thickness reduction from base material for each pin selection.

| **Pin** | 1 | 2 | 3 | 4 |
|---|---|---|---|---|
| **Thickness Reduction (mm)** | 0.126 | 0.124 | 0.144 | 0.086 |

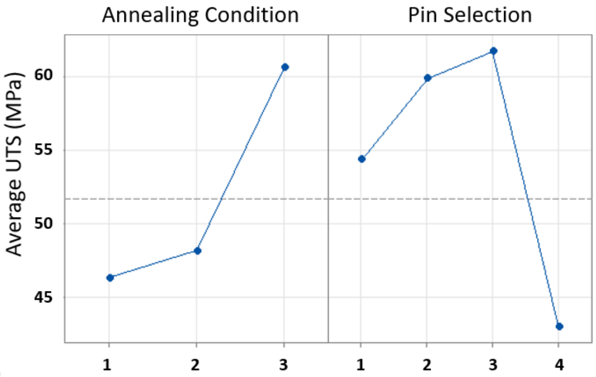

Figure 7.15: Average annealing and tool pin effects on UTS.

### 7.3.5 Future Work

Though improvements were observed in FSW joints from post-weld annealing, improvements must be made in future work to adapt FSW to CFRTP welding and make it a useful and competitive joining process. The continuation of porosity in this study's friction stir welded joints indicates that defect mitigation must occur during the welding process. Other researchers have demonstrated techniques utilizing preheating [67], in-situ heating [72], and heated stationary shoulders [12, 57] can significantly reduce void formation. Void formation not only occurs in composite FSW, but presents issue in many composite manufacturing processes [205]. Research shows that air void content in composites can be reduced by applying pressure [183]. This modification to the FSW process with applied pressure to the weld zone may help reduce porosity.

Another downfall to FSW for CFRTP is its slow joining times. It was theorized that void mitigation by annealing would allow for faster welding speeds. The results do not justify this hypothesis, but the aforementioned modifications to the FSW process may allow faster welding speeds of CFRTP.

## 7.4 Conclusion

This study explores the effect of post-weld annealing on lapped woven carbon fiber reinforced thermoplastic (CFRTP) joined by friction stir welding (FSW). The variable condition includes non-annealed welds, welds annealed at a 200°C low temperarure condition, and welds annealed at a 280°C high temperature condition. This work satisfies goals of advancing three key areas including the understanding of low-melt polyaryletherketone (LMPAEK), annealing effects on welded carbon fiber reinforced thermoplastic, and feasibility and identifying necessary aspects to improve when using FSW to join thermoplastics reinforced with continuous carbon fibers.

Annealing LMPAEK just below its melting temperature increases the mechanical performance of friction stir welded joints with up to a 30% improvement in lap shear strength and 91% increase in toughness over non-annealed joints. Improvements in mechanical performance result from increases in the polymer matrix crystalline content. Joints subject to high temperature annealing yielded a 27.91% crystalline content, which is among the maximum achieved for LMPAEK in other studies. Response to thermal treatment and crystalline structure also provide additional evidence of LMPAEK's similar structure to PEEK despite its slight molecular modifications. Post-weld annealing fails to reduce porosity in the welded joints, which limits the potential of FSW joint performance in CFRTP's with continuous reinforcement. However, this works shows clear influence to LMPAEK's structure and performance due to post-weld processing, which can be applied to other processing methods including competing welding methods, molding, and composite tape layup.

# CHAPTER 8

## Conclusion

The culmination of research in this dissertation satisfies the mission to advance the field of friction stir welding in the realm of polymers and polymer composites. This work does not focus solely on one intended application for polymer joining. Rather, various research projects consider neat polymers and polymer composites with applications for a variety of vehicles, infrastructure, as well as general polymer structures. Many of the principles discussed in each chapter has a high relation with each other, especially regarding fundamental polymer welding principles.

Successful adaptation of FSW for thermoplastic materials requires acknowledging the differences in the fundamental structure between polymers and metals to allow for adequate adjustments to the traditional FSW welding configurations and processing parameters. Each study adapted unique tooling and fixtures to accommodate the different materials and weld geometries. Both conventional FSW tools and heated stationary shoulder tools were used throughout this dissertation.

Study of the tool thread pitch in conjunction with other welding parameters identified relationships that typically receive little attention in polymer FSW research. This work contributes to the field's knowledge of complex relationships between welding parameters and tooling and their effective response on joint quality and machine requirements. Ultimately, the results highlight the importance of slow welding speeds during polymer FSW to promote diffusion of polymer across the joint.

Joining of PVC pipe couplings introduces a unique application for FSW in a new sector. Most notably, identifying the feasibility for FSW as a portable joining process of polymers increases its use cases, since most currently employed FSW applications requires the use of large and heavy equipment. High performance of FSW joints under hydraulic pressure also shows that it is a competitive joining process to existing pipe joining technology.

The development of top plate FSP for forming metal/polymer composites placed an emphasis on efficiently forming surface composites over a wide area of a polymer substrate. Further classification of improved electrical and thermal conductivity over the base polymer in the processed region shows that filler materials can be selectively integrated into surfaces to form multi-functional structures.

FSW of woven CFRTP laminate demonstrates a highly relevant application for increasingly common materials in aerospace industries. This work shows promising results for joint performance and highlights the benefits of little required material preparation for overall manufacturing efficiency. Follow-up research performing post-weld annealing reveals improved material characteristics for welds subjected to relatively fast processing times. Semi-crystalline thermoplastic joint performance in general often does not reach its potential due to rapid cooling during fast joint processing. Thus, heat treating focused research applies to all thermoplastic composite welding methods. Additionally, this CFRTP research further improves the knowledge of processibility for LMPAEK which is essential for its continued adoption in aerospace industries.

## Future Work

Though this work gives a variety of contributions to the field of polymeric FSW, there are several areas in which future considerations can further mature the field. Adoption of FSW in polymer industry requires continued research to make FSW a viable and competitive process for joining thermoplastics and composites.

Perhaps the biggest learned lesson from the work in Chapter 3 is the requirement for slow welding speeds when joining thermoplastics with current FSW methods due to physical constraints of thermoplastics. Slow welding speeds serve as a disadvantage for FSW, as other select thermoplastic welding methods can weld at speeds an order of magnitude faster. Thus, improving welding speeds should be of high priority for future research, and may be accomplished with advancements to assisted heating methods.

FSW of PVC pipe joints will benefit from experimentation with variable pipe diameters and implementation of other coupled attachments, such as elbows and tee junctions. Pressure testing of welded pipe sections at various internal fluid temperatures will improve the understanding of FSW joint performance in comparison to current solvent welded joints in extreme conditions. Finally, this work promotes a portable use case for FSW, which should be demonstrated with the development of a portable device.

Further development of top plate FSP will benefit from a focus on further refining the deposited metal particle size for improved mechanical properties. Additionally, successful demonstrations of top plate FSP on curved surfaces will make FSP more applicable to composite formation on complex surfaces.

Novel woven CFRTP joint fabrication by FSW unlocks endless avenues of future research. Experiments with other fiber layup forms will increase FSW's accessibility to more primary and secondary aerospace structures. Further refinement of the process to address physical defects will further promote the application of FSW for joining composites subject to demanding performance requirements. Continued adoption of CFRTP in aerospace industries requires the capability to manufacture and join higher volumes of composites, which further necessitates the need to improve processing times. Post-weld heat treating may also show enhanced benefits from friction stir welded joints consisting of fewer defects welded under faster speeds. Eliminating porous defects in friction stir welded joints will reduce the dominating strength reduction so that the benefits of post-weld annealing induced crystallinity and polymer interdiffusion can be fully realized.

# Appendix A

## Formation of Encapsulated Joint via Friction Stir Extrusion

The following work considers manufacturing processes involving friction stir extrusion. It does not utilize polymer joints and therefore does not follow the scope of the other chapters. Therefore, this work is included as a section in the appendix. This work was previously published in *Manufacturing Letters* as:

L. T. Wilkins, Eric. L. Zhang, A.M. Strauss, Formation of Encapsulated Joint via Friction Stir Extrusion. *Manufacturing Letters*. April 2022; 32:(73-76).

### Abstract

There is a need for simple and reliable pyrotechnic devices for spacecraft component release. In this work, a pyrotechnic joint was formed between lapped aluminum plates, with the lower plate having a partially thermite-filled cylindrical channel axially parallel to the tool path. Using friction stir extrusion (FSE), material from the top plate flowed into the channel and formed a mechanical interlock, encasing the thermite inside. Joints with various channel radii were prepared and ignited. Successful thermite reaction propagation was observed. Once this technology matures, FSE pyrotechnic joints may be an alternative to current pyrotechnic release mechanisms utilizing no moving parts.

### A.1 Introduction

Pyrotechnic devices in spacecraft are mechanisms actuated using highly energetic materials. Such devices come in many forms and are used for functions including vehicle stage separation, vehicle destruction, fuel shut off, releasing instrumentation covers, equipment deployment, and aircraft escape systems for pilots [206, 207, 208]. They include pin pullers, explosive bolts, and cable cutters/guillotines [206, 208]. One challenge with many of these devices are that they are single use, which means that they cannot be tested prior to a mission without destruction. Lot acceptance testing (LAT) detonates a small subset out of a large quantity to calculate the probability of device failure [207]. LAT does not guarantee success of a working unit and is costly since many devices consisting of complex parts are sacrificed. Explosions from pyrotechnic devices can also send shocks through a vessel, where attenuation can be harmful to electronics and other components on board [209]. Thermite, a composition typically consisting of aluminum and a metal-oxide, creates extremely high temperatures through an oxidation-reduction reaction [210]. Heats of reaction can range between 2-4kJ/mol depending on composition with temperatures exceeding 3000 K [211]. Heat generated and reaction rates are tunable by material composition, and thermite architectures have been shown to be reliable heat sources [210, 211, 212]. Thermites possess potential to serve as the reactive material in pyrotechnic devices due to their low shock characteristics, production of few gas products, and sufficient enthalpy values to self-sustain combustion necessary for device attenuation [213]. This work explores a new joint type assembled by friction stir extrusion (FSE), where thermite embedded between two joined plates shows potential as a mechanism for a pyrotechnic metal joint separator. This joint separator consists of no moving parts and is integral to the joint structure, adding simplicity over other pyrotechnic forms. FSE, described in Evans et. al, uses the principles of friction stir welding (FSW) to soften a top plate via the friction of a rotating tool, forcing material from the top plate into a premachined geometry below it [214]. The nature of extrusion also allows for dissimilar material joining, including aluminum to graphite [215], aluminum to steel [216, 217], dissimilar aluminum alloys [218], and aluminum to copper via dieless friction stir extrusion-brazing (DFSE-B) [219]. The simplicity of this pyrotechnic device coupled with thermite's tunability and reliability offers great potential to serve as a vehicle stage or device separator.

## A.2 Materials and Methods

### A.2.1 Sample Preparation

A 25 mm thick block of aluminum was prepared with drilled holes longitudinally placed 2mm below the surface. The hole diameters were 6.35 mm, 9.53 mm, and 13.72 mm and were approximately 50mm deep. Each hole size will be referred to as size 1, 2, and 3, respectively. A thermite paste was formed consisting of 30 micron iron oxide ($Fe_2O_3$), 30 micron aluminum powder ($Al$), and calcium sulfate hemi-hydrate ($Ca_2SO_4 \cdot \frac{1}{2}H_2O$) in a 3:2:2 ratio. The iron oxide and aluminum powders were supplied by Alpha Chemicals. Commonly known as Plaster of Paris, $Ca_2SO_4 \cdot \frac{1}{2}H_2O$ acts both as a fuel, influencing reaction speed and temperature, and a binder that forms a paste when mixed with water.

Thermite paste was loaded and packed into the drilled holes using an arbor press. Relief holes in the top of the block allowed air and excess water to escape. Once the paste cured overnight, 3.18mm wide notches were milled along the length of the holes to create a channel, shown in figure A.1.

### A.2.2 Extrusion

A 6.35 mm thick AA6061 plate was clamped on top of the aluminum block. The FSE process was performed using a modified milling machine with a tool consisting of a 25.4 mm diameter scrolled parabolic shoulder and a 6.35 mm diameter by 5 mm long left-hand threaded pin. The tool rotated clockwise to facilitate downward material flow. The tool parameters included a 1500 RPM rotation speed, 75 mm/min traverse speed, 5.71 mm plunge depth, and 1.5° tool tilt angle. The tool plunged into the top plate and traversed centered above the length of the channel, shown in figure A.2.

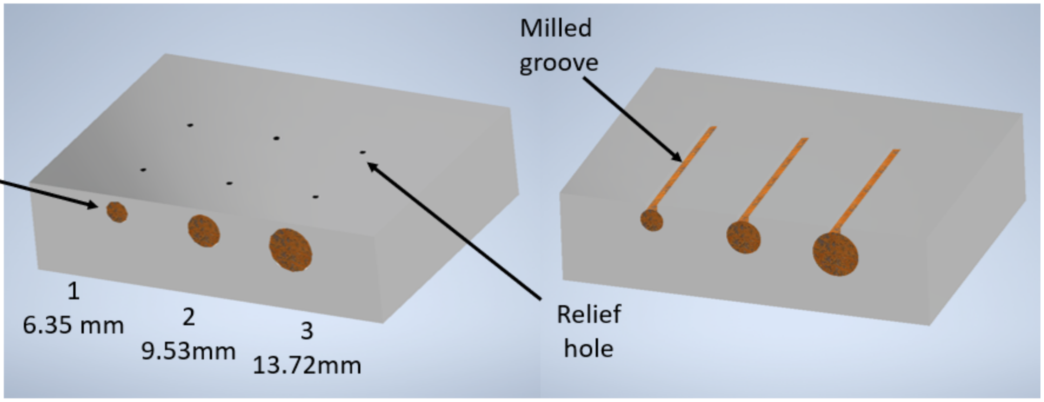

Figure A.1: Schematic of thermite packing process. Left: Thermite paste is packed in each channel. Air and water can escape from the relief holes. Right: Milled grooves following paste curing.

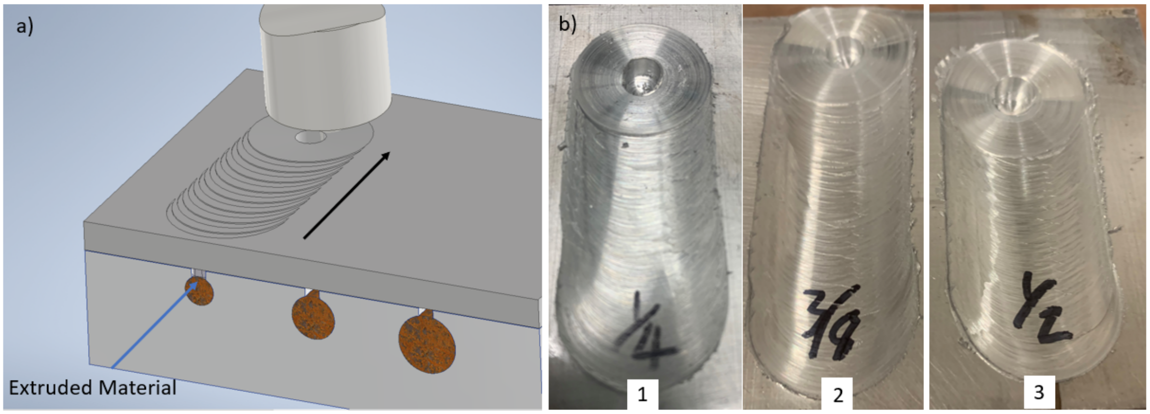

Figure A.2: Left: Diagram of FSE process. The extruded material from the top plate interlocks with the groove on the bottom channel. Right: Top view of completed FSE runs for each channel size.

### A.2.3 Ignition

Each joined section was oriented vertically in the vented enclosure. A small mound of excess cured thermite paste was placed on top of each hole with magnesium ribbon. A torch lit the magnesium to start the reaction.

## A.3 Results and Discussion

### A.3.1 Pre-ignition

FSE successfully formed sound joints over all three channel sizes via mechanical interlock between the top plate and the channel groove. The cured thermite remained packed inside of the channels and did not displace during extrusion. The plunge location was located along each channel approximately 6 mm from the channel inlet.

Figure A.3 shows cross sections of the extrusion specimens prior to ignition. These cross sections are located past the tool plunge zone. The top row provides a macroscopic view of the extrusion zone. Deformation around the channel forms a funnel-like extrusion with a tightly matching interface between the block and top plate. A fine line along this interface signifies that the joint is primarily made via interlock. The bottom of each extrusion has a slight bulge that provides a hooking effect with the slightly collapsed channel preventing pullout. The neck of each extrusion size measures approximately 2.85mm in width, suggesting the channel sizes in this study have little effect on the extrusion geometry due to adequate support from the thermite. The bottom row in figure A.3 shows further interlock at the microscopic scale. The micrographs do not portray superior microscopic interlocking on the advancing side compared to the retreating side (not shown).

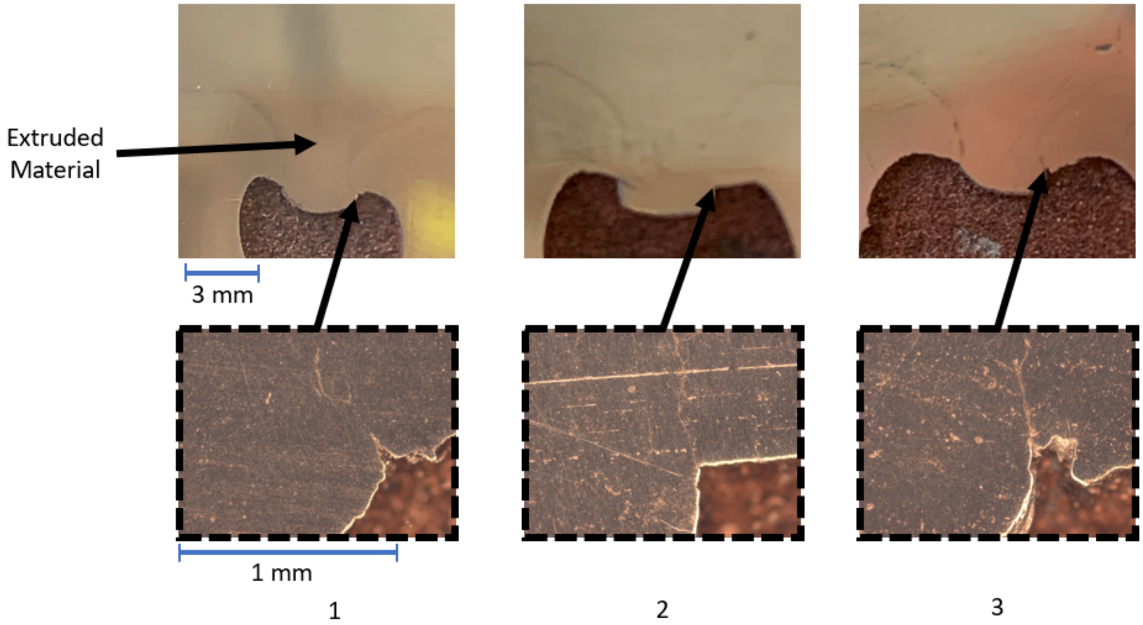

Figure A.3: Cross sections of thermite extrusions. The top row shows a macroscopic view. The bottom row shows the extrusion interface along the advancing side magnified under an optical microscope. The 3 mm and 1 mm scale bars refer to the macroscopic and microscopic images, respectively.

### A.3.2 Post-ignition

The thermite reaction propagated only to the tool plunge location in channel 1, while propagating entirely through channels 2 and 3 for approximately 20 seconds between ignition and completion. Flames protruded from the channel inlet, and grew up to approximately 100 mm in length for channel 2 and 200 mm in length for channel 3. The thermite reactions did not alter the integrity of the extrusions that would allow for aluminum plate separation. Figure A.4 shows the channels after sliding the top plates with an arbor press. The separated extrusion coupons revealed that the most material was extruded at the location of tool plunge, which is a result of initial material displacement by the pin. This displacement forms a deep bulge in the extrusion, effectively reducing the channel cross section. The energy transport in a thermite reaction relies on advection

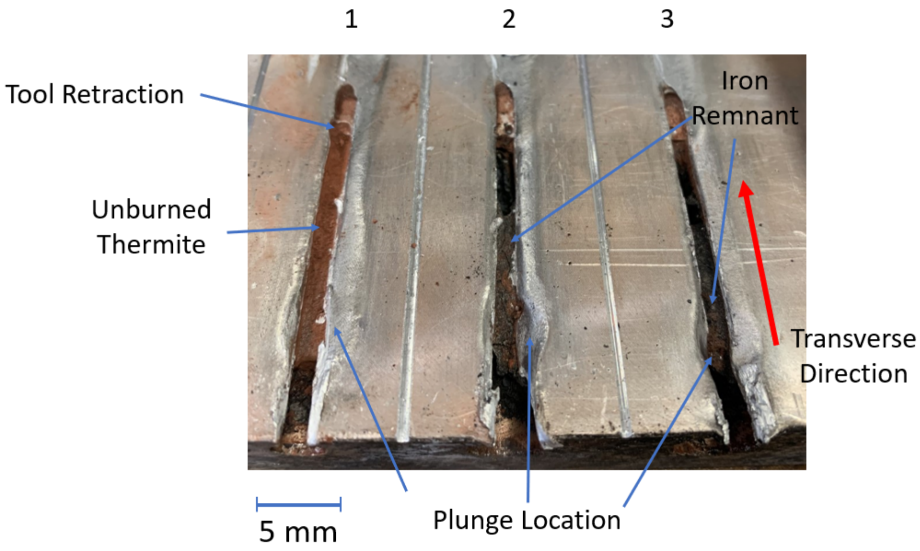

Figure A.4: Channels after removing the extruded top plate. Channel 1 (left) shows unburned thermite beyond the plunge location. Channels 2 and 3 (middle and right) show large deformation in the aluminum block under the plunge location and complete reaction of the thermite. The extrusion process begins at the plunge location and ends at tool retraction.

from transport of hot molten reactant products [220]. Thus, the cross section size at this scale affects the number of particles available to assist in the reaction. For channel 1, the reduction in cross section exceeded the minimum cross section threshold, prohibiting the reaction to pass through. The remaining thermite in channel 1 does not appear to have further compaction from the extrusion process. Thus, the thermite located under the plunge was likely displaced towards the channel inlet during extrusion. Channels 2 and 3 have large deformation in the channel groove under the plunge location. The extrusion groove is much more easily deformed for the larger channels since the walls under the load bearing area become thinner with larger radii channels. The groove deformation in channels 2 and 3 results in lower tool z-force measurements, since the widening of the groove allows for greater displacement of material around the tool pin. Additionally, a smaller mass of aluminum surrounding the channel has less heat capacity to cool the extruded plate.

Though joint separation was not achieved, this work demonstrated a self-propagating thermite reaction where the reactants were integrated into an extruded joint. The FSE process is beneficial due to its versatility and capability to join both similar and dissimilar alloys [214]. Its low joining temperatures combined with thermite's high ignition temperatures makes this a safe process and eliminates the possibility for preignition. Future work will require optimization of joining material dimensions to reduce joint weight and heat loss that prevents material from melting. Following steps to mature FSE pyrotechnic joints will focus on the separation functions to make them an attractive choice in spacecraft applications. Joint strength and further analysis of the extrusion interaction will also be explored. Adding electronic ignitors, such as the nichrome wire used in Densmore et. al [221], will provide more consistent ignitions across test samples and allow for study of the pyrotechnic performance in more orientations.

### A.4 Conclusion

An encapsulated pyrotechnic joint was created using FSE to form a mechanical interlock between an aluminum plate and a thermite filled channel in an aluminum block. Tests showed that a sound joint is possible when extruding into a hollowed cavity partially filled with a packed substance. The size of the thermite filled channel affects the extrusion forces as well as the joint integrity. Additionally, the channel size affects the energy output of the pyrotechnic and its ability to ignite and self-sustain. Enabling the separation functions of this new technology requires further material geometry optimization. Following extensive study, pyrotechnic joints formed by FSE will be extremely versatile due to the ability to encompass dissimilar materials. The pyrotechnic materials in the joints are extremely stable, making the joining process safe and efficient.

# References

[1] R.S. Mishra and Z.Y. Ma. Friction stir welding and processing. *Materials Science and Engineering*, 50:1–78, 2005.

[2] SooJin Park. *Carbon Fibers*, volume 40. Springer, 2018.

[3] U.s. plastic pipe industry reports august 2022, 2022.

[4] Nicholas P. Cheremisinoff. *An Introduction to Polymer Rheology and Processing*. CRC Press, 1993.

[5] Gideon A. Lyngdoh and Sumanta Das. Elucidating the interfacial bonding behavior of over-molded hybrid fiber reinforced polymer composites: Experiment and multiscale numerical simulation. *ACS Applied Materials and Interfaces*, 14:43666–43680, 9 2022.

[6] J.M.G. Cowie. *Polymers: Chemistry and Physics of Modern Materials*. Chapman and Hall, 1991.

[7] Shayan Eslami, Paulo J. Tavares, and P. M.G.P. Moreira. Friction stir welding tooling for polymers: review and prospects. *The International Journal of Advanced Manufacturing Technology*, 89:1677–1690, 2017.

[8] H. W. Zhang, Z. Zhang, and J. T. Chen. The finite element simulation of the friction stir welding process. *Materials Science and Engineering: A*, 403:340 – 348, 2005.

[9] F. Simoes and D. M. Rodrigues. Material flow and thermo-mechanical conditions during friction stir welding of polymers: Literature review, experimental results and empirical analysis. *Materials and Design*, 59:344–351, 2014.

[10] William J. Arbegast. A flow-partitioned deformation zone model for defect formation during friction stir welding. *Scripta Materialia*, 58:372–376, 2008.

[11] Mustafa Kemal Bilici and Ahmet Irfan Yükler. Influence of tool geometry and process parameters on macrostructure and static strength in friction stir spot welded polyethylene sheets. *Materials and Design*, 33:145–152, 2012.

[12] Seth R Strand. *Effects of Friction Stir Welding on Polymer Microstructure*. Ph.d. dissertation, Brigham Young University, 2004.

[13] H. Ahmadi, N. B. Mostafa Arab, and F. Ashenai Ghasemi. Optimization of process parameters for friction stir lap welding of carbon fibre reinforced thermoplastic composites by taguchi method. *Journal of Mechanical Science and Technology*, 28:279–284, 1 2014.

[14] Yahya Bozkurt. The optimization of friction stir welding process parameters to achieve maximum tensile strength in polyethylene sheets. *Materials and Design*, 35:440–445, 2012.

[15] A. Paoletti, F. Lambiase, and A. Di Ilio. Analysis of forces and temperatures in friction spot stir welding of thermoplastic polymers. *International Journal of Advanced Manufacturing Technology*, 83:1395–1407, 2016.

[16] Mehdi Pirizadeh, Taher Azdast, Samrand Rash Ahmadi, Sajjad Mamaghani Shishavan, and Arvin Bagheri. Friction stir welding of thermoplastics using newly designed tool. *Materials and Design*, 54:342–347, 2014.

[17] Yongxian Huang, Xiangchen Meng, Yuming Xie, Long Wan, Zongliang Lv, Jian Cao, and Jicai Feng. Friction stir welding/processing of polymers and polymer matrix composites. *Composites Part A: Applied Science and Manufacturing*, 105:235–257, 2018.

[18] Vipin Sharma, Ujjwal Prakash, and B.V. Manoj Kumar. Surface composites by friction stir processing: A review. *Journal of Materials Processing Technology*, 224:117–134, 2015.

[19] Akshat Patil, Arun Patel, and Rajesh Purohit. An overview of polymeric materials for automotive applications. *Materials Today: Proceedings*, 4:3807–3815, 2017.

[20] *Handbook of PVC pipe design and construction*. Industrial Press, Inc., fifth edition. edition, 2013.

[21] Steven Folkman. Water main break rates in the usa and canada: A comprehensive study. *Utah State University Buried Structures Laboratory*, 2018.

[22] *PE Pipe Handbook*. Plastic Pipe Institute, 2 edition, 2008.

[23] Georg Menges Tim A. Osswald. *Materials Science of Polymers for Engineers*. Carl Hanser Verlag, 2 edition, 2003.

[24] G. Hohne. *Differential scanning calorimetry*. Springer, 2nd rev. and enl.... edition, 2003.

[25] N. Koutras, J. Amirdine, N. Boyard, I. Fernandez Villegas, and R. Benedictus. *Composites Part A: Applied Science and Manufacturing*, 10.

[26] Pan Wang, Qing Lin, Yaming Wang, Chuntai Liu, and Changyu Shen. *Polymers and Polymer Composites*, 10.

[27] Robert M. Jones. *Mechanics of composite materials*. Taylor and Francis, 2nd ed. edition, 1999.

[28] Ken Ashbee. *Fundamental Principles of Fiber Reinforced Composites*. Technomic Publishing Company, Inc., Lancaster, PA, 1989.

[29] James Edward Gordon. *The New Science of Strong Materials*. Penguin Books, London, 1968.

[30] Elham Khadem Shadpour Mallakpour. Recent development in the synthesis of polymer nanocompoites based in nano-alumina. *Progress in Polymer Science*, 51:74–93, 2015.

[31] Amor Mostafapour Hossein Laieghi, Sina Alipour. Heat-assisted friction stir welding of polymeric nanocomposite. *Science and Technology of Welding and Joining*, 25:56–65, 2020.

[32] S. Pavlidou and C.D. Papaspyrides. A review on polymer-layered silicate nanocomposites. *Progress in Polymer Science*, 33:1119–1216, 2008.

[33] Ali Gungor. Mechanical properties of iron powder filled high density polyethylene composites. *Materials and Design*, 28:1027–1030, 1 2007.

[34] Weld — definition in the cambridge english dictionary, 2023.

[35] What is welding? -definition, processes and types of welds, 2023.

[36] M. Vural. 6.02 - welding processes and technologies. pages 3–48. Elsevier, Oxford, 2014.

[37] P. G. de Gennes. Reptation of a polymer chain in the presence of fixed obstacles. 55:572–579, 1972.

[38] Masao Doi and Samuel F. Edwards. *The Theory of Polymer Dynamics*. Oxford Oxfordshire: Clarendon Press, 1986.

[39] Jeou Shyong Wang and Roger S. Porter. On the viscosity-temperature behavior of polymer melts. *Rheologica Acta*, 34:496–503, 1995.

[40] John M Dealy and K. F Wissbrun. *Melt Rheology and Its Role in Plastics Processing*. Springer Netherlands, 1990.

[41] Ginger Gardiner. Developing repairs for thermoplastic composite structures. *CompositesWorld*, 9+:26–32, 2023.

[42] Ginger Gardiner. Cfrtp upper stage propellant tank. *CompositesWorld*, 8:42–46, 2022.

[43] Ginger Gardiner. Thermoplastic composites welding advances for more sustainable airframes. *CompositesWorld*, 8:50–60, 2022.

[44] Wayne M.Thomas, Edward David Nicholas, James Cristopher Needham, Michael George Murch, Peter Temple Smith, and Christopfer John Dawes. Friction stir butt welding. *International Patent Application PCT/GB92, Patent Application GB9125978.8*, December 1991.

[45] N. Mendes, P. Neto, A. Loureiro, and A. P. Moreira. Machines and control systems for friction stir welding: A review. *Materials and Design*, 90:256–265, 2016.

[46] B.T. Gibson, D.H. Lammlein, T.J. Prater, W.R. Longhurst, C.D. Cox, M.C. Ballun, K.J. Dharmaraj, G.E. Cook, and A.M. Strauss. Friction stir welding: Process, automation, and control. *Journal of Manufacturing Processes*, 16:56–73, 2014.

[47] S. Lazarevic, S.F. Miller, J. Li, and B.E. Carlson. Experimental analysis of friction stir forming for dissimilar material joining application. *Journal of Manufacturing Processes*, 15:616–624, 2013.

[48] B. Christner and J. McCoury v S. Higgins. Development and testing of friction stir welding (fsw) as a joining method for primary aircraft structure. *4th International Symposium on Friction Stir Welding*, 2003.

[49] G. Wang Y. Zhao and Y. Hao. Friction stir welding of high-strength aerospace aliminum alloy and application in rocket tank manufacturing. *Journal of Materials Science and Engineering*, 34:73–91, 2018.

[50] Patrick J. G. Stiennon and David M. Hoerr. *The Rocket Company*. American Institute of Aeronautics and Astronautics, Reston, VA, 2005.

[51] Diogo Mariano Neto and Pedro Neto. Numerical modeling of friction stir welding process: a literature review. *International Journal of Advanced Manufacturung Technology*, 65:115–126, 2013.

[52] P.L. Threadgill. Terminology in friction stir welding. *Science and Technology of Welding and Joining*, 12:357–360, 2013.

[53] Seth Strand. Joining plastics - can friction stir welding compete? *Electrical Insulation Conference and Electrical Manufacturing and Coil Winding Conference and Exhibition*, pages 321–326, 2003.

[54] Wayne M. Thomas. Repair by friction welding. In *Exploiting Friction Welding Developments and Innovations*. The Welding Institute, Cambridge, 1984.

[55] Yanxiang Li Ailing Zhang. Effect of alloying elements on thermal conductivity of aluminum. *Journal of Materials Research*, 38:2049–2058, 2023.

[56] M. Day, D. Sally, and D.M. Wiles. Thermal degradation of poly(aryl-ether-ether-ketone): Experimental evaluation of crosslinking reactions. *Journal of applied polymer science*, 40,:1615–1625, 1990.

[57] Amir Mostafapour. A study on the role of processing parameters in joining polyethylene sheets via heat assisted friction stir welding: Investigating microstructure, tensile and flexural properties. *International Journal of the Physical Sciences*, 7, 2012.

[58] H. Su, C.S. Wu, M. Bachmann, and M. Rethmeier. Numerical modeling for the effect of pin profiles on thermal and material flow characteristics in friction stir welding. *Materials and Design*, 77:114–125, 2015.

[59] D. Das, S. Bag, and S. Pal. A finite element model for surface and volumetric effects in the fsw process using a coupled eulerian-langrangian approach. *Science and Technology of Welding and Joining*, 26:412–419, 2021.

[60] L. Fratini, G. Buffa, D. Palmeri, and R. Shivpuri. Material flor in fsw of aa7075-t6 butt joints: numerical simulations and experimental verifications. *Science and Technology of Welding and Joining*, 11:412–421, 2006.

[61] Z. Sun and C. S. Wu. Influence of tool thread pitch on material flow and thermal process in friction stir welding. *Journal of Materials Processing Technology*, 275, 2020.

[62] Yucan Zhu, Gaoqiang Chen, Qilong Chen, Gong Zhang, and Qingyu Shi. Simulation of material plastic flow driven by non-uniform friction force during friction stir welding and related defect prediction. *Materials and Design*, 108:400–410, 2016.

[63] S. Verma and Meenu Study on temperature distribution during Friction Stir Welding of 6082 aluminum alloy J.P. Misra. Study on temperature distribution during friction stir welding of 6082 aluminum alloy. *Materials Today: Proceedings*, 4:1350–1356, 2017.

[64] Z. Zhang and H. W. Zhang. Solid mechanics-based eulerian model of friction stir welding. *International Journal of Advanced Manufacturing Technology*, 72:1647–1653, 2014.

[65] Y. G. Kim, H. Fujii, T. Tsumura, T. Komazaki, and N. Nakata. Three defect types in friction stir welding of aluminum die casting alloy. *Materials Science and Engineering: A*, 415:250–254, 2006.

[66] Hamed Aghajani Derazkola and Abdolreza Simchi. Experimental and thermomechanical analysis of the effect of tool pin profile on the friction stir welding of poly(methyl methacrylate) sheets. *Journal of Manufacturing Processes*, 34:412–423, 2018.

[67] Razi Ur Rehman, Jamal Sheikh-Ahmad, and Suleyman Deveci. Effect of preheating on joint quality in the friction stir welding of bimodal high density polyethylene. *The International Journal of Advanced Manufacturing Technology*, 117, 2021.

[68] J. Y. Sheikh-Ahmad, Suleyman Deveci, Fahad Almaskari, and Razi UR Rehman. Effect of process temperatures on material flow and weld quality in the friction stir welding of high density polyethylene. *Journal of Materials Research and Technology*, 18:1692–1703, 5 2022.

[69] Akos Meilinger and Imre Torok. The importance of friction stir welding tool. *Production Processes and Systems*, 6:25–34, 2013.

[70] K. Panneerselvam and K. Lenin. Investigation on effect of tool forces and joint defects during fsw of polypropylene plate. *Procedia Engineering*, 38:3927–3940, 2012.

[71] K. Panneerselvam and K. Lenin. Joining of nylon 6 plate by friction stir welding process using threaded pin profile. *Materials and Design*, 53:302–307, 2014.

[72] Bandari Vijendra and Abhay Sharma. Induction heated tool assisted friction-stir welding (i-fsw): A novel hybrid process for joining of thermoplastics. *Journal of manufacturing processes*, 20:234–244, 2015.

[73] Arvin Bagheri, Taher Azdast, and Ali Doniavi. An experimental study on mechanical properties of friction stir welded abs sheets. *Materials and Design*, 43:402–409, 2013.

[74] Tracy W. Nelson, Carl D. Sorenson, and Clark J. Johns. Friction stir welding of polymeric materials.

[75] A. Mostafapour and F. Taghizad Asad. Investigations on joining of nylon 6 plates via novel method of heat assisted friction stir welding to find the optimum proces parameters. *Science and Technology of Welding and Joining*, 21:660–669, 2015.

[76] R. Rahbarpour, T. Azdast, H. Rahbarpour, and S. M. Shishavan. Feasibility study of friction stir welding of wood-plastic composites. *Science and Technology of Welding and Joining*, 19, 2014.

[77] Mojtaba Rezaee Hajideh, Mohammadreza Farahani, Seyed Amir Davoud Alavi, and Navid Molla Ramezani. Investigation on the effects of tool geometry on the microstructure and the mechanical properties of dissimilar friction stir welded polyethylene and polypropylene sheets. *Journal of Manufacturing Processes*, 26:269–279, 2017.

[78] Z. Kissv and T. Czigany. Effect of welding parameters on the heat affected zone and the mechanical properties of friction stir welded poly(ethylene-terephthalate-glycole). *Journal of Applied Polymer Science*, 125:2231–2238, 2012.

[79] Douglas C. Montgomery. *Design and analysis of experiments*. Wiley, 3rd ed. edition, 1991.

[80] Mohamed-Ali Rezgui, Ali-Chedli Trabelsi, Mahfoudh Ayadi, and Khaled Hamrouni. Optimization of friction stir welding process of high density polyethylene. *International Journal of Production and Quality Engineering*, 2:55–61, 2011.

[81] Imad M. Husain, Raed K. Salim, Taher Azdast, Soran Hasanifard, Sajjad M. Shishavan, and Richard Eungkee. Mechanical properties of friction-stir-welded polyimide sheets. *International Journal of Mechancial and Materials Engineering*, 10, 2015.

[82] Mohommad Arif, Dilip Kuma, and Arshad Noor Siddiquee. Friction stir welding and friction stir spot welding of polymethyl methacrylate (pmma) to other materials: A review. *MAterials Today: Proceedings*, 62:220–225, 2022.

[83] Adeel Zafar, M. Awang, and Sajjad Raza Khan. Friction stir welding of polymers: An overview. *Lecture Notes in Mechanical Engineering*, pages 19–36, 2017.

[84] Parviz Asadi, Mohammad Hosein Mirzaei, and Mostafa Akbari. Modeling of pin shape effects in bobbin tool fsw. *International Journal of Lightweight Materials and Manufacture*, 5:162–177, 2022.

[85] Jasni Jayran, Azman Ismail, Fatin Nur Zulkipli, Bakhtiar Ariff Baharudin, and Darulihsan Abdul Hamid. *Materials Innovations and Solutions in Science and Technology*, volume 173. Springer, 2023.

[86] Xin Jin, Lars Heepe, Jan Strueben, Rainer Adelung, Stanislav N. Gorb, and Anne Staubitz. Challenges and solutions for joining polymer materials. *Macromolecular Rapid Communications*, 35:1551–1570, 2014.

[87] Sudhir Kumar and Barnik Saha Roy. A comparative analysis on friction stir welding of similar and dissimilar polymers: acrylonitrile butadiene styrene and polycarbonate plates. *Welding in the World*, 66:1141–1153, 2022.

[88] Sanjeev Kumar, Sujeet Kumar Chaubey, Durjyodhan Sethi, Subhash Chandra Saha, and Barnik Saha Roy. Performance analysis of varying tool pin profile on friction stir welded 2050-t84al-cu-li alloy plates. *Journal of Materials Engineering and Performance*, 31:2074–2085, 2022.

[89] Carlos Federico Jasso-Gastinel and Jose Maria Kenny. *Modification of polymer properties*. Elsevier, 2017.

[90] M. K. Bilici. Effect of tool geometry on friction stir spot welding of polypropylene sheets. *Express Polymer Letters*, 6:805–813, 2012.

[91] Santosh K. Sahu, Debasish Mishra, Raju P. Mahto, Vyas M. Sharma, Surjya K. Pal, Kamal Pal, Susanta Banerjee, and Padmanav Dash. Friction stir welding of polypropylene sheet. *Engineering Science and Technology, an International Journal*, 21:245–254, 2018.

[92] V. Jaiganesh, B. Maruthu, and E. Gopinath. Optimization of process parameters on friction stir welding of high density polypropylene plate. *Procedia Engineering*, 97:1957–1965, 2014.

[93] Md Reza-E-rabby and Anthony P. Reynolds. Effect of tool pin thread forms on friction stir weldability of different aluminum alloys. *Procedia Engineering*, 90:637–642, 2014.

[94] Mustafa Boz and Adem Kurt. The influence of stirrer geometry on bonding and mechanical properties in friction stir welding process. *Materials and Design*, 25:343–347, 2004.

[95] Parviz Asadi Mohsen Barmouz, Peyman Shahi. *Friction stir welding/processing of polymeric materials*. 2014.

[96] Densetec hdpe sheet :. Technical report, 2018.

[97] William Russell Longhurst. *Force Control of Friction Stir Welding*. Ph.d. dissertation, Vanderbilt University, 2009.

[98] John R. Walker. *Machining fundamentals*. Goodheart-Willcox, 2004.

[99] S. M. Chowdhury, D. L. Chen, S. D. Bhole, and X. Cao. Effect of pin tool thread orientation on fatigue strength of friction stir welded az31b-h24 mg butt joints. *Procedia Engineering*, 2:825–833, 2010.

[100] W. Tang Yuh J. Chao, X. Qi. Heat transfer in friction stir welding—experimental and numerical studies. *Journal of manufacturing science and engineering*, 125:138–145, 2003.

[101] Durjyodhan Sethi, Uttam Acharya, Shashank Shekhar, and Barnik Saha Roy. Applicability of unique scarf joint configuration in friction stir welding of aa6061-t6: Analysis of torque, force, microstructure and mechanical properties. *Defence Technology*, 18:567–582, 4 2022.

[102] Erica Anna Squeo, Giuseppe Bruno, Alessandro Guglielmotti, and Fabrizio Quadrini. Friction stir welding of polyethylene sheets. *THE ANNALS OF "DUNĂREA DE JOS" UNIVERSITY OF GALAŢI FASCICLE V*, pages 241–146, 2009.

[103] N. Mendes, P. Neto, M. A. Simão, A. Loureiro, and J. N. Pires. A novel friction stir welding robotic platform: welding polymeric materials. *International Journal of Advanced Manufacturing Technology*, 85:37–46, 2016.

[104] Shayan Eslami, Luis Mourão, Nuno Viriato, Paulo J. Tavares, and P. M.G.P. Moreira. Multi-axis force measurements of polymer friction stir welding. *Journal of Materials Processing Technology*, 256:51–56, 2018.

[105] S I Abu-Eishah. Correlations for the thermal conductivity of metals as a function of temperature. *International journal of thermophysics*, 22:1855–1868, 2001.

[106] A. U. Chaudhry, Abdelnasser Mabrouk, and Ahmed Abdala. Thermally enhanced pristine polyolefins: Fundamentals, progress and prospective. *Journal of Materials Research and Technology*, 9:10796–10806, 2020.

[107] Mostafa Akbari, Parviz Asadi, and Reza Abdi Behnagh. Modeling of material flow in dissimilar friction stir lap welding of aluminum and brass using coupled eulerian and lagrangian method. *International Journal of Advanced Manufacturing Technology*, 113:721–734, 2021.

[108] 2017 infrastructure report card. *American Society of Civil Engineers*, 2017.

[109] E. Baumann. Ueber einige vinylverbindungen. *Justus Liebigs Annalen der Chemie*, 163:308–322, 1872.

[110] Jeroen Langeveld Konstantinos F. Makris and Francois H. L. R. Clemens. A review on the durability of pvc sewer pipes: Research vs. practice. *Structure and Infrastructure Engineering*, 16:880–897, 2020.

[111] Safety data sheet: Regular clear and regular clear advanced pvc cement, 2022.

[112] Bryan Hauger. Advanced nuclear technology: Material properties affecting the butt fusion of hdpe pipe. *Electric Power Research Institute*, 2014.

[113] Ramsey F. Hamade, Tarek R. Andari, Ali H. Ammouri, and I. S. Jawahir. Rotary friction welding versus fusion butt welding of plastic pipes – feasibility and energy perspective. *Procedia Manufacturing*, 33:693–700, 2019.

[114] Amir Mosavvar, Taher Azdast, Milad Moradian, and Rezgar Hasanzadeh. Tensile properties of friction stir welding of thermoplastic pipes based on a novel designed mechanism. *Welding in the World*, 63:691–699, 5 2019.

[115] Lucas T Wilkins and Alvin M Strauss. Influence of tool thread pitch during friction stir welding of high density polyethylene plate. *Journal of Manufacturing Science and Engineering*, 144, December 2022.

[116] S Inaniwa, Y Kurabe, Y Miyashita, and H Hori. Application of friction stir welding for several plastic materials. *Proceedings of the 1st International Joint Symposium on Joining and Welding*, 2013.

[117] E J Comeaux, C H Chen, J R Collier, and R D Wesson. Fusion study of polyvinyl chloride (pvc): Relation of processing time and processing temperature to the degree of fusion, 1994.

[118] Jie Yu, Lushi Sun, Chuan Ma, Yu Qiao, and Hong Yao. Thermal degradation of pvc: A review. *Waste Management*, 48:300–314, 2 2016.

[119] Patrick Pimenta R. Cruz, Leonardo Cerqueira da Silva, Raildo A. Fiuza-Jr, and Humberto Polli. Thermal dehydrochlorination of pure pvc polymer: Part i—thermal degradation kinetics by thermogravimetric analysis. *Journal of Applied Polymer Science*, 138, 7 2021.

[120] D. Trimble, J. Monaghan, and G. E. O'Donnell. Force generation during friction stir welding of aa2024-t3. *CIRP Annals - Manufacturing Technology*, 61:9–12, 2012.

[121] ASTM. Standard test method for resistance to short-time hydraulic pressure of plastic pipe, tubing, and fittings. *ASTM International*, 2018.

[122] Qian Shi, Chenyu Jin, Zhiqiang Chen, Le An, and Tiejun Wang. On the welding of vitrimers: Chemistry, mechanics and applications. *Advanced Functional Materials*, 2023.

[123] Hamed Aghajani Derazkola and Abdolreza Simchi. Processing and characterizations of polycarbonate/alumina nanocomposites by additive powder fed friction stir processing. *Thin-Walled Structures*, 157:107086, 2020.

[124] ASTM. Standard specification for poly(vinyl chloride (pvc) plastic pipe fittings, schedule 40. *ASTM International*, 2021.

[125] Keith Flamer and Updated by Daniel Bortz. Best cordless drills of 2023. *Consumer Reports*, May 2023.

[126] *PVC pipe– design and installation*. Anerican Water Works Association, 2nd ed. edition, 2002.

[127] Mohsen Barmouz, Javad Seyfi, Mohammad Kazem Besharati Givi, Iman Hejazi, and Seyed Mohammad Davachi. A novel approach for producing polymer nanocomposites by in-situ dispersion of clay particles via friction stir processing. *Materials Science and Engineering A*, 528:3003–3006, 2011.

[128] A. S. Luyt, J. A. Molefi, and H. Krump. Thermal, mechanical and electrical properties of copper powder filled low-density and linear low-density polyethylene composites. *Polymer Degradation and Stability*, 91:1629–1636, 7 2006.

[129] Andrea Labouriau, Tom Robison, Clinton Shonrock, Steve Simmonds, Brad Cox, Adam Pacheco, and Carl Cady. Boron filled siloxane polymers for radiation shielding. *Radiation Physics and Chemistry*, 144:288–294, 3 2018.

[130] Qingzhong Xue. The influence of particle shape and size on electric conductivity of metal–polymer composites. *European Polymer Journal*, 40:323–327, 2 2004.

[131] Xiangyu Li, Wonjun Park, Yong P. Chen, and Xiulin Ruan. Effect of particle size and aggregation on thermal conductivity of metal-polymer nanocomposite. *Journal of Heat Transfer*, 139, 2 2017.

[132] Shao Yun Fu, Xi Qiao Feng, Bernd Lauke, and Yiu Wing Mai. Effects of particle size, particle/matrix interface adhesion and particle loading on mechanical properties of particulate-polymer composites. *Composites Part B: Engineering*, 39:933–961, 9 2008.

[133] Seyed Mojtaba Zebarjad. Production of polyethylene/carbon nanotube nanocomposite using mechanical milling process and investigation of its microstructure, 12 2009.

[134] Amir Mostafapour Ehsan Azarsa. On the feasibility of producing polymer-metal composites via novel variant of friction stir processing. *Journal of Manufacturing Processes*, 15:682–688, 2013.

[135] Shahram Alyali, Amir Mostafapour, and Ehsan Azarsa. Fabrication of pp/al2o3 surface nanocomposite via novel friction stir processing approach, 2012.

[136] C. J. Lee, J. C. Huang, and P. J. Hsieh. Mg based nano-composites fabricated by friction stir processing. *Scripta Materialia*, 54:1415–1420, 4 2006.

[137] J. Liu, W.-J. Boo, A. Clearfield, and H.-J. Sue. Intercalation and exfoliation: A review on morphology of polymer nanocomposites reinforced by inorganic layer structures. *Materials and manufacturing processes*, 21:143–151, 2006.

[138] Armagan Arici and Tamer Sinmaz. Effects of double passes of the tool on friction stir welding of polyethylene. *Journal of Materials Science*, 40:3313–3316, 2005.

[139] Hung-Yin Tsai, Elisabetta Ceretti, Davide Rizzi, Paola Ginestra, Tuan-Huan Kao, and Ming C. Leu. Laser induced metallization on flexible polymer coating: Analysis and application. *Journal of materials processing technology*, 290:116986, 2021.

[140] Junjin Che, Kai Wu, Yunjie Lin, Ke Wang, and Qiang Fu. Largely improved thermal conductivity of hdpe/expanded graphite/carbon nanotubes ternary composites via filler network-network synergy. *Composites. Part A, Applied science and manufacturing*, 99:32–40, 2017.

[141] Y. Gao, Y. Morisada, H. Fujii, and J. Liao. Friction stir lap welding of plastic to metal using adjustable tool. *Science and technology of welding and joining*, 25:190–197, 2020.

[142] W. Ratanathavorn and A. Melander. Dissimilar joining between aluminium alloy (aa 6111) and thermoplastics using friction stir welding. *Science and Technology of Welding and Joining*, 20:222–228, 2015.

[143] Vincent A. Suprynowicz. *Electrical and Electronics Fundamentals: An Applied Survey of Electrical Engineering*. West Group, 1987.

[144] Ragnar Holm. *Electric contacts; theory and application*. Springer-Verlag, 4th completely re... edition, 1967.

[145] F. Khodabakhshi, M. Haghshenas, S. Sahraeinejad, J. Chen, B. Shalchi, J. Li, and A. P. Gerlich. Microstructure-property characterization of a friction-stir welded joint between aa5059 aluminum alloy and high density polyethylene. *Materials Characterization*, 98:73–82, 2014.

[146] D. E. Hastings. A review of plasma interactions with spacecraft in low earth orbit. *Journal of Geophysical Research*, 100:14457–14483, 1995.

[147] Hicham Ghossein, Ahmed Arabi Hassen, Seokpum Kim, Jesse Ault, and Uday K. Vaidya. Characterization of mechanical performance of composites fabricated using innovative carbon fiber wet laid process. *Journal of Composites Science*, 4, 2020.

[148] Jawaid Mohammad and Thariq Mohamed. *The Role of Advanced Polymer Materials in Aerospace*. Elsevier, 2018.

[149] A. U. Sudhin, Manu Remanan, G. Ajeesh, and Karingamanna Jayanarayanan. Comparison of properties of carbon fiber reinforced thermoplastic and thermosetting composites for aerospace applications. *Materials Today: Proceedings*, 24:453–462, 2020.

[150] G. Ajeesh, Shantanu Bhowmik, Venugopal Sivakumar, Lalit Varshney, Virendra Kumar, and Mathew Abraham. Investigation on polyetheretherketone composite for long term storage of nuclear waste. *Journal of nuclear materials*, 467:855–862, 2015.

[151] A comprehensive review of the processing guidelines of victrex ® peek ™ high performance polymer.

[152] Miguel A.R. Pereira, Ivan Galvão, Jose Domingos Costa, Ana M. Amaro, and Rui M. Leal. Joining of fibre-reinforced thermoplastic polymer composites by friction stir welding—a review. *Applied Sciences (Switzerland)*, 12, 3 2022.

[153] Fatemeh Kordestani, Faramarz Ashenai Ghasemi, and N. B. Mostafa Arab. An investigation of fsw process parameters effects on mechanical properties of pp composites. *Mechanics and Industry*, 17, 2016.

[154] G.H. Payganeh, N.B. Mostafa Arab, Y. Dadgar Asl, F.A. Ghasemi, and M. Saeidi Boroujeni. Effects of friction stir welding process parametrs on appearance and strength of polypropylene composte welds. *International Journal of Physical Sciences*, 6:4595–4601, 2011.

[155] N. Mendes, A. Loureiro, C. Martins, P. Neto, and J.N. Pires. Effect of friction stir welding parameters on morphology and strength of acrylontril butadine styrene plate welds. *Materials and Design*, 58:457 – 464, 2014.

[156] M. Mehta, A. Arora, A. De, and T. DebRoy. Tool geometry for friction stir welding-optimum shoulder diameter. *Metallurgical and Materials Transactions A*, 42:2716–2722, 2011.

[157] Luis Trueba, Georgina Heredia, Daniel Rybicki, and Lucie B. Johannes. Effect of tool shoulder features on defects and tensile properties of friction stir welded aluminum 6061-t6. *Journal of Materials Processing Technology*, 219:271–277, 2015.

[158] F. Kordestani, F. Ashenai Ghasemi, and N. B.M. Arab. Effect of pin geometry on the mechanical strength of friction-stir-welded polypropylene composite plates. *Mechanics of Composite Materials*, 53:525–532, 9 2017.

[159] M. K.Nor Khairusshima and I. S.S. Sharifah. Study on tool wear during milling cfrp under dry and chilled air machining. *Procedia Engineering*, 184:506–517, 2017.

[160] Blair E Carlson, David Ollett, and Sarah Kleinbaum. Final technical report-friction stir scribe joining of carbon fiber reinforced polymer (cfrp) to aluminum (general motors), 2016.

[161] T Czigany and Z Kiss. Friction stir welding of fiber reinforced polymer composites. 2011.

[162] S. P. Meyer, B. Jaeger, C. Wunderling, and M. F. Zaeh. Friction stir welding of glass fiber-reinforced polyamide 6: Analysis of the tensile strength and fiber length distribution of friction stir welded pa6-gf30. volume 480. Institute of Physics Publishing, 3 2019.

[163] Yongxian Huang, Xiangchen Meng, Yuming Xie, Junchen Li, and Long Wan. Joining of carbon fiber reinforced thermoplastic and metal via friction stir welding with co-controlling shape and performance. *Composites Part A: Applied Science and Manufacturing*, 112:328–336, 2018.

[164] Baoning Chang, Junfeng Gu, Zhiqiang Long, Zheng Li, Shilun Ruan, and Changyu Shen. Effects of temperature and fiber orientation on the tensile behavior of short carbon fiber reinforced peek composites. *Polymer Composites*, 42:597–607, 2021.

[165] T300 technical data sheet. *Toray Advanced Composites*, 2018.

[166] Toray cetex 1225 lmpaek product data sheet, 2020.

[167] Abdulbasit Abdulqadir Hamza and Shawnam Rashied Jalal. A review on manufacturing the polymer composites by friction stir processing. *European Polymer Journal*, 178, 9 2022.

[168] Haim Kalman. Effect of particle shape on void fraction. *Powder Technology*, 407, 7 2022.

[169] F. Rezaei, R. Yunus, and N. A. Ibrahim. Effect of fiber length on thermomechanical properties of short carbon fiber reinforced polypropylene composites. *Materials and Design*.

[170] J.S. Lin Youngchul Lee, Roger S. Porter. On the double-melting behavior of poly(ether ether ketone). *Macromolecules*, 22, 1989.

[171] Robin Hron, Martin Kadlec, and Roman Růžek. Effect of the test procedure and thermoplastic composite resin type on the curved beam strength. *Materials*, 14:1–13, 2021.

[172] David. Kemmish. *Update on the technology and applications of polyaryletherketones*. iSmithers, a Smithers Group Co., 2010.

[173] Bram Jongbloed, Julie Teuwen, Genevieve Palardy, Irene Fernandez Villegas, and Rinze Benedictus. Continuous ultrasonic welding of thermoplastic composites: Enhancing the weld uniformity by changing the energy director. *Journal of Composite Materials*, 54:2023–2035, 2020.

[174] Ginger Gardiner. Welding thermoplastic composites. *CompositesWorld*, 9 2018.

[175] Jeong Won Choi, Yoshiaki Morisada, Huihong Liu, Kohsaku Ushioda, Hidetoshi Fujii, Kimiaki Nagatsuka, and Kazuhiro Nakata. Dissimilar friction stir welding of pure ti and carbon fibre reinforced plastic. *Science and Technology of Welding and Joining*, pages 600–608, 2020.

[176] Yuki Ogawa, Yida Xiong, Hiroyuki Akebono, Masahiko Kato, Kojiro Tanaka, and Atsushi Sugeta. Fatigue properties of friction stir welds of treated al to carbon fibre-reinforced plastic. *Science and Technology of Welding and Joining*, 23:79–86, 2018.

[177] Hedi Ahmadi, Nasrollah Bani Mostafa Arab, and Faramarz Ashenai Ghasemi. Application of taguchi method to optimize friction stir welding parameters for polypropylene composite lap joints. *Archives des Sciences -Geneve-*, 65:59–74, 2012.

[178] Hans Luinge, D Dewayne Howell, and Jerik Straetker. Low melt paek (lm paek) prepreg for improved processing of thermoplastic composites. *SAMPE Conference Proceedings*, 2019.

[179] Lucas T. Wilkins and Alvin M. Strauss. Friction stir welding of lapped low-melt polyaryletherketone carbon fiber reinforced thermoplastic laminate. *Journal of Composite Materials*, 57, August 2023.

[180] Ali Yousefpour, Mehdi Hojjati, and Jean Pierre Immarigeon. Fusion bonding/welding of thermoplastic composites. *Journal of Thermoplastic Composite Materials*, 17:303–341, 7 2004.

[181] John Edward Brennan. *The Crystallization of Polyetheretherketone (PEEK) From the Glass*. Ph.d. thesis, University of Illinois at Urbaba-Champaign, 1988.

[182] Vidya Kishore, Xun Chen, Ahmed A Hassen, John Lindahl, Vlastimil Kunc, and Chad Duty. Effect of post-processing annealing on crystallinity development and mechanical properties of polyphenylene sulfide composites printed on large-format extrusion deposition system. Technical report, Oak Ridge National Laboratory, 2019.

[183] Michael Handwerker, Jörg Wellnitz, Hormoz Marzbani, and Ulrich Tetzlaff. Annealing of chopped and continuous fibre reinforced polyamide 6 produced by fused filament fabrication. *Composites Part B: Engineering*, 223, 10 2021.

[184] Xiao Yu, Wenzhe Song, Jinghua Zheng, Yiwei Chen, Linlin Luo, Congze Fan, and Zhongde Shan. Effects of low-pressure annealing on the performance of 3d printed cf/peek composites. *Chinese Journal of Mechanical Engineering: Additive Manufacturing Frontiers*, 2:100076, 6 2023.

[185] Hui Jin Um, Yeon Taek Hwang, Kyung Hee Choi, and Hak Sung Kim. Effect of crystallinity on the mechanical behavior of carbon fiber reinforced polyethylene-terephthalate (cf/pet) composites considering temperature conditions. *Composites Science and Technology*, 207, 5 2021.

[186] Jérémie Audoit, Lisa Rivière, Jany Dandurand, Antoine Lonjon, Eric Dantras, and Colette Lacabanne. Thermal, mechanical and dielectric behaviour of poly(aryl ether ketone) with low melting temperature. *Journal of Thermal Analysis and Calorimetry*, 2.

[187] Ines Schiel, Lukas Raps, Ashley R. Chadwick, Isabelle Schmidt, Manuel Simone, and Sebastian Nowotny. *Advanced Manufacturing: Polymer and Composites Science*.

[188] R H Olley, D C Bassett, J J Thomson, and D J Blundell. Permanganic etching of peek. *Polymer*, 27, 1986.

[189] Aditya Ramgobin, Gaëlle Fontaine, and Serge Bourbigot. A case study of polyether ether ketone (i): Investigating the thermal and fire behavior of a high-performance material. *Polymers*, 8.

[190] Giovanni Esteves, Klarissa Ramos, Chris M. Fancher, and Jacob L. Jones. *LIPRAS: Line-Profile Analysis Software*, 03 2017.

[191] Ruth Pritchard. The transparency of crystalline polymers. *Polymer Engineering and Science*, 4:66–71, 1964.

[192] Shang Lin Gao and Jang Kyo Kim. Correlation among crystalline morphology of peek, interface bond strength, and in-plane mechanical properties of carbon/peek composites. *Journal of Applied Polymer Science*, 84:1155–1167, 2 2002.

[193] Hui Jin Um, Yeon Taek Hwang, Kyung Hee Choi, and Hak Sung Kim. Effect of crystallinity on the mechanical behavior of carbon fiber reinforced polyethylene-terephthalate (cf/pet) composites considering temperature conditions. *Composites Science and Technology*, 5.

[194] Dong Yang, Yi Cao, Zhikun Zhang, Yifa Tin, and Dichen Li. Effects of crystallinity control on mechanical properties of 3d-printed short-carbon-fiber-reinforced polyether ether ketone composites. *Polymer Testing*, 97, 2021.

[195] Helena Perez-Martin, Paul Mackenzie, Alex Baidak, Conchur M. O Bradaigh, and Dipa Ray. Crystallisation behaviour and morphological studies of pekk and carbon fibre/pekk composites. *Composites Part A: Applied Science and Manufacturing*, 159, 8 2022.

[196] J. J. Sha, J. X. Dai, J. Li, Z. Q. Wei, J. M. Hausherr, and W. Krenkel. Influence of thermal treatment on thermo-mechanical stability and surface composition of carbon fiber. *Applied Surface Science*, 274:89–94, 6 2013.

[197] Huiqing Zhang. *Fire-safe polymers and polymer composites*. Ph.d. dissertation, University of Massachusetts Amherst, 2003.

[198] L. H Perng, C. J Tsai, and Y. C. Ling. Mechanism and kinetic modelling of peek pyrolysis by tg/ms. *Polymer (Guilford)*, 40:7321–7329, 1999.

[199] D.J. Blundell and B.N. Osborn. The morphology of poly(aryl-ether-ether-ketone). *Polymer*, 24:953–958, 1983.

[200] M. Dasriaux, S. Castagnet, L. Thilly, L. Chocinski-Arnault, and S.A.E. Boyer. Evolution of the amorphous fraction of peek during annealing at atmospheric and high pressure above the glas transition temperature. *Journal of Applied Polymer Science*, 130:1148–1157, 2013.

[201] M. Doumeng, L. Makhlouf, F. Berthet, O. Marsan, K. Delbé, J. Denape, and F. Chabert. A comparative study of the crystallinity of polyetheretherketone by using density, dsc, xrd, and raman spectroscopy techniques. *Polymer Testing*, 93, 2021.

[202] Dimitrios Gaitanelis, Chris Worrall, and Mihalis Kazilas. Detecting, characterising and assessing peek's and cf-peek's thermal degradation in rapid high-temperature processing. *Polymer Degradation and Stability*, 10.

[203] T Stern, G Marom, and E Wachtel. Origin, morphology and crystallography of transcrystallinity in polyethylene-based single-polymer composites. *Composites Part A*, 28:431–444, 1997.

[204] Peng Wang, Bin Zou, Shouling Ding, Chuanzhen Huang, Zhenyu Shi, Yongsheng Ma, and Peng Yao. Preparation of short cf/gf reinforced peek composite filaments and their comprehensive properties evaluation for fdm-3d printing. *Composites. Part B, Engineering*, 198:108175, 2020.

[205] Geoff. Eckold. *Design and manufacture of composite structures*. McGraw-Hill, 1994.

[206] Laurence J. Bement and Morry L. Schimmel. A manual for pyrotechnic design , development and qualification (nasa-tm-110172. *NASA Technical Memorandum*, 1995.

[207] James M. Womack. Computing risk of pyrotechnic devices using lot. *Military Operations Research*, 26:73–92, 2021.

[208] pyrotechnic device. *A Dictionary of Space Exploration*, 2018.

[209] Richard J Ott. Understanding pyrotechnic shock dynamics and response understanding pyrotechnic shock dynamics and response attenuation over distance attenuation, 2016.

[210] Kelsay E Neely, Kevin C Galloway, and Alvin M Strauss. Additively manufactured reactive material architectures as a programmable heat source. *3D printing and additive manufacturing*, 6:210–216, 2019.

[211] Michael D. Grapes, Robert V. Reeves, Kamel Fezzaa, Tao Sun, John M. Densmore, and Kyle T. Sullivan. In situ observations of reacting al/fe2o3 thermite: Relating dynamic particle size to macroscopic burn time. *Combustion and Flame*, 201:252–263, 2019.

[212] Kelsay Neely. *Additively Manufactured Thermite-Based Energetics: Characterization and Applications*. Ph.d. dissertation, Vanderbilt University, 2020.

[213] Yu Frolov, Pivkina Alla, D. Ivanov, D. Meerov, K. Monogarov N. Murav'ev, D. Dilhan, and S. Mudretzova. Selection and testing of thermite compositions for pyrotechnic devices. pages 301–311, 2007.

[214] William T Evans, Brian T Gibson, Jay T Reynolds, Alvin M Strauss, and George E Cook. Friction stir extrusion: A new process for joining dissimilar materials. *Manufacturing letters*, 5:25–28, 2015.

[215] Connor Strawn and Alvin M Strauss. Friction stir extrusion of aluminum aa6061 into isostatically molded graphite. *Journal of manufacturing processes*, 69:391–397, 2021.

[216] Adam W Jarrell, Jeff Cui, Alvin M Strauss, and George E Cook. Friction stir extrusion of thin sheet stock. *Manufacturing letters*, 24:38–42, 2020.

[217] Peng Zhang, Shengdun Zhao, Chuanwei Zhang, Zheng Chen, Jiaying Zhang, Liangyu Fei, and Peng Dong. Microstructure and mechanical properties of probeless friction stir extrusion joined joints of 6061-t6 aluminum alloy to q235 steel. *International journal of advanced manufacturing technology*, 2022.

[218] Tinu P Saju, R. Ganesh Narayanan, and Barnik Saha Roy. Effect of pinless tool shoulder diameter on dieless friction stir extrusion joining of aa 5052-h32 and aa 6061-t6 aluminum alloy sheets. *Journal of mechanical science and technology*, 33:3981–3997, 2019.

[219] M Paidar, V Mohanavel, O.O Ojo, S Mehrez, S Rajkumar, and M Ravichandran. Dieless friction stir extrusion-brazing (dfse-b) of aa2024-t3 aluminum alloy to copper with zn interlayer. *Results in physics*, 24:104101, 2021.

[220] Kyle T. Sullivan, Cheng Zhu, Eric B. Duoss, Alexander E. Gash, David B. Kolesky, Joshua D. Kuntz, Jennifer A. Lewis, and Christopher M. Spadaccini. Controlling material reactivity using architecture. *Advanced materials*, 28:1934–1939, 2016.

[221] J.M. Densmore, K.T. Sullivan, and A. E. Gash. Thermal imaging of thermite flame propagation, llnl-jrnl-648519. *Lawrence Livermore National Laboratory*, 2014.